ABSTRACT

CHEMISTRY

BROWN, SADE

B.S. WINSTON-SALEM STATE UNIVERSITY, 2011

M.S. NORTH CAROLINA CENTRAL UNIVERSITY, 2013

PREPARATION AND CHARACTERIZATION OF NANOCOMPOSITES, INCORPORATING CELLULOSE NANOMATERIALS IN POLYMER SYSTEMS

Committee Chair: Eric A. Mintz, Ph.D.

Dissertation dated May 2020

Cellulose nanocrystals (CNC) and cellulose nanofibers (CNF) are of great interest as reinforcing agents for polymer matrix composites due to their nanoscale and specific intrinsic properties of high strength and stiffness, combined with low weight, biodegradability and the environmental benefits arising from its use. For many applications, it is highly desirable to improve the toughness and stiffness of these cellulose nanocomposites. In this study, two critical issues were addressed: good interfacial interactions at filler and matrix interface and improved dispersion of nanocellulose in polyolefins to achieve desired properties by various approaches. Addressing these critical issues is particularly crucial for the fabrication of nanocellulose composites due to the non-polar characteristics of thermoplastic polymers, which limits interaction between the nanocellulose and hydrophobic polymer systems.

Nanocellulose/polyolefin composites were prepared by means of powder sintering, high-torque melt-mixing and *in situ* free radical polymerization.

It was found that lignin-coated cellulose nanocrystals (L-CNC) and lignin-coated nanofibers (L-CNFs) can act as nucleating agents, promoting the crystallization rates of these polyolefins, and, the addition of nanocellulose enhances all other physical properties. However, there were no significant improvements in the thermal properties of the nanocellulose/polyolefin composites. The Young's modulus, tensile strength, and storage modulus of the L-CNC/polyolefin nanocomposites were increased at a defined loading of L-CNCs due to the reinforcement effect of L- CNCs inside the polymer matrix.

The incorporation of L-CNCs in maleic anhydride functionalized polymer systems resulted in improvement in the thermal and mechanical properties. The obtained mechanical results showed improvement in Young's modulus, ultimate tensile strength, and tensile strength at a defined L-CNC loading for all nanocellulose/polyolefin composites. These improvements are due to better dispersion and compatibility of the L-CNCs in the hydrophobic polymer matrices, ultra-high molecular weight (UHMWPE), high-density polyethylene (HDPE) and polypropylene. We have found that the dispersion and distribution of CNCs in these polymer systems improved in the presence of lignin.

PREPARATION AND CHARACTERIZATION OF NANOCOMPOSITES, INCORPORATING CELLULOSE NANOMATERIALS IN POLYMER SYSTEMS

A DISSERTATION

SUBMITTED TO THE FACULTY OF CLARK ATLANTA UNIVERSITY

IN PARTIAL FULFILLMENT OF THE REQUIREMENTS FOR

THE DEGREE OF DOCTOR OF PHILOSOPHY

BY

SADE BROWN

DEPARTMENT OF CHEMISTRY

ATLANTA, GEORGIA

MAY 2020

ACKNOWLEDGEMENTS

I would first like to thank God and my savior Jesus Christ for the guidance and discipline he has given me through this process. I would also like to thank Clark Atlanta University (CAU) for the opportunity to pursue this Doctor of Philosophy in Chemistry. A distinctive and heartfelt thank you is extended to my mentor, advisor, and friend Dr. Eric Mintz for answering my many questions and guiding me through this process, as well as for allowing me to work within his research group. I thank my committee members Dr. David Veazie, Dr. Conrad Ingram, Dr. Cass Parker and Dr. Dinadayalane Tandabany for their guidance and advice. I am also grateful to my colleagues Ms. V. Sorsor, Dr. W. Simmons, Mr. K. Blue, and Ms. J. Jackson for their support and assistance.

I would like to thank the Department of Defense (DOD), Title III Historically Black Graduate Institutions (HBGI), Mr. Don Hylton, Dr. Kim Nelson of American Process Inc. (API), and Dr. Gregory Schueneman of USDA Forest Products Laboratory (FPL) for their contributions to this research.

I thank my family and friends who were a constant provider in advice and a source of calm through my many stressful moments. Last, but by no means least, I would like to thank my husband, Justin Brown, for his unwavering love, support, advice, and practical rationality and peace, which he brings to every aspect of my life. I am truly thankful to all.

TABLE OF CONTENTS

CHAPTER

CHAPTER

CHAPTER

LIST OF FIGURES

Figure

Figure

Figure

Figure

Figure

Figure

Figure

Figure

Figure

LIST OF TABLES

Table

Table

Table

LIST OF ABBREVIATIONS

AA	Acrylic acid
E_a	Activation energy
API	American Process Inc.
AVAP	American Value Added Pulping
ASTM	American Standard Testing Methods
ω	Angular frequency
n	Avrami exponent
k	Avrami rate constant
BC	Bacterial nanocellulose
BPO	Benzoyl peroxide
CNT	Carbon nanotubes
CNCs	Cellulose nanocrystals
CNFs	Cellulose nanofibers
*η	Complex viscosity
β	Cooling rate
k	Crystal growth
T_c	Crystallization temperature
t_c	Crystallization time

AGU	D-anhydroglucopyranose units
T_d	Decompostion Temperature
X_c	Degree of crystallinity
DP	Degree of polymerization
DCP	Dicumyl peroxide
DSC	Differential scanning calorimetry
DTBPO	Di-tert-butyl peroxide
DMA	Dynamic mechanical analysis
η'	Dynamic viscosity
E_α	Effective activation energy
E'	Elastic modulus
E''	Elastic loss modulus
α	Extent of conversion
T_α	Extent of conversion temperature
DTG	First derivative of the thermogravimetric analysis curve
F	Force
E_a	Activation Energy
FPL	Forest Park Laboratories
fHDPE	Functionalized HDPE
fPP	Functionalized PP
G'	Storage modulus
G"	Loss modulus
$t_{1/2}$	Half-time of crystallization

ΔH_m	Heat of fusion
Hz	Hertz
R	Gas constant
GPa	Gigapascals
GO	Graphene oxide
T_g	Glass transition temperature
Hz	Hertz
HDPE	High-density polyethylene
HPP	Homopolymer polypropylene
η''	Imaginary viscosity
IR	Infrared
T_0	Initial temperature
LPO	Lauroyl peroxide
L-CNCs	Lignin-coated cellulose nanocrystals
L-CNFs	Lignin-coated cellulose nanofibers
LLDPE	Linear low-density polyethylene
LDPE	Low-density polyethylene
Tan δ	Loss tangent value
MAPP	Maleated polypropylene
MA	Maleic anhydride
T_{max}	Maximum decomposition temperature
T_m	Melting temperature

MCC	Microcrystalline cellulose
NC	Nanocellulose
MMT	Organoclay
T_p	Peak maxima temperature
PETA	Pentaerythritol triacrylate
PAN	Poly(acrylonitrile)
PE	Polyethylene
PEO	Poly(ethylene oxide)
PET	Polyethylene terephthalate
PLA	Poly(lactic acid)
PMCs	Polymer Matrix Composites
PP	Polypropylene
PVA	Polyvinyl alcohol
PVC	Polyvinyl chloride
RCP	Random copolymers
X_t	Relative degree of crystallinity
SEM	Scanning electron microscopy
ε	Strain
ε_f	Strain at specimen failure
σ	Stress
Tan δ	Loss tangent value
TEMPO	2,2,6,6-tetramethylpiperidine-1-yl)oxidanyl

U_T	Tensile toughness
TBPB	Tert-butyl peroxy benzoate
TEGO	Thermally expanded graphite oxide
TGA	Thermogravimetric analysis
UHMWPE	Ultra-high molecular weight polyethylene
wt.%	Weight percentage

CHAPTER 1

LITERATURE REVIEW

1.1 Cellulose

Currently, there is a significant movement to utilize materials and experimental practices which cause minimal damage to the environment and enhance thermo-mechanical properties of polymers.[1-3] Some materials that meet these requirements are renewable, non-toxic, and biodegradable, such as cellulose. Cellulose is one of the most abundant polymeric materials on earth and is the primary constituent in the cell walls of plants. Cotton has the highest known cellulose content of any plant, with about 90% cellulose content.[4-5] Wood contains about 40–50% cellulose and bast fibers, e.g., hemp have 70–80% cellulose.[6] Figure 1 is a schematic representation of the hierarchical structure of cellulose in a tree which, spans nanoscale to macroscopic dimensions. It is a depiction of cellulose being the "building block" within tree structures.[7] Cellulose can also be found in various marine organisms, such as tunicates and algae.[8-9] Cellulose is a linear homo-polysaccharide consisting of D-anhydroglucopyranose units (AGU) connected by β-1,4-glycosidic bonds (see Figure 2).[9-10] Cellulose polymers can form ordered crystalline structures that are held together with hydrogen bonds due to the many hydroxyl groups in the molecule. The hydroxyl groupsin cellulose can form intra- and intermolecular hydrogen bonds, which contribute to the stiffness of the polymer chains

and the formation of sheet structures.[9] The sheets are held together by hydrogen bonding and van der Waals forces.[11] Hydrogen bonding amongst neighboring groups help maintain the structure and stability of cellulose, and is responsible for the materials high tensile strength.[12] Recently, nanocellulose has been recognized as an excellent filler to prepare polymer matrix composites (PMCs).[12-13]

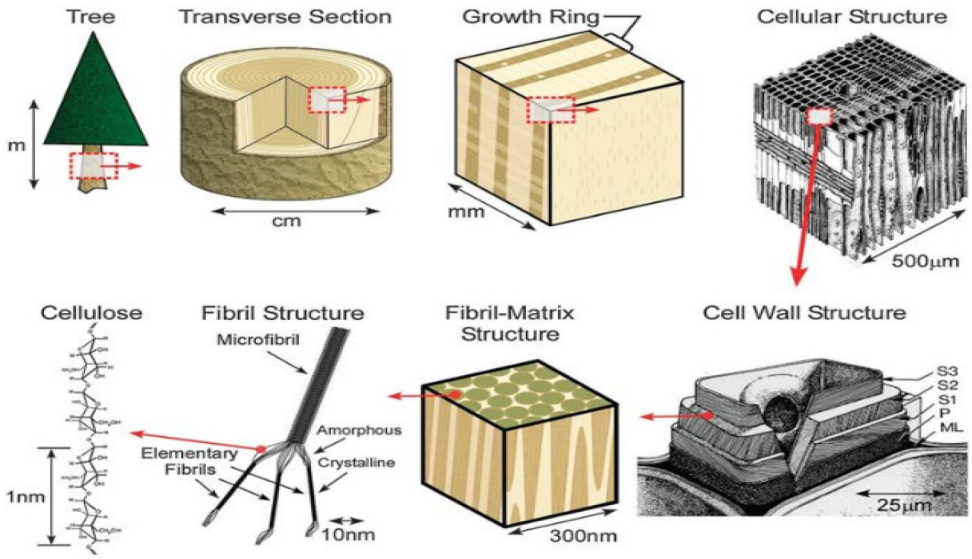

Figure 1. Schematic of the hierarchical structure of cellulose in trees.[7]

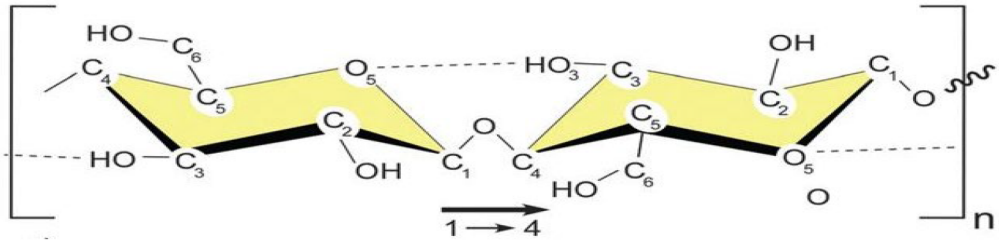

Figure 2. Schematics of a single cellulose chain repeat unit, showing the directionality of the 1 - 4 linkage and intrachain hydrogen bonding (dotted line).[10]

1.2 Nanocellulose (NC)

Nanocellulose materials include cellulose nanocrystals, and nanofibers. These materials are a less expensive substitute for carbon fiber and glass fiber for some PMC applications.[14] Nanometer-sized cellulose, such as cellulose nanocrystals (CNCs) and cellulose nanofibrils (CNFs) are produced by mechanical treatments or chemical modifications on cellulose pulp. CNCs have been isolated by hydrolyzing the non-crystalline regions of cellulose, and the remaining crystals are in the nanometer size range in at least one dimension. For CNFs, some of the inter-fibrillated hydrogen bonds will break and form materials that are micrometer in length and nanometer in width with non-crystalline regions present.[8, 15]

Cellulose nanocrystals (CNCs) can be modified with different functional groups to give different surface characteristics. The surface modification of nanocellulose depends on the isolation process and further desired treatment of the nanocrystals.[16-17] CNCs have been isolated by acid hydrolysis or (2,2,6,6-tetramethylpiperidine-1-yl)oxidanyl (TEMPO) oxidation of cellulose fibers.[18] These methods hydrolyze or oxidize the non-crystalline regions of the cellulose from many different sources such as hardwood pulp, softwood pulp, microcrystalline cellulose (MCC), cotton, bacterial cellulose, algae, and tunicin, see Figure 3 and 4.[17] The different cellulose sources give different structures and aspect ratios of the monocrystalline domains in them.[17]

These cellulose nanomaterials are excellent reinforcing agents due to their high strength, biodegradability, high aspect ratio, and low density. The physical and chemical properties of these nanofillers depend on their chemical structures.[19] Hydrogen bonding

is responsible for the crystalline structure of cellulose fibers resulting in its high tensile strength and modulus, and the tendency to form bundles.[20]

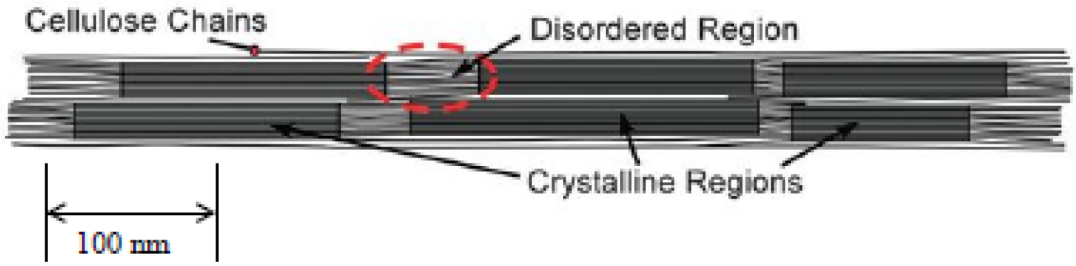

Figure 3. Representative configuration of the crystalline and amorphous regions of a cellulose microfibril.[17]

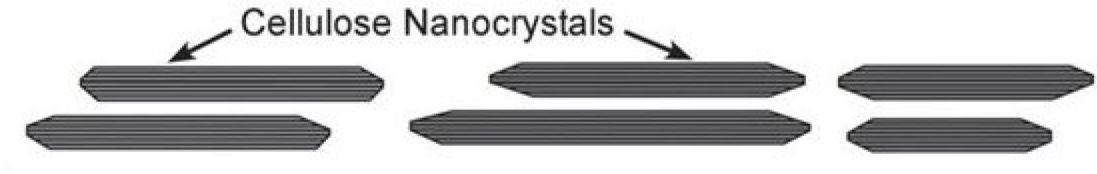

Figure 4. Cellulose nanocrystals after acid hydrolysis and removal of the disordered regions.[17]

CNCs have been isolated by the acidic hydrolysis of cellulose fibers derived from numerous sources.[6, 9] The isolation of CNCs is generally dependent on the type of acid, concentration, reaction temperature, and time.[21] Under acid hydrolysis, there is transverse cleavage of the microfibrils to produce short monocrystals.[21-22] In the primary stage of the hydrolysis, the glycosidic bonds are hydrolyzed after the acid diffuses into the non-crystalline segments. During hydrolysis, other glycosidic bonds become more accessible in the polymer to be hydrolyzed, and finally, hydrolysis occurs at the reducing

end group and at the surface of the nanocrystals. The reducing end group is considered "a disaccharide that contains a monosaccharide with a free anomeric carbon." The free anomeric carbon is a stereocenter that could have an aldehyde or ketone functional group of the open-ring form of the carbohydrate molecule that can reduce another compound.[16, 23] For example, by using a 64 wt.% sulfuric acid solution, hydrogen bonds will break, and the acid will penetrate into the non-crystalline and crystalline domains of the polymer, and approximately 0.5 to 2.0% of CNC-OH groups on the surface of the nanocrystal will react with sulfuric acid-producing charged sulfate ester groups on the nanocrystal surface.[16, 21] Furthermore, the anionic functionalized CNCs will form stable colloidal dispersion when diluted in water to specific concentrations, due to charged sulfate groups.[21, 24-25]

Interest in CNFs is due to its high aspect ratio and long, flexible microfibrils, which make them suitable for use as reinforcements in polymer matrices. CNFs are produced from many different types of cellulose sources. Researchers have studied CNFs from plant cells due to their high abundance and low cost.[26] It has been reported that incorporation of CNFs, produced from rutabaga, Kraft pulp, flax, and hemp fibers, in a polyvinyl alcohol (PVA) matrix led to improved mechanical properties in PMCs as compared with the neat PVA.[27] CNFs have also been produced by mechanical treatments of microfibrils, which break the fibers and the inter-fibrillar bonds between the cellulose molecules, resulting in "nanofibrils" with a diameter in nano-sized dimension and fiber length ranging from nanometer to micrometer.[28] Refining pulp, followed by homogenization, modifies the nanofibrils and gives a continuous dispersion when diluted

in water, which is considered a conventional mechanical treatment for CNFs.[9] Another practice used to produce CNFs was through regeneration and electrospinning of a cellulose polymer melt.[28]

CNCs exhibit excellent mechanical properties as compared to other fillers such as Kevlar, carbon fibers, or steel wire, as shown in Table 1.[9] Nanocellulose plays an essential role in several materials that are widely used in commercial, medical, food, and pharmaceutical industries.[9] It can also improve the combat survivability of the warfighter, which is considered the most critical aspect of military technology.[3, 9]

Table 1. Mechanical Properties (Tensile Strength and Young's Modulus) for Different Reinforcement Materials used in Commercial PMCs.[9]

Material	Tensile strength (GPa)	Young's modulus (GPa)
CNC	7.5-7.7	110-220
Kevlar	3.5	124-130
Steel wire	4.1	210
Carbon fiber	1.5-5.5	150-500
Carbon nanotubes	11-63	270-950

The preparation of nanocellulose polymer composites is of interest due to their distinctive properties, including renewability, biocompatibility, biodegradability, and the ease of surface modification, which is due to the abundance of surface –OH groups.[21] However, there remain disadvantages concerning the use of nanocellulose in PMCs, such as poor compatibility when incorporated in hydrophobic polymer matrices and high-moisture adsorption.[21] Recently, Menezes et al. incorporated CNCs modified with

nonpolar surface groups in low-density polyethylene (LDPE), which resulted in improved compatibility between the CNCs and LDPE, but did not lead to significant mechanical reinforcement.[29] Pereda et al. used poly(ethylene oxide) (PEO) as a compatibilizer to improve the dispersion of CNCs in the LDPE matrix; however, the mechanical properties of the nanocomposite films only showed a slight increase in the tensile modulus and strength.[30] Volk et al. used poly(ethylene glycol-*b*-ethylene) as a compatibilizer to melt-mix linear low-density polyethylene (LLDPE) and microfibrillated cellulose. The corresponding nanocomposites mechanical properties exhibited minor improvement compared to neat LLDPE.[31] Therefore, studies have been carried out to utilize both covalent or non-covalent interactions between nanocellulose and hydrophobic polymers to achieve desired functionalities.[9, 32-34]

Surface modified nanocellulose has been used to improve the interfacial compatibility with hydrophobic polymer matrices, such as polypropylene (PP), high-density polyethylene (HDPE) and ultra-high molecular weight polyethylene (UHMWPE) via covalent interactions.[35-36] Nanocellulose has been modified by coating the cellulose nanoparticles with surfactants or by chemically modifying the cellulose surface with hydrophobic groups.[37-38] The use of surfactants is the easier of these two methods. However, a considerable amount of surfactants is often necessary to coat the surface of the fillers, which causes defects in the corresponding composites.[37]

American Process Inc. (API) of Atlanta, Georgia, produces CNCs and CNFs via American Value Added Pulping (AVAP) process. API produces sugars by the hydrolysis of cellulose and has recently altered the AVAP process to produce CNCs and CNFs

under milder conditions than the sulfuric acid and (2,2,6,6-tetramethylpiperidine-1-yl)oxidanyl (TEMPO) processes. In the AVAP process, biomass is chemically pretreated using sulfur dioxide and ethanol to remove lignin, hemicelluloses, and amorphous regions of the cellulose. The sulfur dioxide frees the cellulose and hemicelluloses from the lignin while ethanol serves as the process solvent.[39] More importantly, they have also developed a process to deposit lignin onto the surface of CNCs and CNFs in situ, thus producing nanocellulosic materials with a hydrophobic surface, lignin-coated cellulose nanocrystals (L-CNCs) and lignin-coated cellulose nanofibers (L-CNFs). Lignin-coated cellulose nanocrystals (L-CNCs) produced from eucalyptus chips have an average length and diameter of ~350 nm and ~5-7 nm. Lignin has hydrophobic regions and is non-covalently attached to cellulose, which prevents re-aggregation of CNCs during processing and also improves interaction with the hydrophobic polymer matrix.[39-40] It has been found that API nanocellulose materials are more thermally stable than the corresponding CNCs and CNFs produced by acid hydrolysis and the TEMPO process.[41] A recent study indicated that L-CNCs are excellent nucleating agents for poly(lactic acid) (PLA), and upon incorporation by high-torque melt-mixing led to improved physical properties of PLA nanocomposites.[42] The coating of lignin on the surface of CNCs is an effective approach to improve the dispersion of CNCs in hydrophobic polymer systems, which in the case of PLA led to an increase in the degree of crystallinity and entanglement points of polymer chains.[42-43] Recently, it has been found that the incorporation of lignin in CNCs/polymer composites can improve dispersion and compatibility.[44-45]

Developing new nanocomposites with improved properties for lightweight armor systems is a crucial requirement for the department of defense.[1, 3] Polyolefins, nylons, polyesters, and aramid resins are of interest, considering their ability to be molded into fibers for high-performance thermoplastic nanocomposite materials. Recently, Cavallaro reported that textile materials, such as nylon, fiberglass, and Kevlar have provided body armor with extraordinarily improved ballistic protection levels at a significantly reduced weight.[46] Future improvements will be increasingly challenging to achieve because the expenses associated with developing new materials are becoming less cost-effective. However, recent advances in the incorporation of lignocellulosic nanomaterials into polymeric systems to produce nanocomposites with conventional resins that can be processed into fibers and films, provide a path forward to prepare new cost-effective PMC materials for incorporation in soft body armor.[42-43, 47]

1.3 Thermoplastics

The most often studied thermoplastics are polyolefins such as polypropylene and polyethylene, specifically high-density polyethylene and ultra-high molecular weight polyethylene.[48] Upon heating, thermoplastics are able to be shaped in the molten phase of the resin and, therefore, can be extruded or molded into various shapes, such as pipe, pipe fittings, flanges or valves. Significant research has been dedicated to improving the interfacial adhesion between hydrophobic matrices and hydrophilic nanofillers.[34, 37, 49] Chemical, physical, and biological treatments help to improve the interfacial adhesion, which in turn enhances the overall properties of the resulting PMCs.[34, 38, 50-51] The low

cost of production and excellent properties of these materials have allowed them to replace many of the traditional more expensive and less adaptable materials, such as thermosets.[34] Thermoplastic composites have some distinct advantages over thermoset composites, such as high ductility, and toughness.[52] Thermoplastics are either semicrystalline or amorphous. Semicrystalline resins contain crystalline phases, whereas amorphous resins are completely disordered.[53]

Polyolefins are used in many different applications, from packaging to high-end performance materials. PP is known to be stiffer than HDPE, and its biaxial orientation results in films and containers with superior optical, and barrier properties.[53] These plastics feature a range of properties with a combination of lightweight, high-strength and are readily processed.[53]

1.4 Polypropylene (PP)

Polypropylene is a vinyl polymer in which a methyl group is bonded to every other carbon atom in the main chain, as shown in Figure 5.[53] High molecular weight polypropylene resins are prepared by the catalytic polymerization of propylene. In this process, heat, high-energy, and a catalyst are used to bond propylene monomers to form very long polymer chains. It is a highly useful material that has favorable physical properties, such as being, translucent, semi-rigid, tough, good fatigue, chemical and heat resistance.[53-56] Moreover, PP has a high resistance to flexing stress, low water absorption, excellent electrical resistance, lightweight, dimensional stability, high impact strength, and are non-toxic.[55]

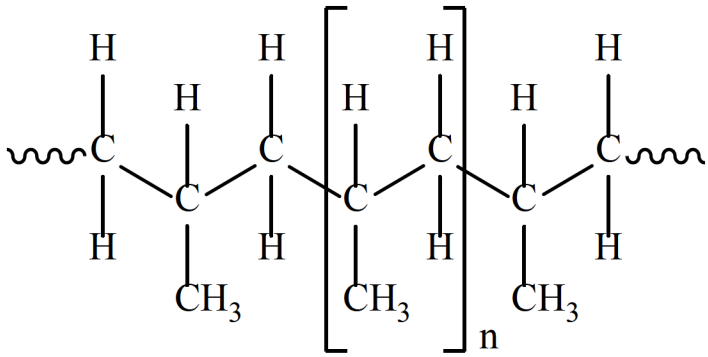

Figure 5. Polypropylene structure.[53]

Polypropylene is processed through many methods, such as melt-mixing, injection molding, and extrusion. The ability to produce many variations of a polymer material permits manufacturers to tailor PP resins for diverse applications, such as packaging films; rigid food containers; appliance parts; automotive bumper fascia and batteries; and medical syringes. In a medical environment, PP is suitable for items such as trays, funnels, pails, bottles, and instrument jars that have to be frequently sterilized.[53]

There are various types of polypropylene, such as homopolymer polypropylene (HPP), random copolymers (RCP), and impact copolymers (ICP). A polymer produced with identical monomers is called homopolymers, whereas polymers with more than one kind of monomer in their chains are known as copolymers.[53] The most commercially used polypropylene is homopolymer polypropylene, which contains both crystalline and non-crystalline regions. The amorphous regions have both isotactic PP and atactic PP. The advantages of HPP is its high level of stiffness at room temperature and high melting point. Some disadvantages include low transparency, as well as diminished impact

strength relative to PE.[53, 57] Propylene/ethylene copolymers, are considered random copolymers (RCP) that are formed in a single reactor by copolymerizing low amounts of ethylene (usually 7 wt.% or less) and propylene.[53] Incorporation of ethylene in PP causes disorder in the structure of polypropylene, which results in a reduction of crystalline order in the polymer. Propylene/ethylene copolymers have slightly better impact properties than all other polypropylenes, such as decreased melting points and enhanced flexibility. Impact copolymers (ICP) are physical blends of HPP and RCP with an overall ethylene content of approximately 6 to 15 wt.%. Impact polymers are ideal for use at low temperatures and exhibit with higher impact resistance.[53, 57]

1.5 Graft Copolymerization

Graft copolymerization has been widely used to improve the interfacial adhesion between the components in composite systems.[49] Alternatively, organic coupling agents are used to functionalize polymers by graft copolymerization, thus resulting in strong adhesion, even crosslinking, at the interface between filler and polymer matrix. In the maleation method, maleic anhydride (MA) has been used to functionalize polymers in the presence of a free radical initiator. MA is an α, β-unsaturated carbonyl compound, containing one carbon-carbon double bond (C=C) and two carboxylate groups (-C=OO-). This conjugated structure dramatically increases the graft reactivity due to the carbon-carbon double bond in the heterocyclic ring with the polymer matrix through the conjugate addition under a radical initiator, resulting in crosslinking or strong adhesion at the interface of a filler.[58] The concentration of the coupling agent determines the

coupling effectiveness in the composite. In general, mechanical properties increase with increased concentration of a coupling agent up to a specific limit, and then decrease or level off at higher concentrations.[59] The decline in mechanical properties at higher concentrations of coupling agents is due to 1) the formation of different by-products, 2) increase in the concentration of unreacted coupling agents, and 3) interference with the grafting reaction.[59-61] Therefore, an excess of a coupling agent is unfavorable to the grafting reaction and may act as an inhibitor of adhesion.[59]

In graft copolymerization, initiators are typically required, along with coupling agents during the grafting process. The most commonly used initiators are organic peroxides, including dicumyl peroxide (DCP), benzoyl peroxide (BPO), lauroyl peroxide (LPO), tert-butyl peroxy benzoate (TBPB) and di-tert-butyl peroxide (DTBPO).[59] In graft reactions, the concentration of peroxide is usually between 0.5-1 wt.%. An excess of peroxide may adversely affect the mechanical properties of the composite due to molecular chain scission of the polymer and filler.[59] DCP is a better initiator for MA compared with BPO because the free radicals of DCP have superior thermal stability that leads to better graft performance.[59] MA is commonly used for the functionalization and compatibilization of polyolefins and fillers due to the higher reactivity of the anhydride group toward successive reactions.[62-63] The succinic anhydride groups formed by the addition of maleic anhydride to a polymer by grafting, are highly reactive and can form covalent bonds with polar fillers and polymers. In several studies, a graft copolymer is used as a compatibilizer, where the polymer consists of a polyolefin backbone grafted with functional groups such as maleic anhydride with the incorporation of a polar filler.[55,

[64] MA on the non-polar backbone of polyolefins has overcome the disadvantage of the low surface energy of these polymers, improved surface hydrophilicity for the benefit of printing and coating applications, and adhesion with polar polymers such as polyamides, metals, glass, and cellulose fibers.[65-66]

1.6 Graft Copolymerization of Polypropylene

The functionalization of PP with polar monomers is an effective way to add polar groups to polypropylene and increase its affinity with polar materials.[49] These types of grafted polymers have been widely used to improve properties of polypropylene such as polarity, interfacial adhesion with metals, ceramics, and compatibility with natural fillers, polyamides, and polyesters.[49, 67]

Melt-reactive processing is an attractive route to fabricate new PP composites. The grafting of maleic anhydride onto PP by reactive processing involves a reaction between the polymer melt and maleic anhydride in the presence of an organic peroxide. During processing, the organic peroxides undergo hemolytic scission at the oxygen-oxygen bonds to form primary free radicals.[68] The grafting process is initiated when the radicals abstract hydrogen atoms from the PP chains forming macro radicals on the polymer backbone. Figure 6 is a representation of this reaction in a simplified manner; where *I* represents the initiator, and $R\cdot$ represents the free radical formed. However, such reactions can be accompanied by chain scission, which alters the rheologic characteristics of PP. Finding the ideal conditions of the grafting process involves a significant number

of variables, including coupling agent concentration, type, and concentration of peroxide, reaction time and temperature, rotor speed, and the addition sequence of the reagents.[49]

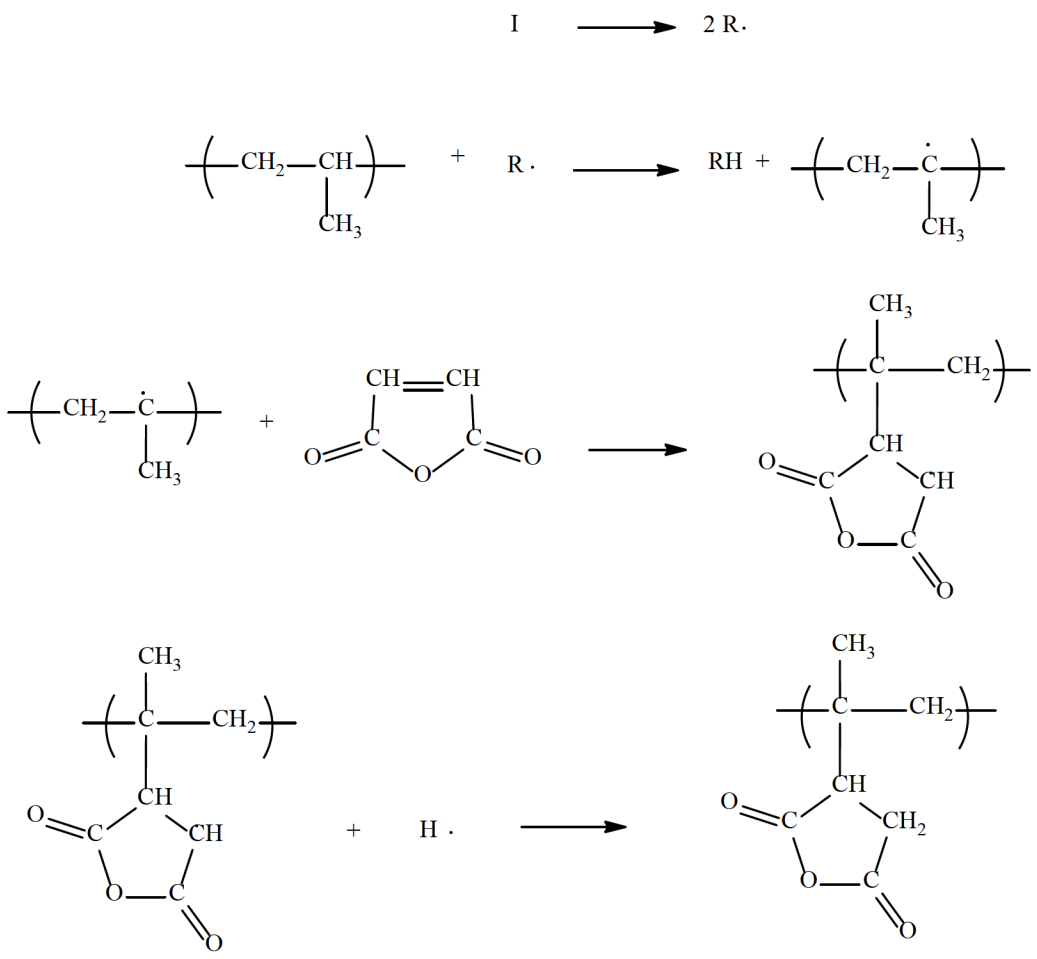

Figure 6. Maleic anhydride (MA) grafting reaction with polypropylene.[49]

Recent work suggests that the use of MA-grafted PP (MAPP) significantly improves the filler–matrix adhesion.[69] There have been many studies devoted to the use of filler/PP composites containing the coupling agent MAPP. Yuan et al. used MAPP as

a coupling agent for PP-waste newspaper flour composites and reported improved mechanical properties.[70] Sanadi et al. reported that the improvement in properties using MAPP depends on the amount of MA in the graft copolymer and the molecular weight of the copolymer.[71] Similarly, Pracella et al. studied hemp/PP composites,[72] Arbelaiz et al. focused on flax/PP composites,[73] Sam-Jung et al. worked on cotton/PP composites,[74] and all of them found that the incorporation of MA resulted in improved mechanical properties of the corresponding composites. At higher MAPP content, a minimal decrease in mechanical properties has occurred, which may be due to the self-entanglement of MAPP, resulting from the migration of excess MAPP around the fiber surface rather than causing inter-chain entanglement and contributing to the mechanical stability of the system.[70] When MAPP is used as coupling agent, bonding between the anhydride groups of MAPP and hydroxyl groups of the cellulosic fibers occurs as shown in Figure 7.[75-76] This is the possible reinforcement mechanism for nanocellulose/polymer composites containing MAPP. Studies that correlate to this research show that the functional group, [-$(C=O)_2$ O-] of maleic anhydride, interact with the polar groups, mainly hydroxyl groups (-OH) of cellulose and lignin to form covalent or hydrogen bonds.[51, 59, 77] MAPP increases the mechanical properties of natural fiber/PP composites, but the content of MAPP should not be high.[74]

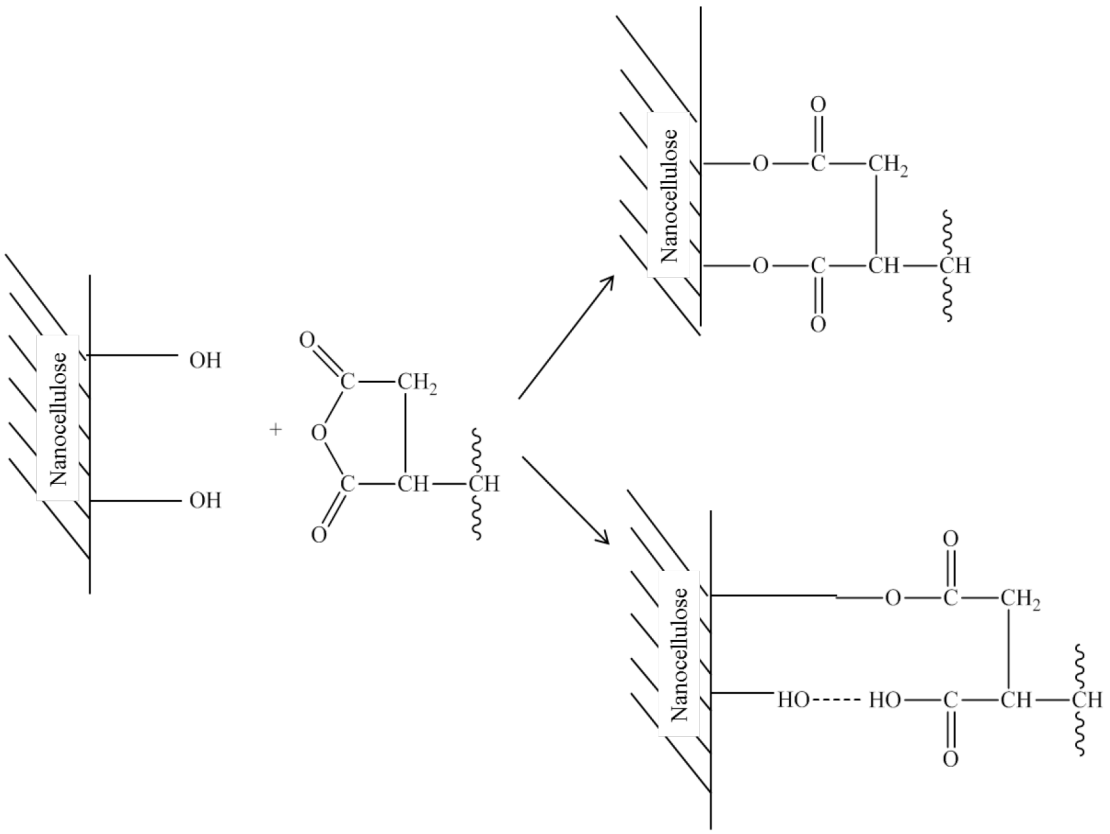

Figure 7. Bond formation between hydroxyl groups of nanocellulose and anhydride ring of maleated polypropylene (MAPP).[55]

The surface modification of CNFs by MAPP was also found to be beneficial for the reinforcement of PP.[38] Composites composed of PP and MAPP-modified CNFs was prepared using a twin-screw co-rotating extruder. However, there was only a 1% increase in the tensile strength of the nanocomposite compared to neat PP. Performing a similar approach, Wang et al. reported a 26% increase in Young's modulus in PP/CNFs nanocomposite containing 10 wt.% of CNFs and 2 wt.% of MAPP.[78] Ferrer et al. used lignocellulosic fibers for the reinforcement of PP.[79] In this study, the CNFs contained approximately 9 wt.% of lignin that acted as the compatibilizer resulting in improved

dispersion of CNFs in the PP matrix and exhibiting a 15% increase in the tensile modulus with respect to neat PP. Iwamoto et al. added 5 wt.% of MAPP to improve the interfacial adhesion to reinforce PP with lignocellulose nanofibers (L-CNF).[80] Thus, these works show that MAPP is a promising compatibilizer for PP composites and can increase the mechanical properties of natural fillers in PP.[78-80]

1.7 Polyethylene (PE)

Polyethylene is a thermoplastic polymer with a variable crystalline structure composed of ethylene monomers as shown in Figure 8.[81] Polyethylene grades are generally classified into three categories: low-density polyethylene (LDPE) with long branches, linear low-density polyethylene (LLDPE) with short branches and high-density polyethylene (HDPE) composed of linear chains.[82] Ultra-high molecular weight polyethylene (UHMWPE) is a particular case of HDPE characterized by very long chains. HDPE has a molecular weight that is typically between 50,000 and 250,000 g/mol, while that of UHMWPE is approximately 3.5 to 7 million g/mol. There are numerous applications for polyethylenes; however, certain applications are more or less well suited.[83] For example, LDPE is generally used in plastic packagings such as for grocery bags or plastic wrap; HDPE, by contrast, has common applications in construction.[81, 83] Ultra-high molecular weight polyethylene has high-performance applications in areas such as medical devices and bulletproof vests.[1, 3]

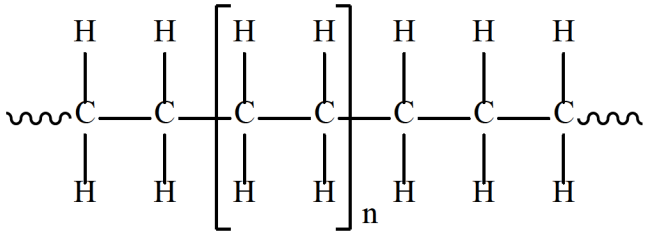

Figure 8. Polyethylene structure.[81]

1.8 High-Density Polyethylene (HDPE)

High-density polyethylene (HDPE) has a linear structure and no or low degree of branching, produced by catalytic polymerization of ethylene in either a slurry suspension, solution or gas phase reactors. The polymer chain is approximately 500,000 to 1,000,000 carbon units long.[83] HDPE properties include high impact strength, abrasion-resistant, and a low coefficient of friction.[83] HDPE nanocomposites have attracted considerable interest because they exhibit enhanced mechanical, thermal, and barrier properties.[84] These nanocomposites are used in a variety of applications including packaging for consumer products, plastic parts for various industries; automotive industry, particular devices like living hinges, and textiles.[83, 85] It has been shown that due to the weak interfacial bonding between CNCs and PE matrix, a decrease in yield stress and modulus of elasticity was observed for PE/CNC nanocomposites relative to neat PE.

1.9 Graft Copolymerization of High-Density Polyethylene (HDPE)

Polyethylene is the most commonly used polyolefin and has no polar groups in its backbone. Therefore, challenges have been encountered in preparing a homogeneous dispersion of hydrophilic nanoparticles. For example, Heidarbeigi et al. found a decrease

in yield stress and Young's modulus for PE/CNC nanocomposites due to the weak interfacial bonding between CNCs and the PE matrix. Chemical modification of HDPE has been used successfully to overcome problems associated with poor phase adhesion in polymer/filler systems.[86] Coupling agents have been added to promote compatibility, induce interaction between the phases, reduce the interfacial tension, and increase the adhesion between materials, which makes the nanocomposite more homogeneous.[86] The decrease in interfacial tension is dependent on the presence, and concentration of the coupling agent, as mentioned in section 1.6.[49] The coupling agents commonly grafted onto polyethylene are unsaturated functional monomers, such as maleic anhydride and acrylic acid (AA) and their derivatives.[34] Gaylord et al. patented maleic anhydride as a coupling agent to react with cellulose and polyethylene (PE) or polyvinyl chloride (PVC) in the presence of a free radical initiator.[87] The functionalization of HDPE with MA through a free radical reaction in both solution and melt processes have been studied, extensively.[66-67, 87-88] The functionalization lowers the hydrophobicity of polyethylene, imparting polarity, which makes it more compatible with polar and hydrophilic materials. MA is suitable for grafting onto polyethylene because of its low reactivity towards itself and its ability to graft onto the polymer with a free radical initiator. MA grafting adds polar groups onto the polyethylene backbone, and this reaction can be carried out in a single processing step. Figure 9 presents this reaction in a simplified manner; where *I* represent the initiator (organic peroxide), and $R\cdot$ represents the free radical formed.[86]

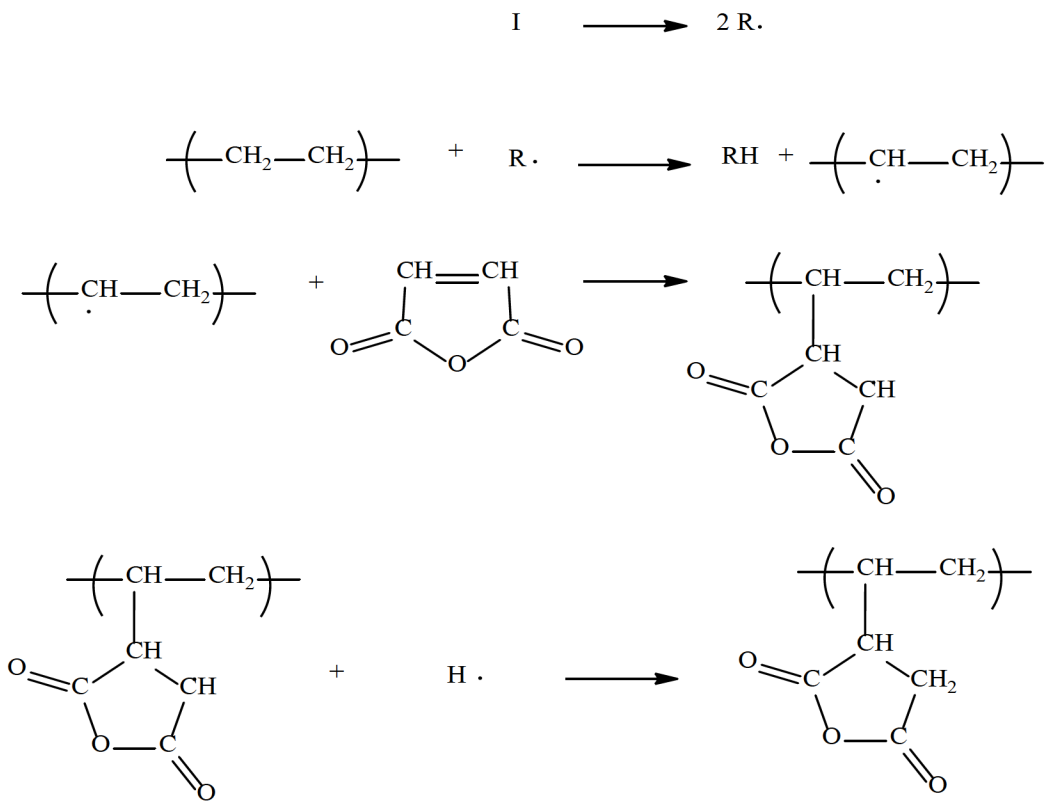

Figure 9. Maleic anhydride (MA) grafting reaction with polyethylene.[86]

The polyethylene macro-radical subsequently reacts with MA monomer. Many side reactions can also take place during this free-radical grafting reaction. For example, secondary formed macro-radicals undergo a coupling reaction to produce a cross-linked product. The details of the grafting mechanism of MA onto polyethylene with a radical initiator may be found in various reports.[86, 89] Wang et al.[90] suggested that polyethylene has a high grafting level of maleic anhydride at 0.1 wt.%. Recent work on clay/polyethylene nanocomposites indicated that clay could be exfoliated excessively, due to the addition of maleated polyethylene.[91-92] Polyethylene (PE)/organoclay (MMT)

nanocomposites containing maleated polyethylene (PE-*g*-MA) were studied by Liang et al.[93] The results indicated a significant increase in complex melt-viscosity, storage modulus, and loss modulus under shear stress relative to neat polymer.[94] They found that MMT intercalation in PE/PE-g-MAH/organo-MMT could be enhanced by increasing the content of PE-g-MAH and that the improved dispersion led to significant increases in the stiffness and flame resistance of the nanocomposite.[94] Therefore, these works show that MAPP is a promising compatibilizer for HDPE composites and will increase the mechanical properties of natural fillers in HDPE.

1.10 Ultra-High Molecular Weight Polyethylene (UHMWPE)

UHMWPE is synthesized by a Ziegler-Natta polymerization with the use of a titanium chloride catalyst.[83] UHMWPE is well-known for its ultra-high toughness combined with high abrasion resistance, low coefficient of friction, impact resistance, low moisture uptake, and excellent chemical resistance.[82] Because of these properties, UHMWPE is used for a variety of applications, including bullet-proof body armor, sports goods such as skis and snowboards, and total hip replacements.[95] UHMWPE shows excellent performance in short-term applications but, its low melting temperature, poor creep recovery, and self-lubricating property limits its long-term applications. For many applications, it is highly desirable to improve the UHMWPE toughness and stiffness. Several efforts have been made to achieve desired properties by various approaches such as blending UHMWPE with other high-performance polymers or using nanofillers such as carbon nanotubes, clay, graphene, carbon black, and hydroxyapatite.[96-98] The addition

of these nanofillers resulted in significant improvement. Several methods have been implemented to improve the dispersion and compatibility of nanofillers with UHMWPE which includes surface treatment of nanofillers, powder sintering, and dry/ball mixing.[99-101] Furthermore, UHMWPE is an extremely viscous polymer and thus cannot be processed conventionally, typically resulting in a reduced dispersion of reinforcing agents. These critical issues are particularly crucial for the fabrication of UHMWPE nanocomposites due to its non-polarity, which limits interaction between filler and matrix polymer.

Addition of CNCs in polyolefins such as polypropylene and polyethylene, specifically high-density polyethylene and ultra-high molecular weight polyethylene significantly improved the rate of crystallization and slightly improved mechanical properties.[102-105] However, incorporation of CNCs in UHMWPE resulted in no significant improvement in the properties due to poor dispersion and incompatibility with hydrophobic UHMWPE.[106]

1.11 Processability of Thermoplastic Nanocomposites

A challenging problem in preparing nanocomposites is the desire to achieve a homogenous dispersion of the filler in the polymer matrix. Therefore, researchers have focused on using processing methods and conditions which maximize dispersion, avoiding large-scale agglomeration and the formation of a network structure when incorporating cellulose nanocrystals in a polymer matrix.[55] Literature reports four processing methods that have been utilized to produce nanocellulose thermoplastic

composites. Those techniques are: melt compounding,[107-108] powder sintering,[109] partial dissolution,[107] electrospinning.[17] Melt compounding, involves the incorporation of reinforcing agents in polymer matrices by way of thermal-mechanical mixing; followed by optional compression molding into test specimens. During processing, it is important to control processing parameters to prevent degradation caused by temperature, time, and shear stress.[49] Studies have reported efforts to improve the dispersion of CNCs in hydrophobic polymer matrices such as PLA, PP, and PE.[110-112]

Some thermoplastics, such as UHMWPE, are more difficult to fabricate by conventional melt processing techniques.[98, 113] As a result, these polymers are processed by the powder processing technique, which involves cold compaction of the polymeric powders followed by sintering of the preforms at elevated temperatures. The properties of such products are governed by several process variables employed during the compaction and sintering processes. The compaction involves pressing the polymeric powder in a closed rigid die. During the compaction process, particle rearrangement, elastic deformation at contact points, and finally, the compression of the material takes place. The sintering process consists of heat treatment of the compacted polymer product or the preform as per a well-defined temperature program.[109]

UHMWPE nanocomposites with 0, 0.5, 1, 2, and 5 wt.% loading of L-CNCs and 1, 2, 5, 17, and 20 wt.% loading of L-CNFs were prepared for us by Crown Plastics using a sintering method. I investigated the incorporation of 0, 0.5, 1, 2, and 5 wt.% of L-CNCs in HDPE and PP by high-torque melt-mixing. Compression molding was utilized

to produce panels for thermo-mechanical characterization by DSC, DMA, TGA, melt-rheology, and tensile testing. This research is a comprehensive guide to understand the processing and experimental conditions for the incorporation of lignin-coated nanocellulose in producing a nanocomposite.

CHAPTER 2

EXPERIMENTAL METHODS

2.1 Materials

American Process Inc. Atlanta, GA, provided spray-dried cellulose nanocrystals (CNCs) and cellulose nanofibers (CNFs) prepared by the AVAP process. The AVAP L-CNCs have an average length and diameter of ~350 nm, and ~5-7 nm and AVAP L-CNFs are 5 - 200 nm wide, 500 nm to several microns in length, and were produced from eucalyptus chips.[39]

Ultra-high molecular weight polyethylene (UHMWPE) sheets are approximately 14 inches wide, 0.5 inches thick and several feet long containing 0.5, 1, 2, and 5 wt.% loading of L-CNCs and 1, 2, 17, and 20 wt.% of loading of L-CNFs were prepared by a powder sintering process and were provided by Crown Plastics, Inc., Plymouth, MN.[114] The samples were designated as neat UHMWPE, 0.5% L-CNCs/UHMWPE, 1% L-CNCs/UHMWPE, 2% L-CNCs/UHMWPE and 5% L-CNCs/UHMWPE, respectively, for UHMWPE containing 0, 0.5, 1, 2, and 5 wt.% L-CNCs and 0.5% L-CNFs/UHMWPE, 1% L-CNFs/UHMWPE, 2% L-CNFs/UHMWPE 17% L-CNFs/UHMWPE and 20% L-CNFs/UHMWPE, respectively, for UHMWPE containing 0, 0.5, 1, 2, 17, and 20 wt.% L-CNFs.

High-density polyethylene (HDPE) pellets (commercial code AL55-003) and Isotactic Polypropylene (PP) pellets (commercial code PDH-052/random copolymer) were supplied by ExxonMobil, Baytown, TX. Maleic anhydride (MA) was purchased from MATHESON COLEMAN & BELL Manufacturing Chemist Norwood, OH, and dicumyl peroxide (DCP) from ACROS ORGANICS, Geel, Belgium.

2.2 Experimental Procedures

2.2.1 Preparation of L-CNCs/Polyolefin Nanocomposites

A Hakke Rheocord 90 mixer with sigma blade attachments was used to intimately melt-mix L-CNCs and polyolefins, PP and HDPE, using a combination of thermal and mechanical energy. The masses of components used in the melt mixing are given in Tables 2 and 3. The samples were prepared by adding the polymer to the melt-mixer over 3 min, followed by the addition of L-CNCs over 5 min and then melt-mixing continued for a total of 10 min. An initial temperature of 170 °C was used for PP and 140 °C for HDPE with a mixing rate of 40 rpm in both cases. The 5% masterbatches of PP and HDPE were melt-mixed with neat PP or HDPE, respectively, to prepare 0.5, 1, and 2 wt.% L-CNCs nanocomposites. The mixing process temperature increased an average of 198 °C for PP and 158 °C for HDPE after the addition of L-CNCs. Upon completion of mixing, samples were cooled to room temperature.

Polyolefin were compression molded with a three-piece tool. Samples were loaded into the bottom plate and picture frame of the tool and inserted into a preheated (180 - 200 °C) Wabash hot press. After allowing the sample to melt into the bottom

portion of the tool, the top plate was added and the sample was compressed under 5 tons of pressure. After compression molding for 5 min, the tool was removed from the press and rapidly cooled at room temperature.

Table 2. Mass of HDPE and L-CNCs Mixed for this Study to Prepare Nanocomposites.

	Percent Loading		
Components	0.5	1	2
HDPE (g)	45.880	40.132	30.022
5% L-CNCs/HDPE (g)	5.025	10.258	20.147
Total (g)	50.905	50.390	50.169

Table 3. Mass of PP and L-CNCs Mixed for this Study to Prepare Nanocomposites.

	Percent Loading		
Components	0.5	1	2
PP (g)	45.331	40.069	30.125
5% L-CNCs/HDPE (g)	5.152	10.272	20.007
Total (g)	50.483	50.341	50.132

2.2.2 Preparation of Polyolefin-*g*-MA Nanocomposites

A Hakke Rheocord 90 mixer with sigma blade attachments was used to carry out the grafting reactions of L-CNCs and PP and HDPE, via melt-mixing. Samples ranging from 0.5 to 5 wt.% L-CNC loading were prepared for the comparison of filler/reinforcement effects with the samples prepared as described in Tables 4 and 5. The MA grafted samples were prepared by initially melt-mixing the polymer pellets for 3

min, followed by the addition of DCP for 30 seconds. MA was added, and melt-mixed for 2 min, and then the appropriate amount of L-CNCs were added, and melt mixing continued for a total of 11 min. An initial melt-mixer temperature of 170 °C was used for PP and 140 °C for HDPE with a mixing rate of 40 rpm. The mixing process temperature increased an average of 198 °C for PP and 158 °C during processing. Upon completion of mixing, samples were removed from the mixer and cooled to room temperature.

Polyolefin nanocomposites with various loadings of nanocellulose were processed by compression molding with a three-piece tool to produce flat panels. The sample was loaded into the bottom plate and picture frame of the tool and inserted into the preheated (150 - 180 °C) Wabash hot press. After allowing the sample to melt into the bottom portion of the tool, the top plate was added, and the sample was compressed under 5 tons of pressure. After compression, the tool was removed from the press and rapidly cooled at room temperature.

Table 4. Mass of HDPE, L-CNCs, MA, and DCP Mixed for this Study to Prepare Nanocomposites.

	Percent Loading			
Components	0.5	1	2	5
HDPE (g)	48.253	48.122	47.518	46.014
L-CNCs (g)	0.255	0.513	1.018	2.509
MA (g)	1.512	1.521	1.505	1.514
DCP (g)	0.104	0.11	0.107	0.101
Total (g)	50.124	50.266	50.148	50.138

Table 5. Mass of PP, L-CNCs, MA, and DCP Mixed for this Study to Prepare Nanocomposites.

Components	Percent Loading			
	0.5	1	2	5
PP (g)	48.270	48.347	47.534	46.437
L-CNCs (g)	0.201	0.542	1.018	2.541
MA (g)	1.550	1.518	1.505	1.534
DCP (g)	0.170	0.151	0.125	0.113
Total (g)	50.191	50.558	50.182	50.625

2.3 Characterization

2.3.1 Differential Scanning Calorimetry (DSC)

A TA Instruments Q2000 Differential Scanning Calorimeter was used for recording the DSC thermograms under N_2. To ensure the reliability of the data obtained, heat flow and temperature were verified monthly by running an indium and sapphire standards and recalibrated in needed. Samples of approximately 6-10 mg were weighed and hermetically sealed in aluminum pans.

Neat UHMWPE and UHMWPE nanocomposites were heated to 180 °C at a heating rate of 50 °C/min under a nitrogen atmosphere and held for 5 min to remove thermal history. The crystallization temperature (T_c) and melting temperature (T_m) were measured by cooling the samples from 180 to -75 °C, and then reheating to 180 °C at a ramp rate of 10 °C/min.

Non-isothermal and isoconversional studies were carried out by heating samples from 25 °C to 180 °C at a heating rate of 50 °C/min and held for 5 min at 180 °C to remove thermal history and then cooled to 25 °C, at cooling rates 1, 5, 10, 15 and 20 °C/min. The heat flow as a function of time and temperature were recorded at different cooling rates for all the samples.

Neat HDPE, L-CNCs/HDPE, and HDPE-g-MA nanocomposites samples were heated to 180 °C at a heating rate of 50 °C/min under a nitrogen atmosphere and held for 5 min to remove thermal history. The T_c and T_m were measured by cooling and heating samples from 180 to 25 °C and 25 to 180 °C at a ramp rate of 10 °C/min.

Non-isothermal studies were investigated by heating each sample from 25 °C to 180 °C at a heating rate of 50 °C/min to remove any thermal history and then cooled to 25 °C at different cooling rates (1, 5, 10, 15 and 20 °C/min). The exothermic curves of the heat flow as a function of time were recorded at different cooling rates for each sample.

Neat PP and L-CNCs/PP, PP-g-MA nanocomposites were heated from 25 to 180 °C at a heating rate of 50 °C/min under a nitrogen atmosphere and held for 5 min to remove thermal history. The T_g, T_c, and T_m were investigated by cooling and heating samples from -75 to 180 °C and 180 to -75 °C at a ramp rate of 10 °C/min. Analyses of all sample data were conducted using TA instruments, Universal Analysis Software.

2.3.2 Dynamic Mechanical Analysis (DMA)

The storage modulus (G'), loss modulus (G'') and the mechanical loss factor (tan δ = G''/G') as a function of temperature (T) were assessed by dynamic mechanical analysis (DMA) using a TA instruments, AR-G2 in tension mode. The samples were thin rectangular strips with dimensions of approximately 30.0 x 11.0 x 2.50 mm^3. Neat PP and PP nanocomposites thermal behavior was investigated by heating the samples from 30 °C to 200 °C at a heating rate of 3 °C/min in tension mode at 1 Hz, and 0.005% strain.

Temperature ramp measurements of neat HDPE and HDPE nanocomposites thermal behavior was investigated by heating the samples from 30 °C to 135 °C at a heating rate of 3 °C/min in tension mode at 1 Hz, and 0.1% strain. Time sweep measurements were performed at 1 Hz, at a constant temperature of 30 °C for 5 min.

The viscoelastic properties of neat UHMWPE and UHMWPE nanocomposites were determined by dynamic mechanical analysis. The elastic modulus (E'), loss modulus (E''), and the mechanical loss factor (tan δ = E''/E') as a function of temperature (T), were assessed by dynamic mechanical analysis (DMA) using a Netzsch DMA 242E instrument in tensile mode.. Samples with dimensions 15.00 x 3.20 x 1.50 mm^3 were cut from UHMWPE sheets and analyzed in tensile mode. The DMA experiments were performed from -170 °C to 125 °C at a heating rate of 2 °C/min, at frequencies of 0.1, 1, 10, and 50 Hz and the samples underwent cyclic strain with fixed amplitude of displacement equal to 45 μm (dynamic force of 11.750 N, and static force of 0.050 N). Analyses of all samples were conducted using Proteus Analysis Software.

2.3.3 Thermogravimetric Analysis (TGA)

The thermal degradation of UHMWPE, HDPE, and PP nanocomposites were evaluated using thermogravimetric analysis (TGA) on a TA Instruments model TGA-Q50. Samples, 10-20 mg, prepared as described in sections 2.2.1 and 2.2.2 were weighed on a platinum pan on the TGA and then heated at 20 °C/min from temperatures, 30 to 800 °C. Analyses of all samples were conducted using TA instruments, Universal Analysis Software.

2.3.4 Tensile Testing

All samples were cut according to ASTM D-638, dog-bone Type IV, and to reduce experimental error, at least five replicate tests were performed for each sample material. UHMWPE nanocomposite samples were measured according to ASTM D-638 on an Instron 8505 electromechanical test frame equipped with a digital controller and computer data acquisition, under a displacement-control loading rate of 1.0 in/min with the use of a non-contact laser extensometer to measure strain as a function of applied load at room temperature. The analysis was then conducted using TESTWORKS software to record all data and runs.

The PP and HDPE nanocomposite samples were measured according to ASTM D-638 on an MTS electromechanical test frame equipped with the use of a contact-strain gauge to measure strain as a function of applied load at room temperature at a crosshead speed of 2.0 in/min. The analysis was then conducted using TESTWORKS software to record all data and runs.

2.3.5 Melt-Rheology

The rheological properties of PP and HDPE nanocomposites and neat samples were measured using a TA Instruments AR-G2 rheometer, using 25 mm aluminum plates using plate-plate geometry with chamber temperatures of 150 °C for HDPE and 175 °C for PP. For strain sweep and frequency sweep tests, melt-mixed samples were compressed and cut into 25 mm diameter plates and preconditioned at 5 degrees below melt-temperature for 15 min. Strain sweeps within the range of 0-2% were conducted on neat HDPE, PP, L-CNCs nanocomposites, and functionalized nanocomposites. At 1 Hz, the most sensitive rheological parameter was found to be stable at 0.1% strain. For this reason, the dynamic (frequency sweep) tests were performed at a strain of 0.1%. The resulting storage modulus (G'), loss modulus (G''), tan δ and dynamic viscosity (*η) were plotted as a function of frequency in the range of 0.01 to 100 Hz at 0.1% strain in the linear viscoelastic region.

2.3.6 Scanning Electron Microscope (SEM)

Studies on the morphology of the tensile fracture surfaces of UHMWPE nanocomposites were carried out using an Agilent Technologies 8500 Field Emission SEM operating at high vacuum and 25 kV, to study the morphology of the neat UHMWPE and UHMWPE nanocomposites. The fractured ends of specimens were mounted on aluminum stubs and sputter-coated with a thin layer of gold to avoid electrostatic charged during the examination. The surface morphology of all samples was compared.

2.3.7 Optical Microscopy

Crystalline morphology of nanocomposites and the distribution of L-CNCs in polymer matrices, PP, and HDPE were observed using an optical microscope. Samples were melted and squeezed between a microscope cover glass at 180 °C for 10 minutes and then quenched to room temperature. The thickness of the samples prepared by melt-pressing was less than ideal for analyzing the L-CNC distribution by optical microscopy.

CHAPTER 3

ULTRA-HIGH MOLECULAR WEIGHT POLYETHYLENE (UHMWPE) NANOCOMPOSITES RESULTS & DISCUSSION

3.1 General Overview

Cellulose nanocrystals (CNC) and cellulose nanofibers (CNF) have excellent reinforcing properties due to hydrogen bonding, which is responsible for the crystalline structure of cellulose fibers resulting in its high tensile strength and modulus.[20] In some cases, the addition of modified and non-modified CNCs to polymer matrices such as poly(lactic acid), polyvinyl alcohol, polyethylene, poly(ethylene terephthalate), polypropylene, polyamide, poly(methylmethacrylate), and polyethylene oxide significantly improved mechanical properties and the rate of crystallization.[102-103, 105, 115] However, incorporation of CNCs in ultra-high molecular weight polyethylene (UHMWPE) resulted in no significant improvement in these properties due to poor dispersion and incompatibility with the hydrophobic matrix of UHMWPE.[106] American Process Inc., developed a process to deposit lignin onto the surface of its CNCs and CNFs in situ, thus producing nanocellulosic materials with a hydrophobic interface, lignin-coated cellulose nanocrystals (L-CNCs) and lignin-coated cellulose nanofibers (L-CNFs). Lignin has hydrophobic regions and is non-covalently attached to cellulose, which prevents re-aggregation of CNCs during processing and also improves interaction with the hydrophobic polymer matrix.[39-40] Coating lignin on the surface of CNCs has

been shown to be a practical approach to enhance the dispersion of CNCs in hydrophobic polymer systems.[42-43] Previously, Marshall et al. showed that nanocellulose prepared by the AVAP process is more thermally stable than CNCs and CNFs produced by sulfuric acid hydrolysis and the TEMPO process.[39, 41]

Although the crystallization kinetics of low-density polyethylene (LDPE) and high-density polyethylene have been widely studied, the crystallization kinetics of UHMWPE has not received the same attention.[116-119] For the present study, L-CNCs/UHMWPE and L-CNFs/UHMWPE nanocomposites were prepared for us by Crown Plastics, Inc., by the powder sintering process.[114] The thermomechanical properties and crystallization kinetics of the corresponding nanocomposites were investigated by DSC, tensile testing, DMA, TGA, and SEM.

3.2 Crystallization Behavior of L-CNCs/UHMWPE Nanocomposites

Figure 10 shows a depiction of the L-CNCs/UHMWPE nanocomposites, which exhibited a uniform light-brown to dark-brown color as the L-CNC loading increased. UHMWPE samples were designated as neat UHMWPE, 0.5% L-CNCs/UHMWPE, 1% L-CNCs/UHMWPE, 2% L-CNCs/UHMWPE and 5% L-CNCs/UHMWPE, respectively for UHMWPE containing 0, 0.5, 1, 2, and 5 wt.% L-CNCs. Crystallization and melting behavior of UHMWPE in the presence of L-CNCs were investigated by analyzing DSC thermograms. Figure 11 shows the DSC scans on cooling from 180 to 30 °C and the second heating scans at 10 °C/min for neat UHMWPE and L-CNCs/UHMWPE nanocomposites. The DSC scans show the presence of a crystallization exotherm, T_c, on

cooling, and a melting endotherm, T_m, on heating. The enthalpy of melt (ΔH_m) was determined from the area of the melting endotherm, and the DSC results are summarized in Table 6. From the ΔH_m values, percent crystallinity was calculated using Equation 1:[120]

$$X_c = \frac{\Delta H_m}{(1 - mass\ of\ L-CNC) \times \Delta H_m^0} \times 100 \quad (1)$$

where X_c is the degree of crystallinity, ΔH_m is the enthalpy of melt for the sample, and ΔH_m° is the standard enthalpy of melt for 100% crystalline UHMWPE, taken from the literature as 288.0 J/g.[120] DSC showed that the degree of crystallinity for the nanocomposites decreased with increasing L-CNC loading and that the onset of crystallization temperature of UHMWPE decreased upon the incorporation of L-CNCs. The decrease in percent crystallinity was due L-CNCs, hindering chain diffusion and folding at the crystal growth front and results in thin spherulite lamellar thickness.[121-122] Incorporation of L-CNCs showed virtually no change in the melting behavior of UHMWPE upon heating, indicating that the addition of L-CNCs had little effect on UHMWPE crystals formed. Similar behavior was observed for carbon nanotubes in high molecular weight poly(trimethylene terephthalate) matrix.[123]

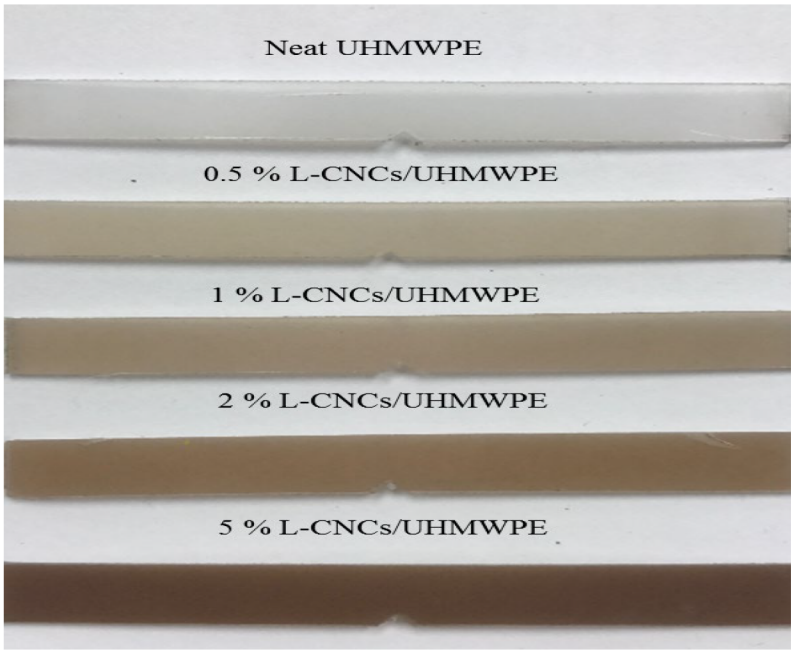

Figure 10. Optical image of UHMWPE samples which were designated as neat UHMWPE, 0.5% L-CNCs/UHMWPE, 1% L-CNCs/UHMWPE, 2% L-CNCs/UHMWPE and 5% L-CNCs/UHMWPE, respectively for UHMWPE containing 0, 0.5, 1, 2, and 5 wt.% L-CNCs.

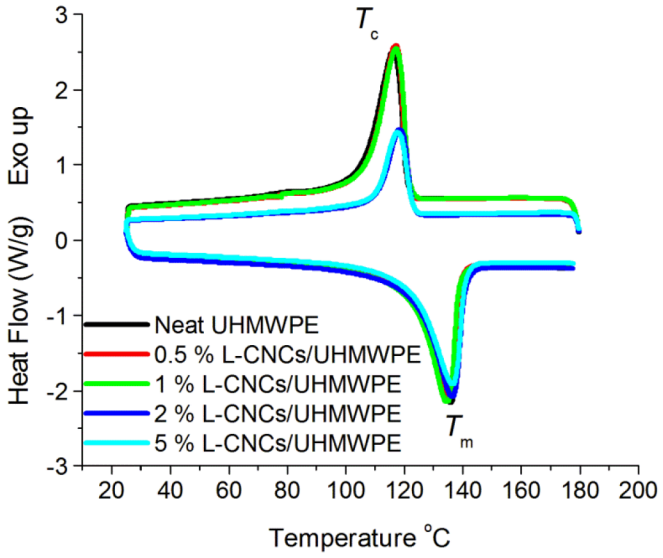

Figure 11. DSC scans for neat UHMWPE and L-CNCs/UHMWPE nanocomposites at heating rate of 10 °C/min.

Xu et al suggested that the non-nucleating behavior of CNCs in UHMWPE is due to the very high molecular weight of the polymer.[124] High molecular weight homopolymers always possess some topological defects such as chain entanglement, loops, or knots in the melt.[124] These structures do not participate in the crystallization process and are relegated to the non-crystalline region as the transformation progresses.[124-125] UHMWPE has been found to contains many entanglement points due to its very high molecular weight.[124] To further understand the role of L-CNCs on the crystallization behavior of UHMWPE, the crystallization kinetics of L-CNCs/UHMWPE nanocomposites were studied in this work.

Table 6. Thermal Parameters of Neat UHMWPE and L-CNCs/UHMWPE Nanocomposites Derived from Cooling and Second Heating Scan.

Sample designation	ΔH_m (J/g)	Onset of T_c (°C) peak	T_m (°C)	X_c (%)
neat UHMWPE	200.3	123.7	135.8	69.5
0.5% L-CNCs/UHMWPE	175.6	123.0	134.7	61.3
1% L-CNCs/UHMWPE	174.0	122.8	134.6	61.6
2% L-CNCs/UHMWPE	161.4	122.7	136.4	56.6
5% L-CNCs/UHMWPE	163.0	119.3	136.6	59.6

3.3 Non-Isothermal Crystallization of L-CNCs/UHMWPE Nanocomposites

Non-isothermal kinetics of neat UHMWPE and L-CNCs/UHMWPE nanocomposites were investigated by DSC to determine the process of nucleation and crystal growth by applying Avrami's model.[126]

The cooling scans of neat UHMWPE and L-CNCs/UHMWPE nanocomposites were recorded at cooling rates of 1, 5, 10, 15, and 20 ˚C/min and are shown in Figure 12. Results show that with increasing cooling rates, the exotherms shift to lower temperatures, indicating that with higher cooling rates, the UHMWPE starts crystallizing at lower temperatures, which is a common phenomenon for polymers.[124] The data also demonstrates that, with increasing supercooling, the characteristic time of crystallization decreases as a result of increasing thermodynamic driving force for crystallization, leading to a continuous increase in both the rate of crystal nucleation and growth. It has been reported that the "melt-crystallization of macromolecules is limited to the temperature range between the equilibrium melting temperature ($T_{m,0}$) and a temperature T_{∞}, which is assumed to be 30-50 K below the glass transition temperature,T_g."[127] Supercooling is defined as the difference between $T_{m,0}$ and the crystallization temperature, and generally leads to an increase in the crystallization rate in response to a lower crystallization temperature and, subsequently, to a decrease as the temperature approaches T_g.[127] Low cooling rates provide enough time for the material to nucleate; however, high cooling rates do not. Thus, crystallization starts at higher temperatures with low cooling rates. On the contrary, at high cooling rates, the UHMWPE does not have enough time to nucleate; thus, crystallizing occurs at lower temperatures.[124]

In general, the heat generated during the polymer crystallization process is linearly proportional to the evolution of crystallinity.[126] Thus, the degree of crystallinity (X_t) as a function of crystallization time (t) can be calculated using Equation 2.[126]

$$X_T = \frac{\int_{T_0}^{T_c} \frac{dH}{dT} \cdot dt}{\int_{T_0}^{T_\infty} \frac{dH}{dT} \cdot dt} \quad (2)$$

where dH is the enthalpy of crystallization released within an infinitesimal temperature range dT, T_0 denotes the initial crystallization temperature, and T_∞ is the temperature required to complete the crystallization process and T_c is the temperature when the crystallization process is completed. The plots of the degree of crystallinity versus time are shown in Figure 13. It can be seen from the curves of the Avrami plots that three sections with different slopes can be distinguished; an initial stage from the beginning of the crystallinity until 5% crystallinity followed by primary crystallization with a higher slope that extends to 60 - 80% crystallinity. This stage is then followed by a final phase of crystallization with a significantly lower slope due to the secondary crystallization and crystal impingement. These results show that the presence of L-CNCs had no significant effect on the rate of crystallization of UHMWPE, and the time required for complete crystallization remains the same at a given cooling rate.

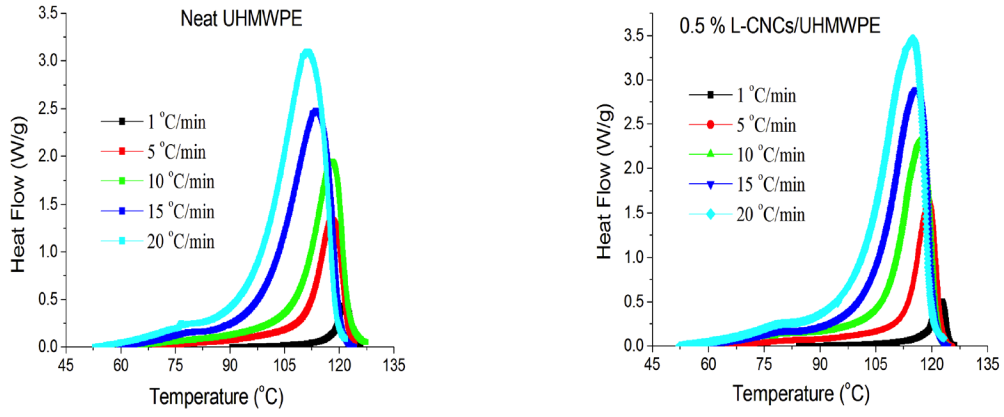

Figure 12. The heat flow of (a) neat UHMWPE and (b) L-CNCs/UHMWPE nanocomposites as a function of temperature at various cooling rates from DSC measurements.

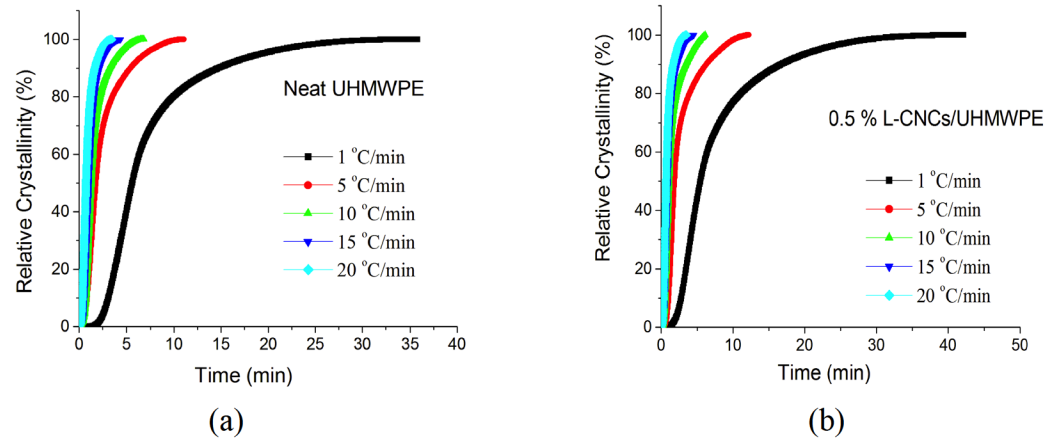

Figure 13. The degree of crystallinity of (a) neat UHMWPE and (b) L-CNCs/UHMWPE nanocomposites as a function of time at various cooling rates.

To quantitatively describe the macroscopic evolution of crystallinity during primary crystallization under quiescent isothermal conditions, classical Avrami theory was used.[128-129] The Avrami equation is as follows:

$$1 - X_t = \exp(-kt^n) \tag{3}$$

where n is the Avrami exponent and gives information about the type of crystal growth, k the Avrami rate constant and X_t is the relative degree of crystallinity at time t. The equation above is often expressed in the double logarithmic linear form, as shown in Equation 4.

$$\ln[-\ln(1 - X_t)] = \ln k + n \ln t \tag{4}$$

By plotting ln[-ln (1-X_t)] versus ln t for each cooling rate, the value of n and k can be directly obtained from the slope and intercept of the best-fitted lines, respectively. However, these parameters do not have the same significance as in the case of isothermal crystallization since the temperature changes continuously under non-isothermal conditions; it affects the rate of both nuclei formation and spherulite growth, both parameters are temperature dependent.[130] Furthermore, the non-isothermal crystallization rate was characterized using half-time of crystallization $t_{1/2}$, which is defined as the time to reach 50% of the relative degree of crystallinity and can be directly calculated using Equation 5.

$$t_{1/2} = \left(\frac{\ln 2}{k}\right)^{1/n} \tag{5}$$

The data presented in this table shows that the crystallization half-time decrease with increasing cooling rates. With the addition of L-CNCs, the crystallization half-time was comparable to that of the neat UHMWPE. This observation shows that the overall nucleation and growth parameters are in agreement with one another when the L-CNCs are incorporated into the matrix. The crystallization parameters, n, and k for L-CNCs/UHMWPE nanocomposites were obtained from the slopes and intercepts of the best-fitted lines, respectively, for the primary crystallization portion of the $\ln[-\ln(1-X_t)]$ vs. $\ln t$ plots as shown in Figure 14, and the data is summarized in Table 7. For neat UHMWPE, the values of Avrami exponents (n) were non-integral and ranged from 2.8 to 4.4 for the given cooling rates. Generally, the n value close to 3 and 4 indicate a thermal nucleation process; the nucleation process is where crystals start growing together, followed by three-dimensional spherulitic crystal growth. The fractional n value obtained for the neat polymer can be attributed to the crystal branching and three-dimensional crystal growth or mixed growth and change in the nucleation mechanism.[131] The addition of L-CNCs had little to no effect on n, k, and $t_{1/2}$ values of UHMWPE at a given cooling rate.

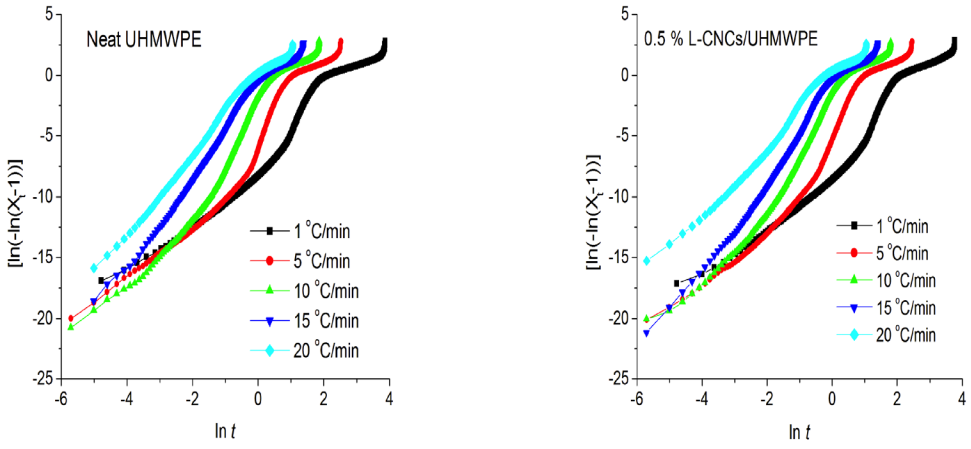

Figure 14. Plots of ln[-ln(1-X_t)] versus ln t for (a) neat UHMWPE and (b) L-CNCs/UHMWPE nanocomposites.

Table 7. Values of n, k, and $t_{1/2}$ for UHMWPE and L-CNCs/UHMWPE Nanocomposites Obtained from Avrami Analysis for Non-Isothermal Crystallization Processes.

	Cooling rate (°C/min)	neat UHMWPE	0.5% L-CNCs/ UHMWPE	1% L-CNCs/ UHMWPE	2% L-CNCs/ UHMWPE	5% L-CNCs/ UHMWPE
n	1	4.0	4.9	3.9	4.1	3.1
	5	4.4	4.2	3.5	4.4	4.3
	10	4.1	3.7	4.0	3.4	4.4
	15	3.1	3.6	3.3	3.7	3.6
	20	2.8	2.7	3.0	4.2	3.3
k/min^{-1}	1	0.0004	0.0006	0.0005	0.0003	0.0002
	5	0.013	0.020	0.036	0.011	0.012
	10	0.17	0.24	0.20	0.18	0.10
	15	0.64	0.76	0.79	0.57	0.58
	20	1.5	1.9	1.7	1.3	1.4
$t_{1/2}$/min	1	6.4	6.5	6.6	7.0	7.3
	5	2.4	2.4	2.2	2.6	2.6
	10	1.4	1.3	1.4	1.3	1.5
	15	1.0	0.98	0.96	1.1	1.1
	20	0.76	0.68	0.75	0.87	0.78

3.4 Determination of the Effective Activation Energy of Non-Isothermal Crystallization using the Isoconversional Approach

Several mathematical models have been developed to calculate activation energy for polymer crystallization using a variation of peak temperature with the given heating

or cooling rate.[132] Among them, the Kissinger's method has been widely applied in evaluating the overall activation energy by:

$$\ln\left(\frac{\beta_i}{T_{p,i}^{\ 2}}\right) = const - \frac{\Delta E}{RT_{p,i}} \tag{6}$$

where $T_{p,i}$ is the temperature of the peak maxima at different cooling rates, for experiments performed at cooling rate (β_i), R is the gas constant, and ΔE is the activation energy. However, the Kissinger method is only applicable to heating experiments, i.e., positive values of β. Vyazovkin et al. demonstrated that their advanced isoconversional method can be used to determine the effective activation energy of non-isothermal crystallization of the polymer melts. Vyazovkin[133] has demonstrated that dropping the negative sign for β is mathematically incorrect. Kissinger equation is inapplicable to the processes that occur on cooling, such as melt crystallization. Moreover, the use of this method may result in incorrect values of the activation energy. To overcome the disadvantages of Kissinger methods, other isoconversional methods have been developed to evaluate the dependence of the activation energy on crystallinity and temperature during cooling processes. The methods include the differential isoconversion method proposed by Friedman and the advanced integral isoconversion method given by Vyazovkin and Sbirrazzuoli.[133] For the present study, the differential isoconversion method developed by Vyazovkin[133] was used. In this method, the effective activation energies (E_α) are calculated for each degree of crystallinity or extent of conversion (α) using the following equation 7:

$$\left[\frac{d\ln(d\alpha/dt)}{dT^{-1}}\right]_{\alpha} = -\frac{E_{\alpha}}{R} \tag{7}$$

where dα/dt is the instantaneous crystallization rate as a function of time at a given extent of conversion (α), E_{α} is the effective activation energy at given extent of conversion, and T_{α} is the temperature related to a given extent of conversion at a given cooling rate. It is important to note that the effective activation energy was defined by Vyazovkin as the "temperature coefficient of a process rate," and may demonstrate unusual behavior in the case of multi-step processes.[134] Recently, negative values of effective activation energy that increase with increasing extent of melt conversion were reported by several authors applying the Vyazovkin method to different polymer systems, including polyethylene terephthalate (PET)/clay,[135] PET,[134] and polypropylene (PP)/silicates.[136] Vyazovkin et al. method was applied to DSC data on the crystallization of poly(ethylene terephthalate) (PET), which resulted in the increase in activation energy along with the extent of crystallization from -270 to 20 kJ/mol as shown in Figure 15. A sudden increase in the effective activation energy is attributed to a change in the crystallization mechanism.

To avoid the complex integration of Vyazovkin equations, it is better to directly apply the differential Friedman method.[124, 137] Xu et al. reported data for Vyazovkin-plots of ln[da/dt] vs. 1/T*a* for UHMWPE; at different relative degrees of crystallinity using the Friedman method as shown in Figure 16.[124] In this analysis, for a given conversion, from 0.1 to 1α, the value of effective activation energy, E_{α} is

determined from the slope of a plot of $ln(d\alpha/dt)$ versus $1/T_\alpha$. Plots of $ln(d\alpha/dt)$ versus $1/T_\alpha$ for neat UHMWPE and the nanocomposites at the given degrees of crystallinities are shown in Figure 17. As indicated in Figure 17, the lines obtained are relatively straight, thus allowing the calculation of the effective activation energy at a given extent of conversion.

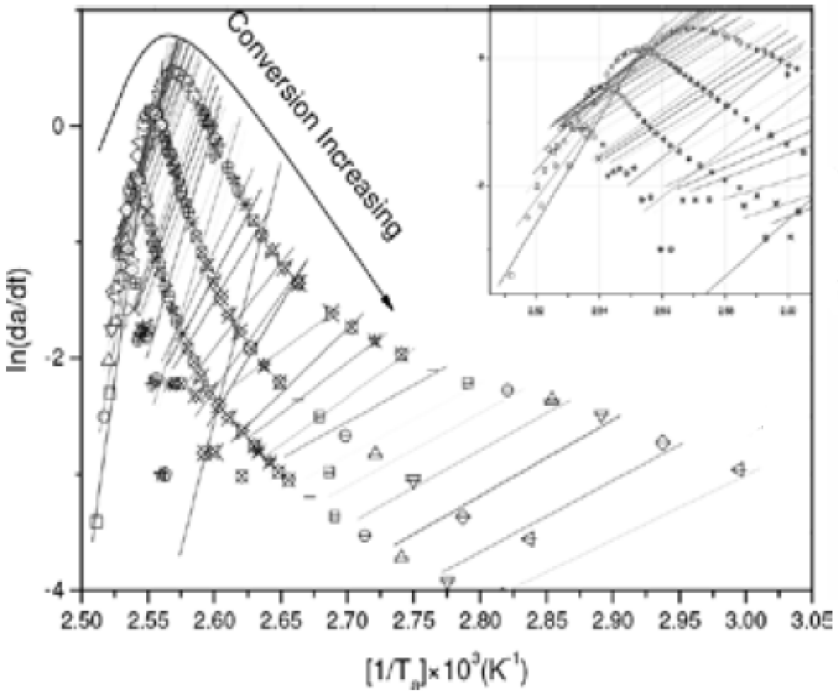

Figure 15. Vyazovkin plots of $ln(d\alpha/dt)$ versus $1/T_\alpha$ for UHMWPE at different relative degrees of crystallinity.

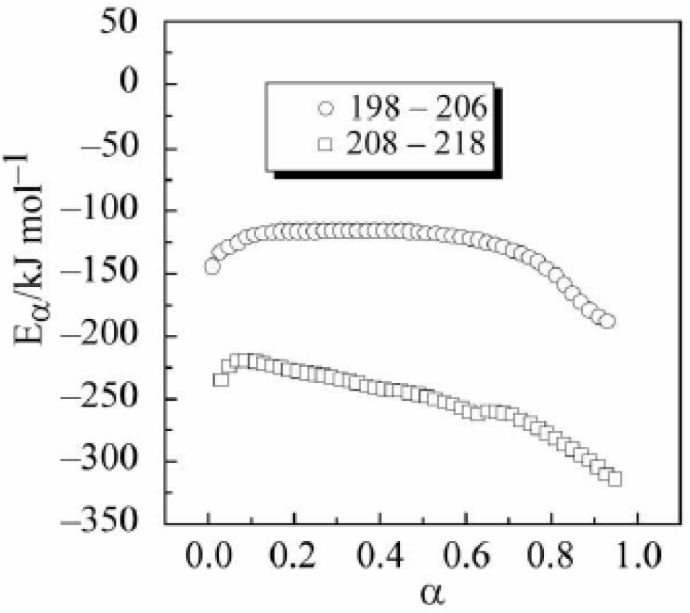

Figure 16. Dependence of the activation energy on the extent of PET conversion under isothermal conditions for two temperature regions: 198 - 206°C (circles) and 208 - 218 °C (squares).

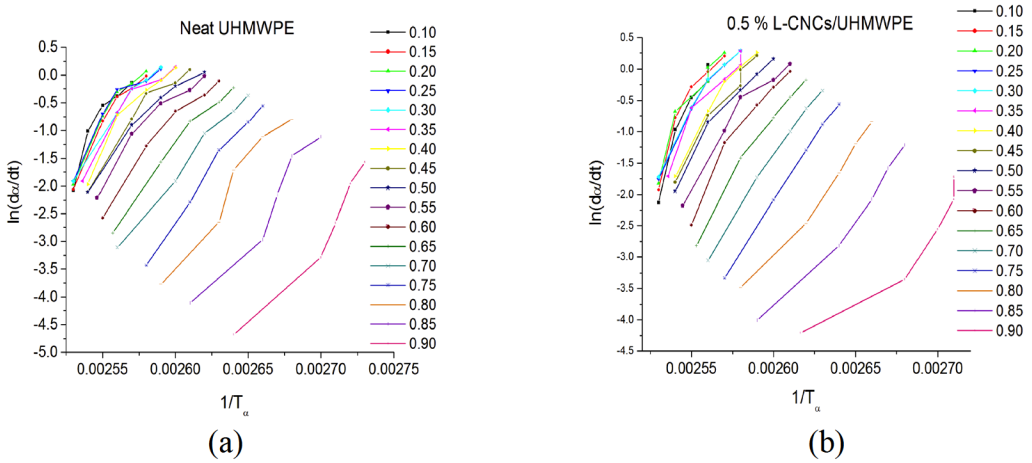

Figure 17. Vyazovkin plots of $ln(d\alpha/dt)$ versus $1/T_\alpha$ for (a) neat UHMWPE and (b) 0.5% L-CNCs/UHMWPE.

The calculated effective activation energy (E_α) plotted against the relative extent of crystallization (α) for the neat UHMWPE, and L-CNCs/UHMWPE nanocomposites, shown in Figure 18. The calculated effective activation energies are negative and become less negative with increasing extent of crystallization and decreased with an increase in crystallization temperature for both neat UHMWPE and L-CNCs/UHMWPE nanocomposites. The negative effective activation energies have been explained by a decrease in the free energy of nucleation with increasing the degree of supercooling.[133] Within the region of $T_{max} - T_m$, one encounters the anti-Arrhenius crystallization behavior that is described by negative values of the effective activation energy.[133] When $T < T_{max}$, the Arrhenius behavior is observed, which is described by positive values of the experimental activation energy.[133] The calculated E_α values for neat UHMWPE and 2% L-CNCs/UHMWPE nanocomposites increased from -275 to -100 kJ/mol, and -422 to -21 kJ/mol, respectively, with the increasing extent of crystallization from 0.01 to 0.9. The results suggest that initially, it was easier for UHMWPE chains, with or without L-CNCs, to crystallize faster. However, especially after 0.7α, it becomes rather difficult to crystallize due to the requirement of more energy to transport the UHMWPE chains to the crystallization surface with decreasing temperature and increasing conversion, as shown in Figure 18. Lower values of E_α for L-CNCs/UHMWPE nanocomposites than that of neat UHMWPE at low degrees of crystallization also indicate the nucleating behavior of L-CNCs in UHMWPE matrix.[42, 124]

The phenomenon of the negative value of activation energy obtained in this study can be understood by the equation derived by Sergey Vyazovkin and Nicolas

Sbirrazzuoli.[133] These authors developed an equation which can be applied to non-isothermal crystallization for evaluating the dependence of the effective activation energy on conversion and temperature as:

$$E_\alpha = U^* \frac{T^2}{(T - T_\infty)^2} + K_g R \frac{T_m^2 - T^2 - T_m T}{(T_m - T)^2 T} \quad (8)$$

where T_∞ is a hypothetical temperature where motion associated with viscous flow ceases, usually 30 degrees below the glass transition temperature, T_g, T_m is the equilibrium melting temperature of polymer, T is crystallization temperature, U* is the activation energy for transport of polymer chains to the crystallization site, K_g is the energy required for the formation of nuclei, and R is gas constant. The second term in Equation 8 is negative in the temperature region between ~$0.618T_m$ and T.[133] Moreover, the absolute value of this term approaches negative infinity when the temperature approaches the melt temperature, i.e., at small supercooling ($\Delta T = T_m - T$). As the supercooling increases, the melt converts to the crystalline phase, and the effective activation energy increases toward zero. Whereas, the first term of Equation 8 is always positive, and its value decreases as temperature increases. Since the crystallization of UHMWPE in the present study takes place in the temperature range between $0.618T_m$ and T, the effective activation energies are negative and increase with decreasing temperature and vice versa. Equation 8 also explains why the effective activation energy of the melt crystallization performed upon cooling yields negative values, whereas

crystallization during heating, e.g., cold crystallization in polymers, yields positive activation energy.

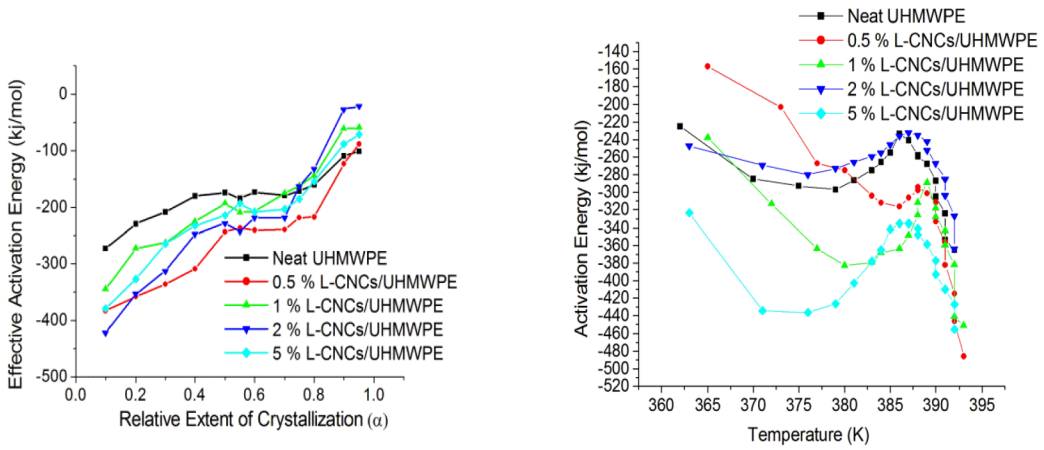

Figure 18. Dependence of the effective activation energy on the (a) relative extent of crystallization and (b) temperature.

3.5 Mechanical Properties of L-CNCs/UHMWPE Nanocomposites by Tensile Testing

In a recent study, CNC/UHMWPE composites were prepared by blending different amounts of CNCs with UHMWPE, followed by melt-pressing in a hot-press. The properties of the CNC/UHMWPE composites were also investigated by tensile testing. Wang et al. reported that an increase in CNC loading led to decreased tensile strength at break and toughness; however, Young's modulus values remained constant. This behavior is explained by poor interaction of the CNCs with UHMWPE and aggregation of the CNCs in the UHMWPE matrix. This work indicated that there is an incompatible interface between CNCs and UHMWPE.[138] Figure 19 shows typical stress-

strain curves for neat UHMWPE and the nanocomposites having varying loadings of L-CNCs, tensile test results are summarized in Table 8. All samples showed typical stress-strain behavior of UHMWPE. The results show that the incorporation of L-CNCs resulted in a significant increase in Young's modulus, indicative of good interfacial interaction between the L-CNCs and the polymer matrix. On the addition of 2 wt.% L-CNCs, Young's modulus of UHMWPE, measured as the slope in the elastic region of the stress-strain curve, increased by approximately 43%, i.e., from 416 to 595 MPa relative to neat UHMWPE. However, no significant change was observed upon the addition of L-CNCs in tensile strength at specimen break, nor the yield strength, as shown in Table 8. It is believed that at 5 wt.% L-CNC loading, tensile strength decreased relative to neat UHMWPE and UHMWPE nanocomposites due to agglomeration L-CNCs and micro-void formation at the L-CNCs and UHMWPE interface during the sintering process. The elongation to failure of the nanocomposites exhibits a slight decrease as the wt.% of L-CNCs increased, indicating that the nanocomposites exhibited less elasticity as compared to neat UHMWPE. However, our experimental results showed that the lignin of the L-CNCs improved the interfacial interactions between the CNCs and UHMWPE polymer matrix due to an increase in Young's modulus values.

In an effort to quantify the effects of the addition of L-CNCs to UHMWPE on the ability of the nanocomposites to dissipate energy, the tensile toughness, U_T of the nanocomposites was calculated using Equation 9 by integrating the stress-strain curves as:[139]

$$U_T = \int_0^{\varepsilon_f} \sigma \cdot d\varepsilon \tag{9}$$

where ε is the strain, σ is the stress, and ε_f is the strain at specimen failure.[139] The data in Table 8 shows no improvement in tensile toughness values upon the addition of the L-CNCs in UHMWPE. Tensile toughness is defined as the amount of energy per unit volume that a material can absorb before breaking.[139] Our results show that at a higher loading of L-CNCs, at 5 wt.%, the tensile toughness is reduced. This is attributed to the agglomeration of L-CNCs and poor interfacial adhesion between L-CNCs and the polymer matrix, resulting in reduced energy dissipation.

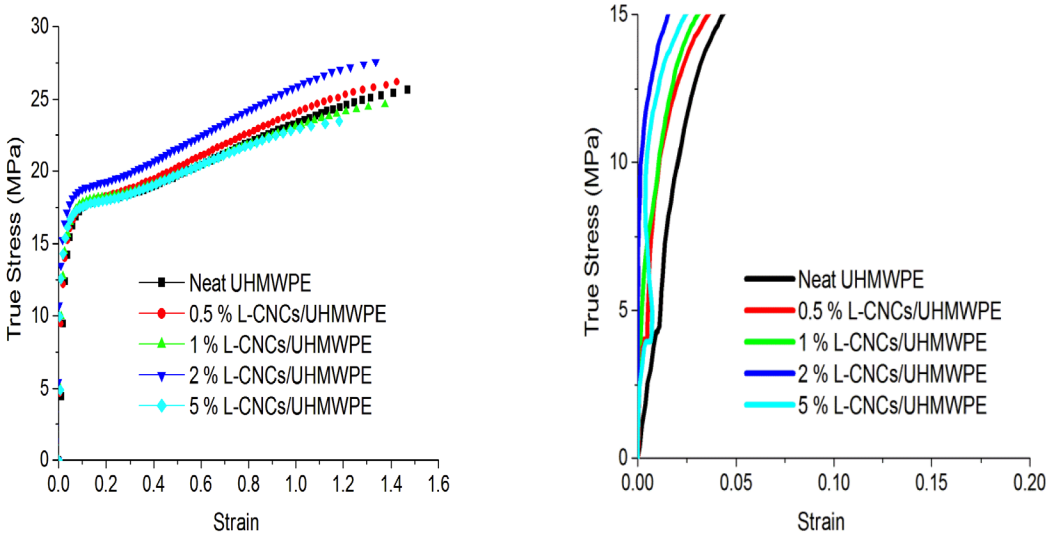

Figure 19. Representative true stress versus engineering strain curves for neat UHMWPE and L-CNCs/UHMWPE nanocomposites (a) Full scale, and (b) Zoomed-in scale.

Table 8. Results Obtained from Stress-Strain Curves of Neat UHMWPE and L-CNCs/UHMWPE Nanocomposites.

Sample Designation	Young's Modulus (MPa)	Tensile Strength at Break (MPa)	Yield Strength (MPa)	Tensile Toughness (MPa)
neat UHMWPE	416.4 ±33	39.1 ±2	13.7 ±1	18.1 ±1
0.5% L-CNCs/UHMWPE	457.6 ±28	39.3 ±1	14.4 ±1	18.3 ±1
1% L-CNCs/UHMWPE	507.3 ±63	38.5 ±1	15.1 ±1	17.6 ±0
2% L-CNCs/UHMWPE	595.4 ±58	38.7 ±1	15.9 ±1	17.8 ±0
5% L-CNCs/UHMWPE	572.6 ±60	35.0 ±2	15.4 ±1	17.2 ±0

Due to the good dispersion of L-CNCs in UHMWPE, it is expected that some improvement in the tensile strength would result. However, the addition of up to 2 wt.% L-CNCs led to neither a decreased or an increased tensile strength. Poor outcomes have been reported in the literature for the mechanical properties of CNCs/UHMWPE nanocomposites.[138] Wang et al. reported the addition of 2 - 8 wt.% of CNCs to UHMWPE led to a decrease in tensile strength, and elongation at break due to the weak interface between hydrophilic CNCs and hydrophobic UHMWPE.[138] Our results show that the coating of lignin on the surface of CNCs is an effective approach to improve the dispersion of CNCs in hydrophobic polymers such as UHMWPE.

Experimental results of UHMWPE nanocomposites were compared to the values calculated from an empirical model to predict the effect of L-CNCs on the mechanical properties of the UHMWPE. The modified Halpin–Tsai equation was used to predict the modulus of L-CNCs/UHMWPE nanocomposites based on the mechanical properties of

the nanocomposites. Considering the random orientation of L-CNCs in the UHMWPE matrix, we can calculate the modulus of composite with the modified Halpin–Tsai equation.[140]

$$Ec = \left[\left(\frac{3}{8}\right)\left(\frac{1+2\left(l_{L-CNC}/d_{L-CNC}\right)\eta_L V_{CNC}}{1-\eta_L V_{L-CNC}}\right)+\left(\frac{5}{8}\right)\left(\frac{1+2\eta_T V_{L-CNC}}{1-\eta_T V_{L-CNC}}\right)\right]E_{PE} \quad (10)$$

$$\eta_L = \frac{\left(E_{L-CNC}/E_{PE}\right)-1}{\left(E_{L-CNC}/E_{PE}\right)+2\left(l_{L-CNC}/d_{L-CNC}\right)}, \quad \eta_T = \frac{\left(E_{L-CNC}/E_{PE}\right)-1}{\left(E_{L-CNC}/E_{PE}\right)+2}$$

Where, and E_C, $E_{PE,}$ and $E_{L\text{-}CNC}$ are the moduli of the nanocomposites, UHMWPE, and L-CNCs, respectively; $l_{L\text{-}CNC}/d_{L\text{-}CNC}$ is the ratio of the length to the diameter, i.e., the aspect ratio for the L-CNCs, and $V_{L\text{-}CNC}$ is the volume fraction of L-CNCs in the nanocomposites. The weight fraction of L-CNCs and UHMWPE was converted to the volume fraction using the densities of UHMWPE (0.945 g/cm^3) and L-CNCs (1.5 g/cm^3).[7, 115] To calculate the theoretical values of nanocomposite modulus, the aspect ratio of ~16 and $E_{L\text{-}CNC}$ of ~115 GPa for L-CNCs was used.[8, 141] The L-CNC modulus used in this study represents an average modulus in the axial direction.[8] Experimental and calculated values of Young's modulus of L-CNCs/UHMWPE nanocomposites as a function of L-CNC are shown in Figure 20. The experimental results for the L-CNCs/UHMWPE nanocomposites are in good agreement with theoretically predicted values up to 2 wt.% L-CNCs. Further addition of L-CNCs gave a reduction in the modulus, believed to be due to the agglomeration of L-CNCs at the higher loading.[90, 138]

The Halpin-Tsai model results are evidence of good dispersion and distribution of L-CNCs in UHMWPE up to 2 wt.% loading of L-CNCs.

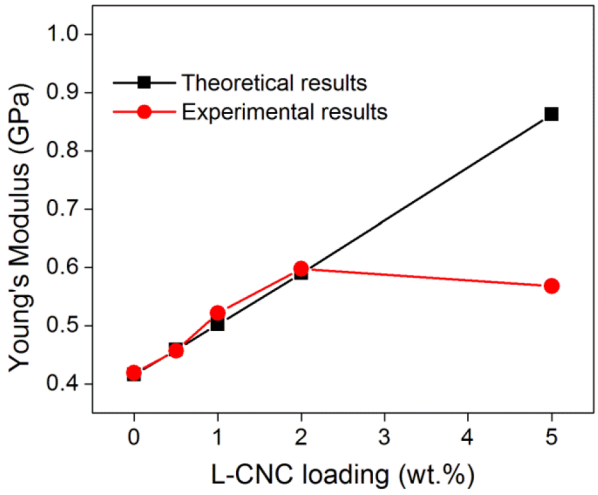

Figure 20. Experimental and calculated values of Young's modulus of L-CNCs/UHMWPE nanocomposites as a function of L-CNC loading.

3.6 Viscoelastic Properties of UHMWPE Nanocomposites by Dynamic Mechanical Analysis (DMA)

The viscoelastic properties of UHMWPE nanocomposites were determined by DMA. The traditional testing of ballistic protection systems with the use of live ammunition requires a suitable firing range as well as additional measuring equipment.[142] Due to the high costs of such testing development, DMA is a reliable and cost-effective method of determining the mechanical properties of UHMWPE nanocomposites. In this study, DMA was used to investigate the stiffness and energy absorption at various frequencies. The DMA technique applies an oscillating force to a material sample and examines the material's response to that force.[142] The modulus measured using DMA is a

complex modulus, which is comprised of an elastic modulus, E′, and loss modulus, E″. These moduli components provide a much more comprehensive material characterization than tensile testing by comparing the material's ability to return energy to its ability to lose energy.[142] The ratio of E″/E′ is called tan δ, where δ is the phase lag between the applied force and the response of the material to that force. The tan δ peaks are highly sensitive to transitions in the material.[142]

DMA was carried out in the linear viscoelastic range and used to measure the thermomechanical properties of neat UHMWPE and L-CNCs/UHMWPE nanocomposites under cyclic loading at a heating rate of 2 °C/min over a range of temperatures and frequencies. According to the literature, UHMWPE exhibits three relaxation processes, named α, β, γ relaxations, in order of decreasing temperature by DMA as shown in Figure 21.[143-144] The α-relaxation transition is related to the main chain motions and is observed above the glass transition temperature. In addition, its intensity is increased by increasing the degree of crystallinity. The β-relaxation transition is associated with the movement of side chains or branches and is related to the amorphous regions. This transition is very weak in UHMWPE. The γ-relaxation transition is related to the local intermolecular relaxation at a temperature in the region of T_g. It characterizes movements of the crystalline phase induced by an interlamellae shear and intralamellar shear mechanisms.[143] Figure 22 shows loss modulus values, E'', against temperature, at 1 Hz plots for neat UHMWPE and L-CNCs/UHMWPE nanocomposites. Neat UHMWPE and UHMWPE nanocomposites show two prominent peaks in Figure 22, which correspond to the γ- and α-transition regions. The addition of up to 2 wt.% L-

CNCs to UHMWPE led to lower loss modulus values as compared to neat UHMWPE, which is an indication of the nanocomposites becoming more elastic, and less energy being dissipated during mechanical cyclic loading. This result is due to the presence of L-CNCs in the UHMWPE matrix, which restrains UHMWPE chain segment movements through filler-matrix and filler-filler interfacial interactions.[122] Plots of E″ against temperature for neat UHMWPE and 0.5% L-CNCs/UHMWPE nanocomposites at 0.1, 1, 10, and 50 Hz are shown in Figure 23. The nanocomposites exhibited weaker β transition peaks than neat UHMWPE. In the L-CNCs/UHMWPE nanocomposites, the energy dissipation may also come from the L-CNC-matrix interface where friction between the two phases can occur. In the temperature range of 30 to 130 °C, the elastic modulus, E′, values of neat UHMWPE and the L-CNCs/UHMWPE nanocomposites shown in Figure 24 decreases with an increase in temperature at 1 Hz, which may be attributed to easier thermal motion of the segments of the polymer chains due to the increase in temperature. In Figure 25, the E′ values of the neat UHMWPE and nanocomposites decrease with an increase in temperature for all frequencies measured. The higher the frequency, the shorter the time will be, resulting in a short time for the polymer molecule chains to relax. The elastic modulus values for 2 and 5 wt.% nanocomposites were higher than those of UHMWPE and other nanocomposite systems which may be due to enhanced mechanical restraints imposed by increased loading of the L-CNCs particles on the molecular mobility of UHMWPE chains.[145]

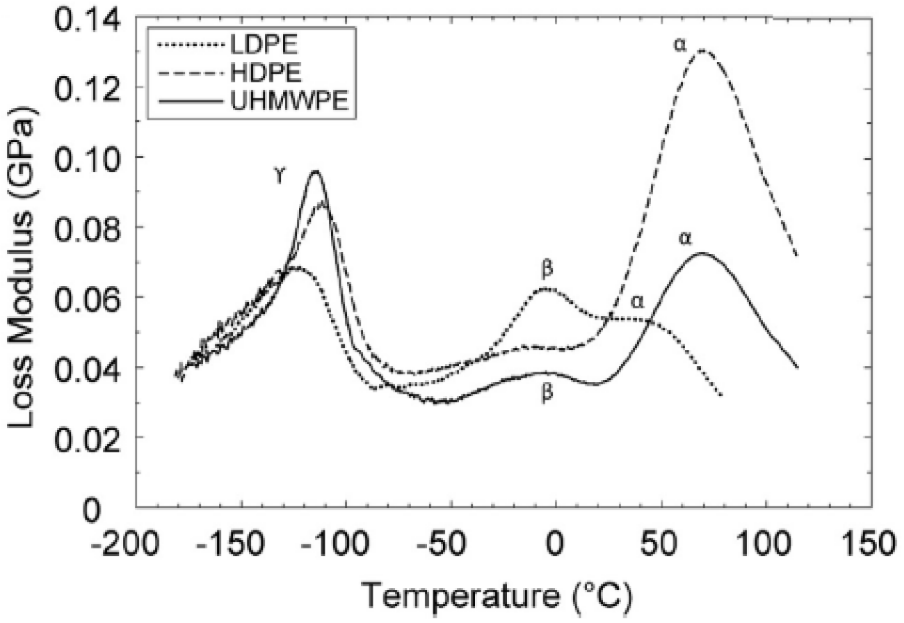

Figure 21. The literature of DMA loss modulus results for LDPE, HDPE, and UHMWPE: temperature scan at a beam bending frequency of 1 Hz.

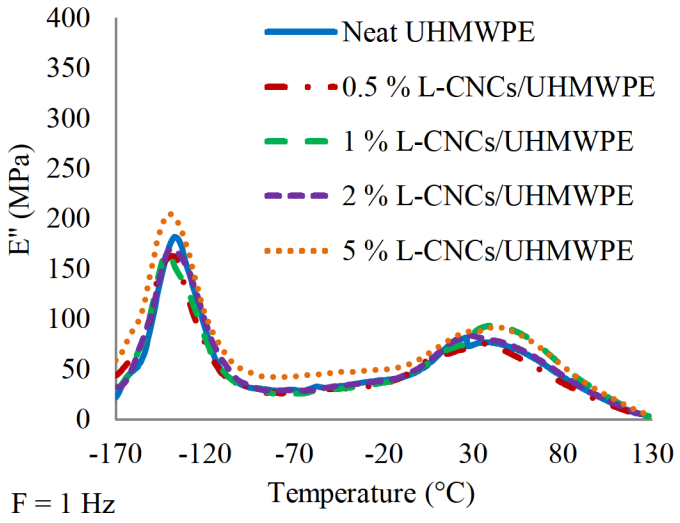

Figure 22. DMA scans of neat UHMWPE and L-CNCs/UHMWPE nanocomposites at a heating rate of 2 °C/min showing the loss modulus (E″) against temperature at 1 Hz.

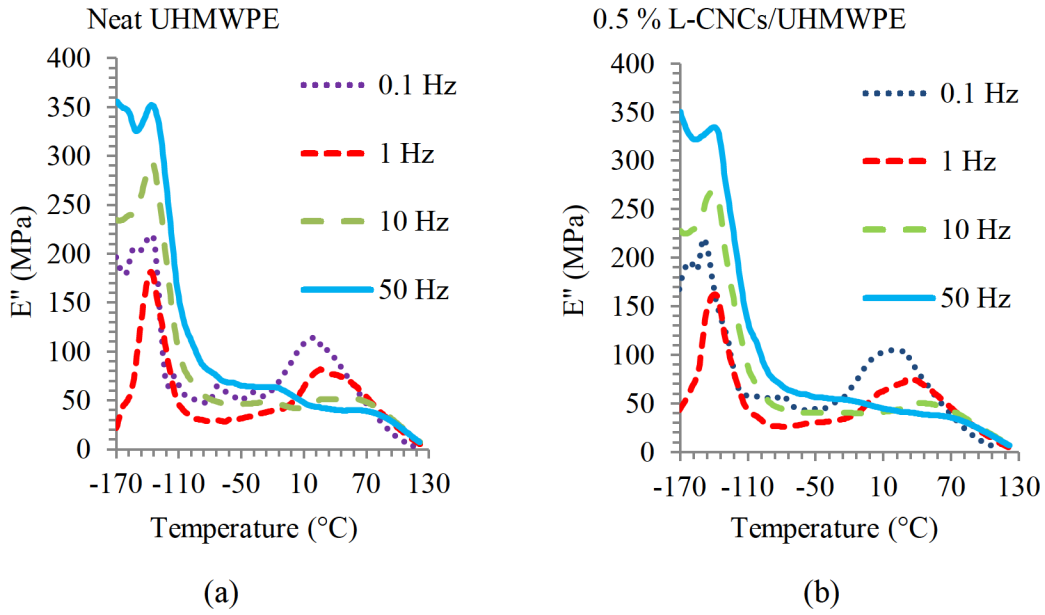

Figure 23. DMA scans of (a) neat UHMWPE and (b) 0.5% L-CNCs/UHMWPE nanocomposite at a heating rate of 2 °C/min showing the loss modulus (E″) against temperature for 0.1, 1, 10, and 50 Hz.

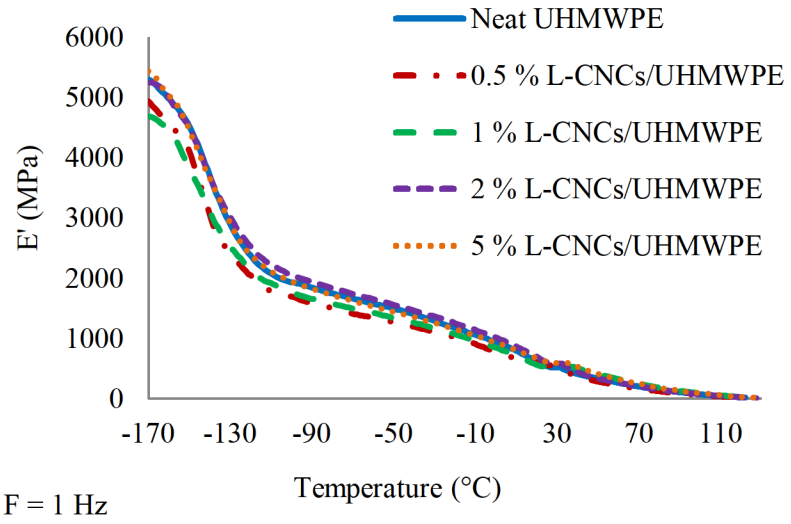

Figure 24. DMA scans of neat UHMWPE and L-CNCs/UHMWPE nanocomposites at a heating rate of 2 °C/min showing the elastic modulus (E′) against temperature at 1 Hz.

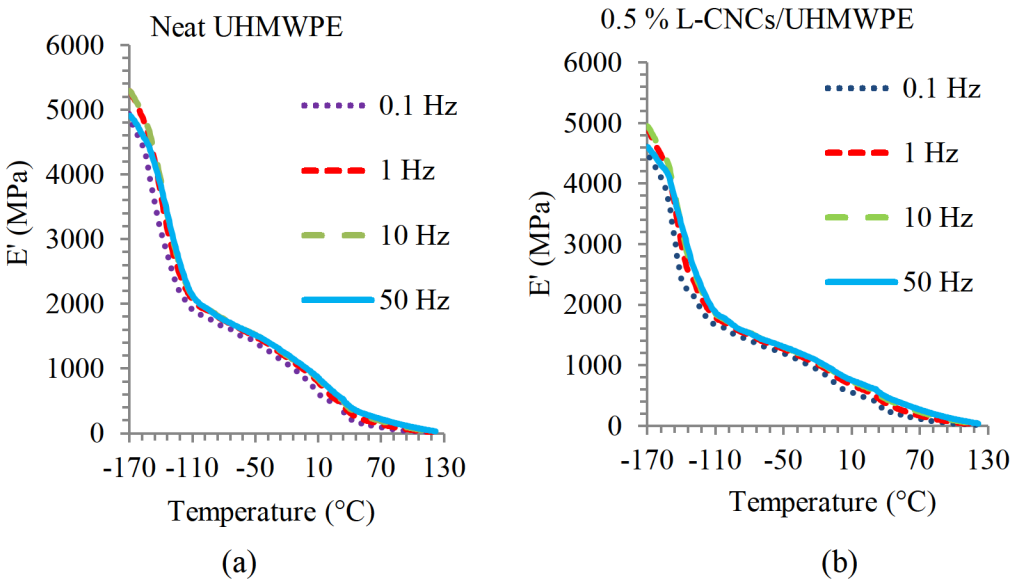

Figure 25. DMA scans of (a) neat UHMWPE and (b) 0.5% L-CNCs/UHMWPE nanocomposite at a heating rate of 2 °C/min showing the elastic modulus (E′) against temperature at 0.1, 1, 10, and 50 Hz.

Figure 26 shows the variation of damping parameter, tan δ, as a function of temperature for neat UHMWPE and 0.5% L-CNCs/UHMWPE nanocomposite at 1 Hz. Two main relaxation processes were observed at increasing temperature, namely a γ-transition and α-transition in DMA. The γ-relaxation occurring around -130 °C is associated with the glass transition, T_g, of the amorphous phase. We observe an influence of the L-CNCs on the α-relaxation phase of UHMWPE due to increasing L-CNC loading; the intensity of the peaks for all nanocomposites is slightly increased as compared to neat UHMWPE. Concerning the α-relaxation, it characterizes movements of the crystalline phase induced by interlamellar shear mechanisms.[81, 146] Figure 27 shows the variation of the damping parameter, tan δ as a function of temperature for neat UHMWPE and L-CNCs/UHMWPE nanocomposites at 0.1, 1, 10, and 50 Hz. The tan δ

plot shows that neat UHMWPE and L-CNCs/UHMWPE nanocomposites go through an γ- and α-transition peaking around -150 °C and 60-100 °C, respectively, for given frequencies. These transitions are due to sufficient energy for motions of a few atoms along the main chain or of side groups on the main chain of the polymer.[142] As frequency increases, the molecular relaxations occur at high temperatures, and as a consequence, the T_g increases with increasing frequency. It can also be seen that an increase in frequency leads to a rise in the α-relaxation temperature. Our results show that during the dynamic damping mechanism, at a given L-CNC loading, UHMWPE nanocomposites absorbed more energy than neat UHMWPE at high strain rates. This provides merit when using UHMWPE as an absorbent material for bullet-proof vests.

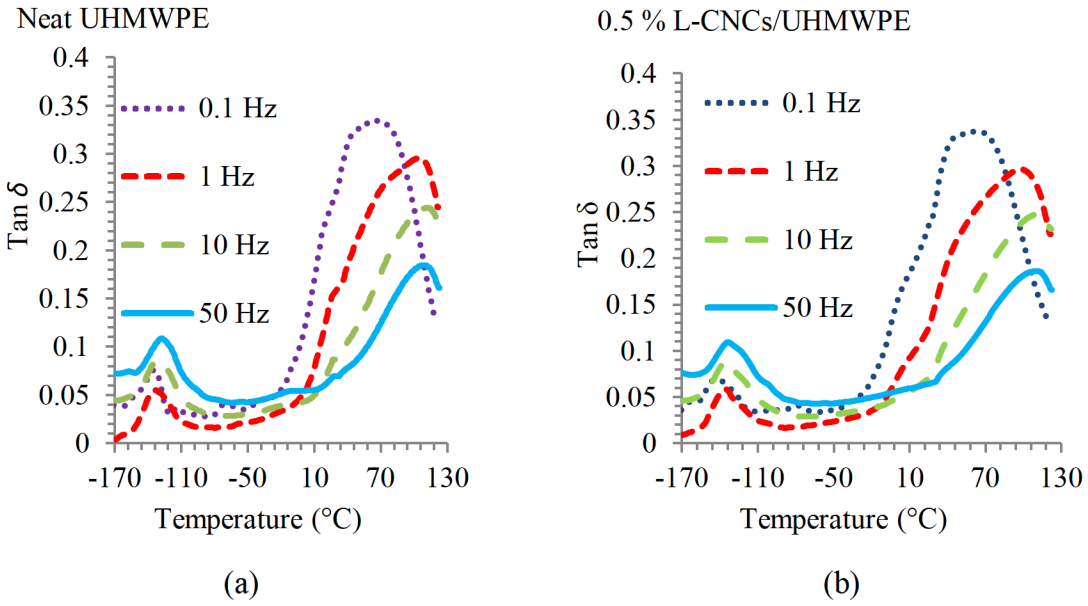

Figure 26. Show the temperature dependence of the loss factor (tan δ) for (a) neat UHMWPE and (b) 0.5% L-CNCs/UHMWPE nanocomposite at 0.1, 1, 10, and 50 Hz at a heating rate of 2 °C/min.

The β-relaxations seen in Figure 27a are due to movements of loops or amorphous chain segments in the interfacial regions.[116] Other authors have attributed this relaxation to changes in the amorphous regions of polyethylene due to branching, ordering of amorphous chains, crosslinks, or tie-molecules.[147] Figure 27b, c, and d show that the intensity of the β-relaxation decreases for 1, 10, and 50 Hz. We consider that the disappearances of β-relaxations at low-frequency levels indicate a disappearance of chain mobility that was localized in the interfacial region.[122] It appears that the addition of L-CNCs has actually increased the mobility of the amorphous phase in the UHMWPE, and hence it increased the damping of the nanocomposite.[148]

The γ- and α-relaxation of UHMWPE was analyzed by means of the Arrhenius approach to determine the activation energy from plots shown in Figure 27. Figure 28 show the log (frequency) as a function of the inverse of temperature, K, for neat UHMWPE and L-CNCs/UHMWPE nanocomposites. These plots were used to calculate the activation energy for the γ- and α-transition. The Arrhenius data for γ- and α-relaxation are summarized in Table 9. The slope of each line is equal to $-E_a/R$, where E_a is the activation energy of α-relaxation, and R = 8.314 J/mol·K is the gas constant. With increasing L-CNC loading, the activation energy increased from 47.0 to 58.1 kJ/mol, and 176.8 to 431.1 kJ/mol, respectively, for the γ- and α-transition. The addition of L-CNCs increased the activation energies for the γ- and α-transition due to impaired chain mobility in UHMWPE.[149] These results may contribute to the performance improvement of UHMWPE soft-body armor.

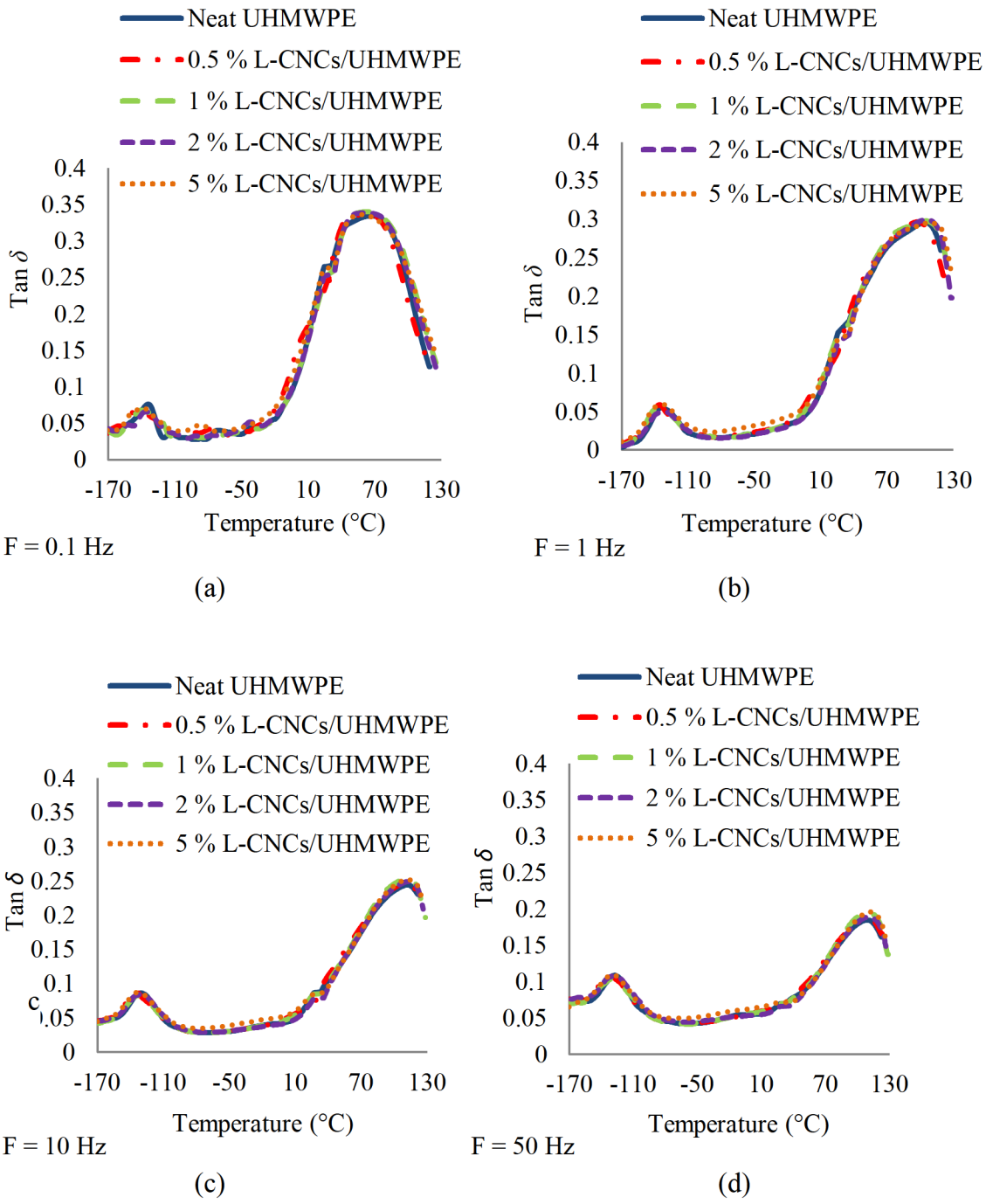

Figure 27. Shows the temperature dependence of the loss factor (tan δ) for neat UHMWPE and L-CNCs/UHMWPE nanocomposites at a heating rate of 2 °C/min at (a) 0.1 Hz (b) 1 Hz (c) 10 Hz and (d) 50 Hz.

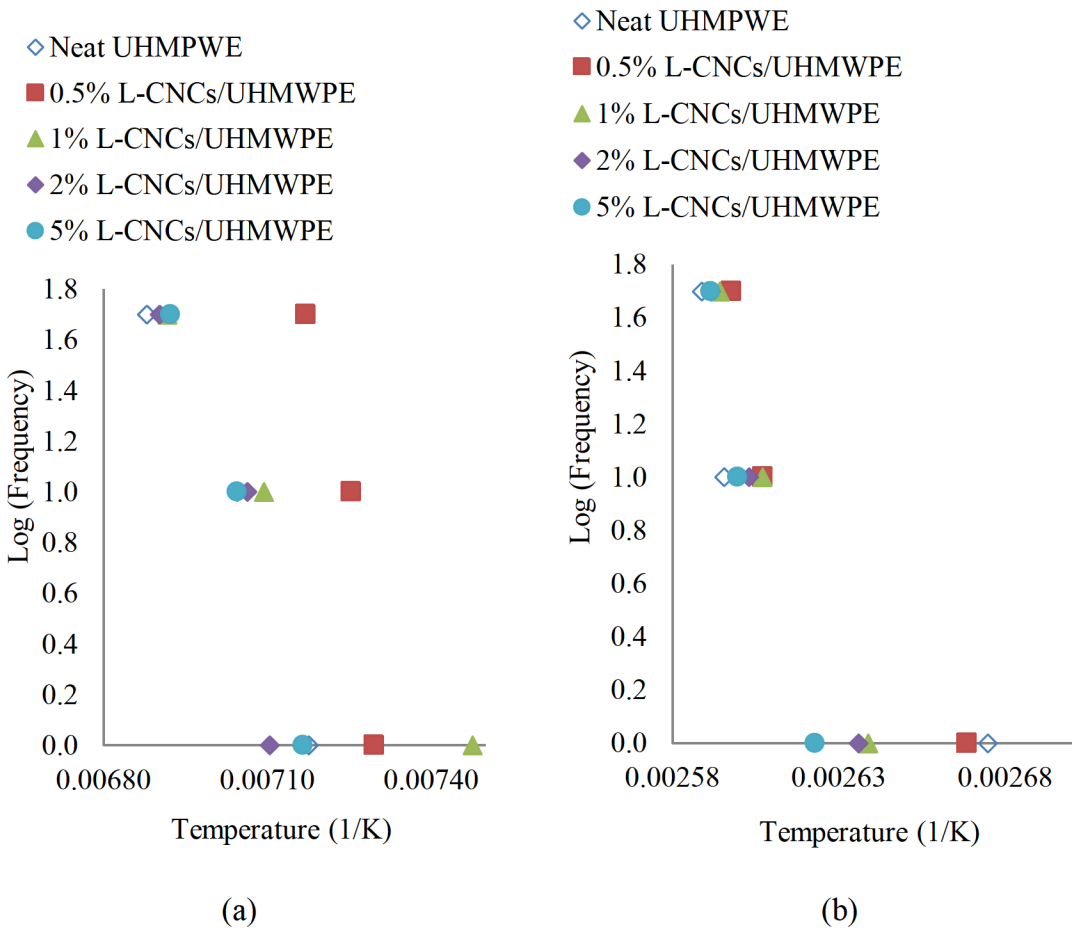

Figure 28. Arrhenius plot: temperatures of (a) γ-relaxation and (b) α-relaxation.

Table 9. Activation Energies and Glass Transition Temperature (T_g) of Neat UHMWPE and L-CNCs/UHMWPE Nanocomposites Derived from DMA Scans.

Sample designation	Temperature (°C)	Activation Energy (kJ/mol)	
	T_g (1 Hz)	ϒ-relaxation	α-relaxation
neat UHMWPE	134.1	47.2	139.6
0.5 % L-CNCs/UHMWPE	136.1	47.0	176.8
1 % L-CNCs/UHMWPE	139.4	52.4	307.1
2 % L-CNCs/UHMWPE	132.4	60.5	303.5
5 % L-CNCs/UHMWPE	133.6	58.1	431.1

3.7 Thermal Degradation Behavior of L-CNCs/UHMWPE Nanocomposites by TGA

The thermal degradation of neat UHMWPE, and UHMWPE nanocomposites, was examined under N_2 atmosphere using TGA at a heating rate of 20 °C/min. The weight loss versus temperature for neat UHMWPE and L-CNCs/UHMWPE nanocomposites are shown in Figure 29. TGA was used to determine the onset of thermal decomposition and the derivative (DTG) of percent weight loss as a function of temperature. The temperature of the maximum rate of weight loss was analyzed from the TGA thermograms and tabulated in Table 10. TGA thermograms of neat UHMWPE and UHMWPE nanocomposites indicate a one stage thermal degradation process. The thermal degradation of neat UHMWPE occurred in the temperature range 491 to 509 °C. The decomposition temperature of the nanocomposites started at 483 °C and took place up to 509 °C. It was found that the L-CNCs/UHMWPE nanocomposites degrade slightly faster than the neat UHMWPE. The onset degradation of L-CNCs/UHMWPE nanocomposites is slightly lower than that of neat UHMWPE. This can be attributed to the presence of L-CNCs, which have lower thermal stability than UHMWPE.[41]

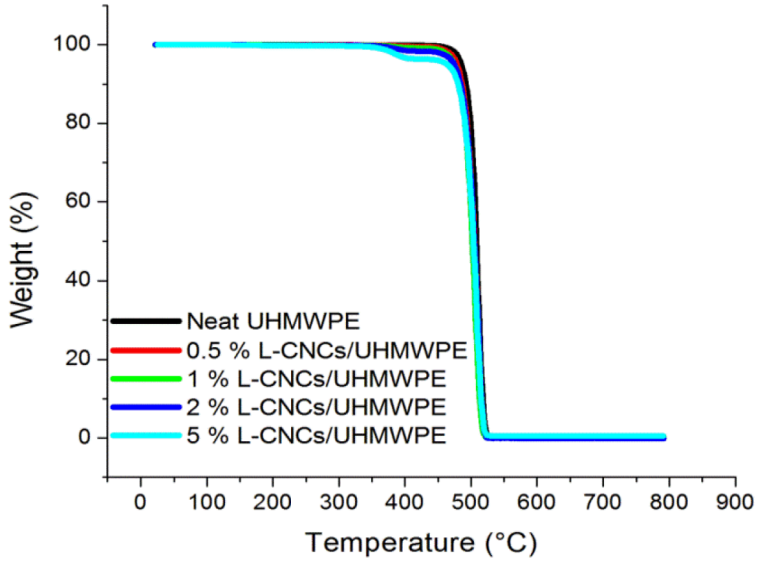

Figure 29. TGA thermograms of neat UHMWPE and L-CNCs/UHMWPE nanocomposites heated at 20 °C /min under N_2.

Table 10. Neat UHMWPE and L-CNCs/UHMWPE Nanocomposites Onset of Thermal Decomposition (T_d) and Maximum Decomposition (*DTG*).

Sample Designation	T_d onset (°C)	DTG (°C)
neat UHMWPE	497.5	509.6
0.5% L-CNCs/UHMWPE	489.5	509.3
1% L-CNCs/UHMWPE	487.4	506.7
2% L-CNCs/UHMWPE	488.9	509.9
5% L-CNCs/UHMWPE	483.7	507.7

3.8 Morphology Properties of L-CNCs/UHMWPE Nanocomposites

Scanning electron microscopy (SEM) was used to determine the morphology of L-CNC distribution in UHMWPE. Neat UHMWPE consists of spheroidal structures (0.3-2 μm) joined to each other by fibrils few tens of nanometers thin.[150] The L-CNCs have a reported average length and diameter of ~350 nm and ~5-7 nm;[39] however, the fibrils in 0.5% L-CNCs/UHMWPE have a measured average diameter of ~226 nm. Figure 30 shows the SEM images of the L-CNCs/UHMWPE nanocomposites. The SEM images of L-CNCs/UHMWPE nanocomposites show filaments in a mesh structure, which could be due to the interaction between L-CNCs and the UHMWPE matrix, also known as crazing.[122] It is the formation of fibrils connecting two layers of the undeformed polymer, which will elongate and fail under a load, leading to the formation of a crack. Crazes work as load-bearing structures deferring break in the composite; it contributes significantly to the tensile strength at break of a polymer.[122]

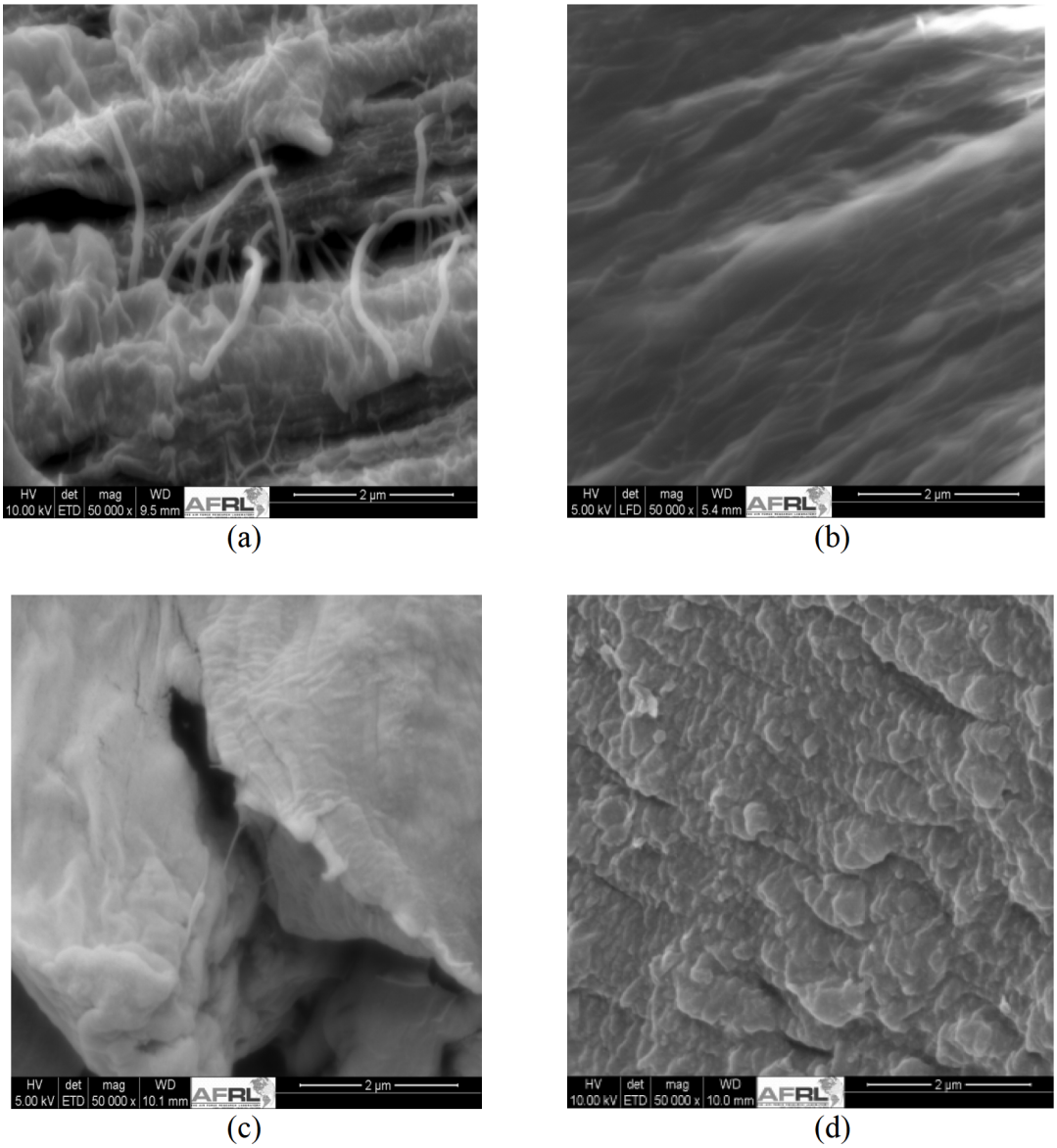

Figure 30. SEM micrograph of tensile fracture surface of (a) 0.5% L-CNCs/UHMWPE, (b) 1% L-CNCs/UHMWPE, (c) 2% L-CNCs/UHMWPE and (d) 5% L-CNCs/UHMWPE nanocomposites.

3.9 Crystallization Behavior of L-CNFs/UHMWPE Nanocomposites by DSC

UHMWPE samples were designated as 0.5% L-CNFs/UHMWPE, 1% L-CNFs/UHMWPE, and 2% L-CNFs/UHMWPE, respectively, for UHMWPE containing 0.5, 1, and 2 wt.% L-CNFs, as shown in Figure 31. Figure 32 presents the DSC scans of neat UHMWPE and L-CNFs/UHMWPE nanocomposites at a heating rate of 10 °C/min. The melt temperature, crystallization temperature, heat of fusion, and degree of crystallinity of neat UHMWPE and L-CNCs/UHMWPE nanocomposites are listed in Table 11. The melt temperature and percent crystallinity decreased for nanocomposites due to the incorporation of L-CNFs. As mentioned, the decrease in percent crystallinity is due to the confinement effects of L-CNFs, which hinders folding at the crystal growth front and chain diffusion, resulting in thin spherulite lamellar thickness.[121-122] The strong interactions between UHMWPE and L-CNFs also thermodynamically contribute to the melting point depression of UHMWPE.[122]

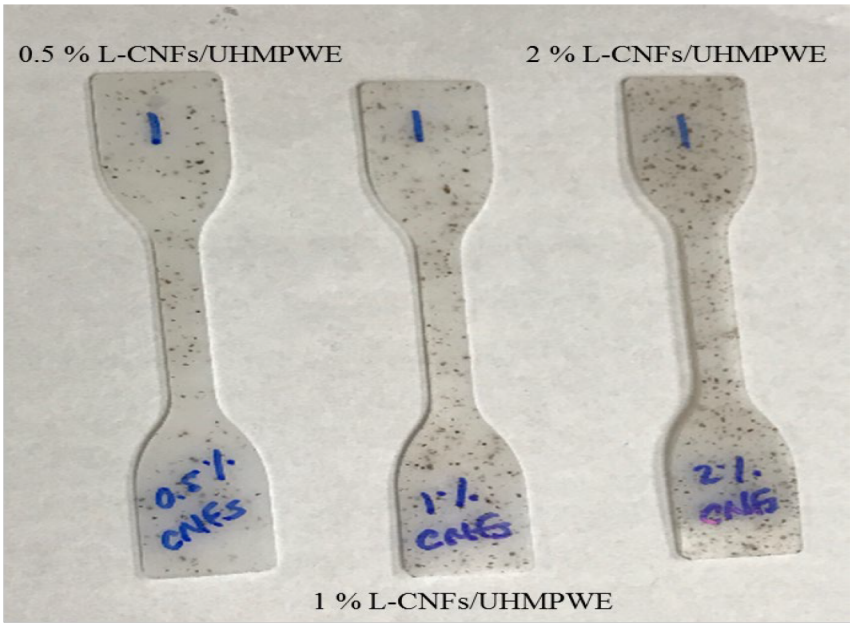

Figure 31. UHMWPE samples were designated as 0.5% L-CNFs/UHMWPE, 1% L-CNFs/UHMWPE, and 2% L-CNFs/UHMWPE, respectively for UHMWPE containing 0.5, 1, and 2 wt.% L-CNFs.

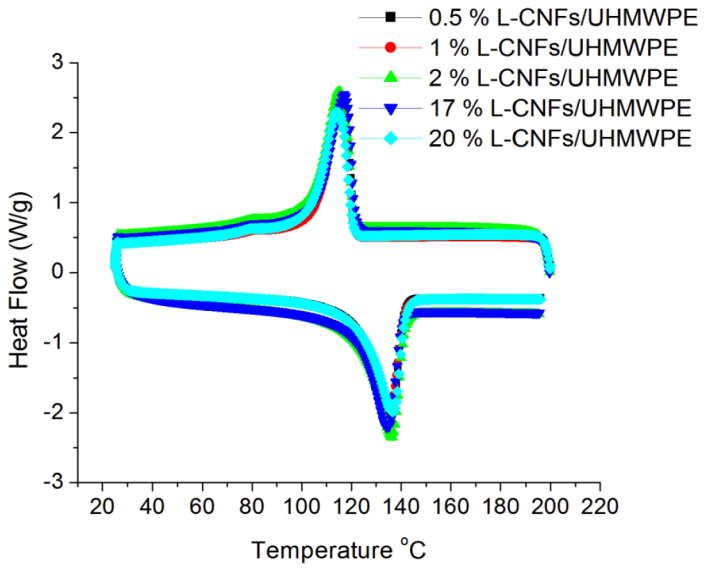

Figure 32. DSC scans for L-CNFs/UHMWPE nanocomposites at 10 °C/min.

Table 11. Thermal Properties of Neat UHMWPE and L-CNFs/UHMWPE Nanocomposites Obtained by DSC.

Sample designation	X_c (%)	T_m (°C)	T_c (°C)	ΔH_m (J/g)
neat UHMWPE	69.5	135.0	123.6	200.3
0.5% L-CNFs-UHMWPE	55.4	123.4	121.2	158.8
1% L-CNFs-UHMWPE	53.2	122.4	121.0	151.7
2% L-CNFs-UHMWPE	63.6	122.4	120.9	179.6
17% L-CNFs-UHMWPE	66.8	122.2	121.3	159.8
20% L-CNFs-UHMWPE	68.8	122.6	120.3	158.7

3.10 Thermal Degradation Behavior of L-CNFs/UHMWPE Nanocomposites by TGA

TGA studies were conducted to determine the effect of L-CNFs loading on UHMWPE, as to determine the onset of thermal decomposition and the derivative (DTG) of percent weight loss as a function of temperature. Figure 33 shows the TGA thermogram of neat UHMWPE and L-CNFs/UHMWPE nanocomposites. The onset of thermal decomposition and temperature of the maximum rate of weight loss was analyzed from the TGA thermograms and tabulated in Table 12. All the samples display a single step mass loss corresponding to the degradation of the polyethylene backbone. The neat UHMWPE plot shows an abrupt linear mass loss started at 491.1 °C. All L-CNFs/UHMWPE nanocomposites had a 5% increase or more for the onset of decomposition temperature as compared to neat UHMWPE. The high thermal stability of the nanocomposites as compared to the neat UHMWPE is attributed to the

incorporation of L-CNFs.[41] Marshall et al. reported API L-CNFs were more thermally stable than API L-CNCs and CNCs.[41, 151]

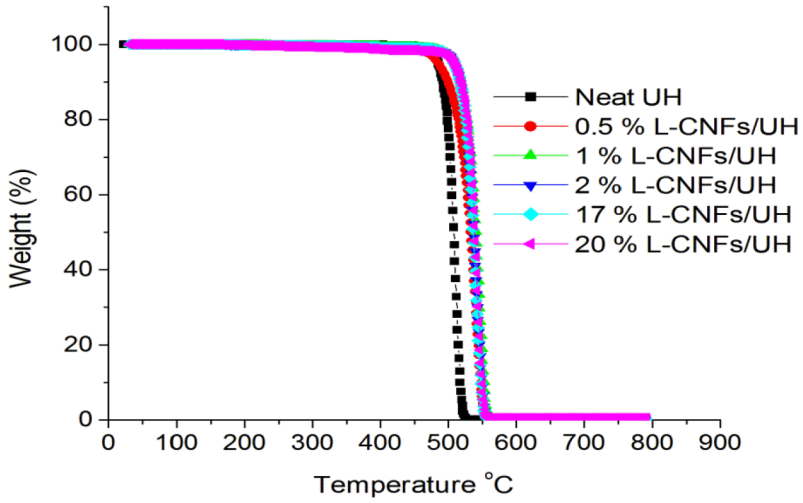

Figure 33. TGA plots of neat UHMWPE and L-CNFs/UHMWPE nanocomposites heated at 20 °C /min under N_2.

Table 12. Neat UHMWPE and L-CNCs/UHMWPE Nanocomposites Onset of Thermal Decomposition (T_d) and Maximum Decomposition (*DTG*).

Sample Designation	T_d onset (°C)	DTG (°C)
neat UHMWPE	497.5	509.6
0.5% L-CNFs/UHMWPE	523.7	539.9
1% L-CNFs/UHMWPE	522.4	541.2
2% L-CNFs/UHMWPE	526.8	542.5
17% L-CNFs/UHMWPE	526.7	539.5
20% L-CNCs/UHMWPE	532.7	536.7

3.11 Mechanical Properties of L-CNFs/UHMWPE Nanocomposites by Tensile Testing

Figure 34 shows representative stress-strain curves for neat UHMWPE and UHMWPE nanocomposites having varying wt.% of L-CNFs. From the stress-strain curves, all samples show typical stress-strain behavior of UHMWPE. The results indicate that the incorporation of L-CNFs resulted in significant improvement in Young's modulus while exhibiting no improvement in tensile strength. On the addition of 1 wt.% of L-CNFs, Young's modulus of UHMWPE, measured as the slope in the elastic region of the stress-strain curve, increased by approximately 22%, i.e., from 416 to 508 MPa, as shown in Table 13. The increase in Young's modulus is due to the L-CNFs acting as a reinforcing agent in UHMWPE.[122] The incorporation of L-CNFs into the UHMWPE matrix further increased entanglement points, which also resulted in a decrease in percent crystallinity.

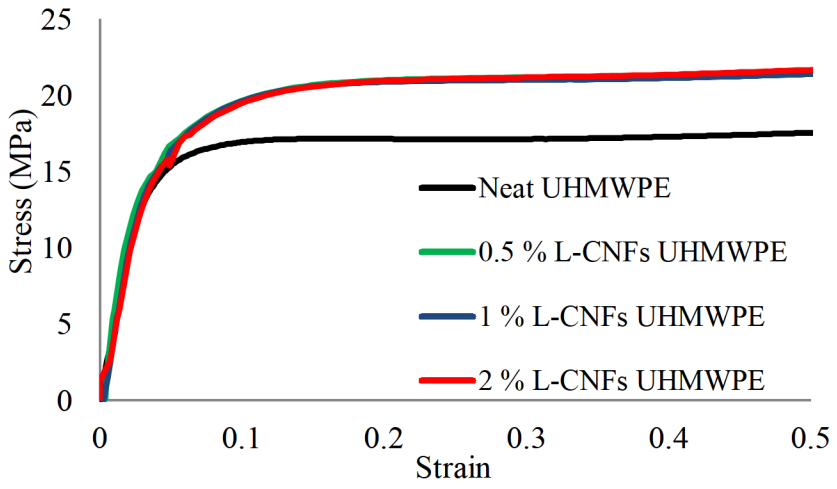

Figure 34. Representative strain-stress curves of neat UHMWPE and the L-CNFs nanocomposites.

Table 13. Results Obtained from Stress-Strain Curves of Neat UHMWPE and L-CNFs/UHMWPE Nanocomposites.

Sample designation	Young's Modulus (MPa)	Tensile Strength at Break (MPa)
neat UHMWPE	416 ±33	39 ±2
0.5% L-CNFs/UHMWPE	444 ±12	32 ±3
1% L-CNFs/UHMWPE	508 ±33	34 ±4
2% L-CNFs/UHMWPE	426 ±69	31 ±3

3.12 Conclusion

The crystallization kinetics for UHMWPE and the corresponding L-CNCs nanocomposites were studied by DSC and analyzed using the Avrami and isoconversional methods. The addition of L-CNCs resulted in relatively no difference in crystallization percent and time. However, the effective activation energies for the crystallization of the L-CNCs/UHMWPE nanocomposites were lower than neat UHMWPE, which suggests that the L-CNCs are acting as nucleating agents. L-CNFs/UHMWPE nanocomposites exhibited superior thermal stability compared to neat UHMWPE. However, the addition of L-CNCs to UHMWPE led to a decrease in the thermal stability of the nanocomposites.

We found that the addition of L-CNCs and L-CNFs in UHMWPE significantly improved Young's modulus of UHMWPE nanocomposites. Whereas, the tensile strength, elongation at break, and energy dissipation properties are unaffected in the presence of L-CNCs. The significant enhancement in Young's modulus shows that the

coating of lignin on CNCs and CNFs improved the dispersion of CNCs and CNFs by preventing re-aggregation of the nanofillers in hydrophobic UHMWPE. The addition of L-CNCs led to a higher Young's modulus than L-CNFs at the same filler loading. Furthermore, the addition of 5 wt.% of L-CNCs in UHMWPE increased the elastic modulus and loss modulus values. The increases were attributed to strong fiber-matrix interfacial bonding, better dispersion and distribution of nanofillers, and large aspect ratios of the fibers.

In summation, our research shows by reinforcing UHMWPE with cellulose nanoparticles at low-loadings enhances the material's properties. Corresponding to DMA data, the L-CNCs/UHMWPE nanocomposites show improvement in energy dissipation and may lead to new generations of lightweight armor that provide both protection and mobility for Soldiers. This work demonstrates that the right materials design approaches have the potential to make big impacts on defense technologies

CHAPTER 4

HIGH-DENSITY POLYETHYLENE (HDPE) NANOCOMPOSITES RESULTS & DISCUSSION

4.1 General Overview

The initial use of nanocellulose as a reinforcement in high-density polyethylene was first reported by Boldizar et al.[152] Favier et al. later reported the strong reinforcing effects of small amounts of nanocellulose.[153] Their research showed that at low nanocellulose loading, the nanocomposites had significantly higher mechanical properties than the neat polymer. The improvement of the formation of the nanocellulose network within the nanocomposites was attributed to the percolation of the nanocellulose whiskers.[153]

The CNCs used for this study have been modified by coating lignin on the surface, as discussed in Chapter 1. Lignin-coated cellulose nanocrystals (L-CNCs) are a potential candidate for the fabrication of natural reinforced composites. It has been documented that nucleating agents such as L-CNCs can influence crystal morphology of polymer matrices resulting in a change in mechanical and crystallization properties of these nanocomposites.[42-43] In the present study, we have investigated the effect of the incorporation of L-CNCs in HDPE by high-torque melt-mixing. We have also examined the incorporation of L-CNCs in HDPE by high torque melt-mixing with in situ free radical reactions with maleic anhydride and a free radical catalyst, dicumyl peroxide

(DCP). The functionalization of HDPE by MA is an effective way to increase the polarity of HDPE.[34] HDPE-*g*-MA polymers have been widely used to improve interfacial adhesion between the phases in polymer-nanofiller systems.[86, 89] It has been reported that the incorporation of CNCs in HDPE tends to aggregate to form agglomerates because of strong van der Waal's forces and hydrogen bonding, which makes the dispersion of CNCs in HDPE challenging.[154] Therefore, in order to achieve a better dispersion, MA is grafted on HDPE to create a hydrophilic surface to interact with the L-CNCs. For the neat HDPE, lignin-coated cellulose nanocrystals/high-density polyethylene (L-CNCs/HDPE), and lignin-coated cellulose nanocrystals/functionalized high-density polyethylene (L-CNCs/*f*HDPE) nanocomposites crystallization, mechanical and thermomechanical behaviors were investigated by DSC, DMA, TGA, melt-rheology, and tensile testing. The methods of preparation of these materials are described in Chapter 2. The results obtained are analyzed and interpreted within the framework of crystallization kinetic models for predicting the crystallization and effective activation energy behavior of HDPE nanocomposites. It is expected that the results of this study will provide a basis for a better understanding of developing thermoplastic nanocomposites reinforced with L-CNCs with improved properties.

4.2 Melt-Processed Neat HDPE and HDPE Nanocomposites

Neat HDPE, L-CNCs/HDPE, and L-CNCs/*f*HDPE nanocomposites were weighed and dried for 60 min at 90 °C to remove water. The L-CNCs/HDPE nanocomposites were prepared by adding HDPE to the melt-mixer over a 3 min time span, followed by

the addition of L-CNCs over 5 min and then melt-mixing continued for a total of 10 min. The MA grafted samples were prepared by initially melt-mixing the HDPE pellets for 3 min, followed by the addition of DCP for 30 seconds. MA was added, and melt-mixed for 2 min, and then the appropriate loadings of L-CNCs were added, and melt-mixing continued for a total of 11 min. The samples changed from dry-free flowing powders to large solid masses upon melt-mixing. Following melt-mixing, the samples exhibited a uniform light-brown to dark-brown color as the L-CNC loading increased, indicating a uniform dispersion and distribution of the filler throughout the composite, as shown in Figures 35 and 36. The presence of L-CNCs could be identified by the brownish color of the sample. Increased loadings of L-CNCs caused a steadily decreasing appearance of the original opaque white HDPE, and the samples took on the appearance of L-CNCs. After melt-mixing, the samples were broken up upon removal from the melt-mixer. Neat HDPE was also melt-mixed and characterized to compare to nanocomposites. Following melt-mixing, all samples were characterized, as described in Chapter 2.

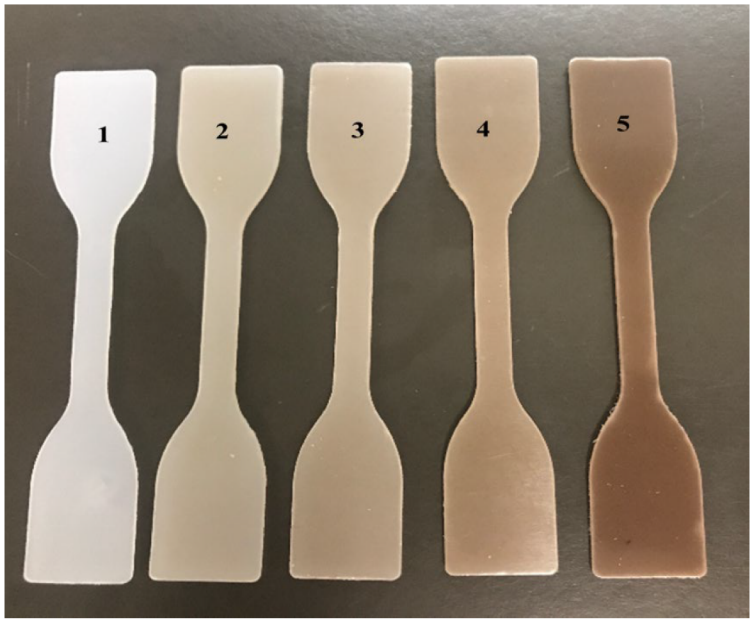

Figure 35. HDPE samples were designated as 1, 2, 3, 4 and 5, respectively for neat HDPE, 0.5% L-CNCs/HDPE, 1% L-CNCs/HDPE, 2% L-CNCs/HDPE and 5% L-CNCs/HDPE.

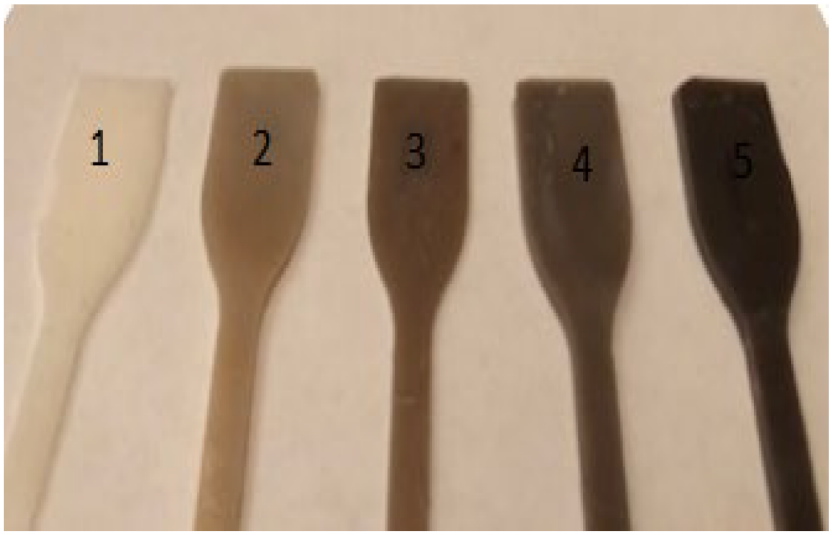

Figure 36. HDPE samples were designated as 1, 2, 3, 4 and 5, respectively for neat HDPE, 0.5% L-CNCs/*f*HDPE, 1% L-CNCs/*f*HDPE, 2% L-CNCs/*f*HDPE, and 5% L-CNCs/*f*HDPE.

4.3 Thermal Behavior of HDPE Nanocomposites by DSC

4.3.1 Thermal Behavior of Neat HDPE and L-CNCs/HDPE Nanocomposites

DSC studies were conducted to determine the effect of L-CNC loading on HDPE as compared to neat HDPE. Crystallization and melting behavior of HDPE in the presence of L-CNCs were investigated by analyzing DSC thermograms. Figure 37 shows the DSC cooling and second heating scans at 10 °C/min for neat HDPE and L-CNCs/HDPE nanocomposites. The DSC scans show the presence of crystallization exotherm, T_c, and melting endotherm, T_m, peaks. The incorporation of L-CNCs showed virtually no change in the melting behavior of HDPE.

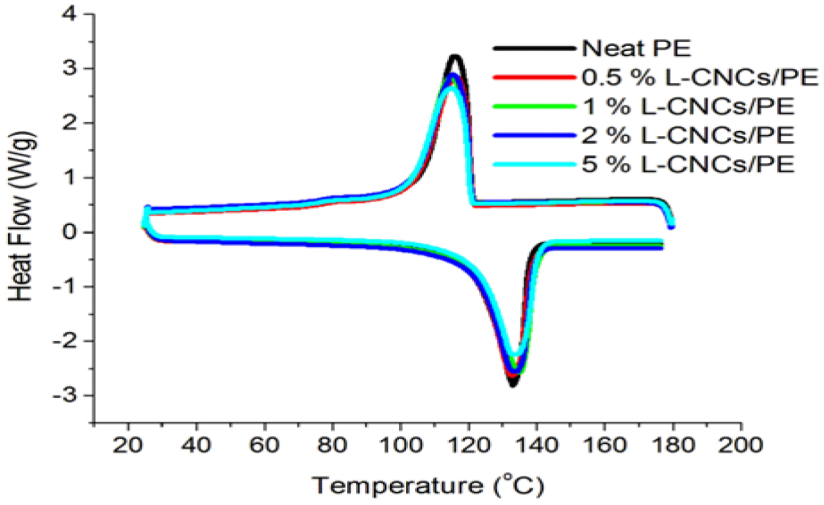

Figure 37. DSC scans for neat HDPE and L-CNCs/HDPE nanocomposites.

From the experimental ΔH_m values, percent crystallinity was calculated using equation 1, in Chapter 3, section 3.2; where, ΔH_m° is the standard enthalpy of melt for

100% crystalline HDPE, taken from the literature as 288.6 J/g.[120] The results show that the addition of L-CNC loadings from 0.5-1 wt.% did not affect the degree of crystallinity of HDPE, as shown in Table 14. The peak crystallization and melting temperatures for HDPE remained unchanged upon the incorporation of L-CNCs. Similar behavior was observed for Na-MMT clay in HDPE and LLDPE matrix.[155] However, at a high loading corresponding to 2 wt.% of L-CNCs, the percent crystallinity of HDPE decreased due to the agglomeration of L-CNCs in the polymer matrix.

Table 14. DSC Thermal Parameters of Neat HDPE and L-CNCs/HDPE Nanocomposites Derived from Cooling and Second Heating Scans.

Sample designation	X_c (%)	T_m (°C)	T_c (°C)	ΔH_m (J/g)
neat HDPE	69.7	133.9	115.3	199.3
0.5% L-CNCs/HDPE	74.1	133.9	115.9	198.8
1% L-CNCs/HDPE	75.0	134.0	115.2	194.8
2% L-CNCs/HDPE	70.0	132.6	116.0	194.3

4.3.2 Thermal Behavior of L-CNCs/Functionalized High-Density Polyethylene (*f*HDPE) Nanocomposites

HPDE compositions were made to determine the effect of L-CNCs, MA, and DCP on HDPE. DSC studies were conducted to assess the effect of L-CNC loading on functionalized HDPE as compared to neat HDPE. The DSC results for L-CNCs/functionalized HDPE nanocomposites are present in Table 15. These results show

that the grafting of MA on HDPE did not enhance the thermal properties upon the addition of L-CNCs.

Table 15. Thermal Parameters of Neat HDPE and L-CNCs/*f*HDPE Nanocomposites Derived from Cooling and Second Heating Scans.

Sample designation	X_c (%)	T_m (°C)	T_c (°C)	ΔH_m (J/g)
neat HDPE	69.7	133.9	115.3	199.3
0.5% L-CNCs-*f*HDPE	69.2	133.1	115.5	196.9
1% L-CNCs-*f*HDPE	-	-	-	-
2% L-CNCs-*f*HDPE	71.1	131.5	116.2	199.4
5% L-CNCs-*f*HDPE	-	-	-	-

4.4 Determination of Viscoelastic Properties of HDPE Nanocomposites by DMA

4.4.1 Viscoelastic Properties of Neat HDPE and L-CNCs/HDPE Nanocomposites

The dynamic mechanical properties of HDPE and L-CNCs nanocomposites at 0.5 to 2 wt.% loadings of L-CNCs were studied. Figure 38 presents the effect of L-CNC loading on the storage modulus, G′, of HDPE over a range of temperatures, 30 to 135 °C. The G′ values for all samples decreased sharply as the temperature approached the melting point. At low temperatures, the addition of 0.5 wt.% of L-CNCs decreased as compared to neat HDPE. The parameter G′ shows a gradual increase with an increase in L-CNC loadings. The addition of 1 and 2 wt.% of L-CNCs G′ values are higher than neat HDPE, which may be attributed to L-CNCs acting as reinforcing agents.[143] Plots of G″ as a function of temperature for neat HDPE and the L-CNCs/HDPE nanocomposites are

shown in Figure 39. HDPE exhibits a loss peak around a temperature of 45 °C, which corresponds to the α-transition region. All L-CNCs/HDPE nanocomposites exhibit higher G″ values except for the addition of 0.5 wt.% L-CNCs as compared to the neat HPDE α-relaxation peak. The peak intensity increased with the 1 and 2 wt.% loading of L-CNCs in HDPE.

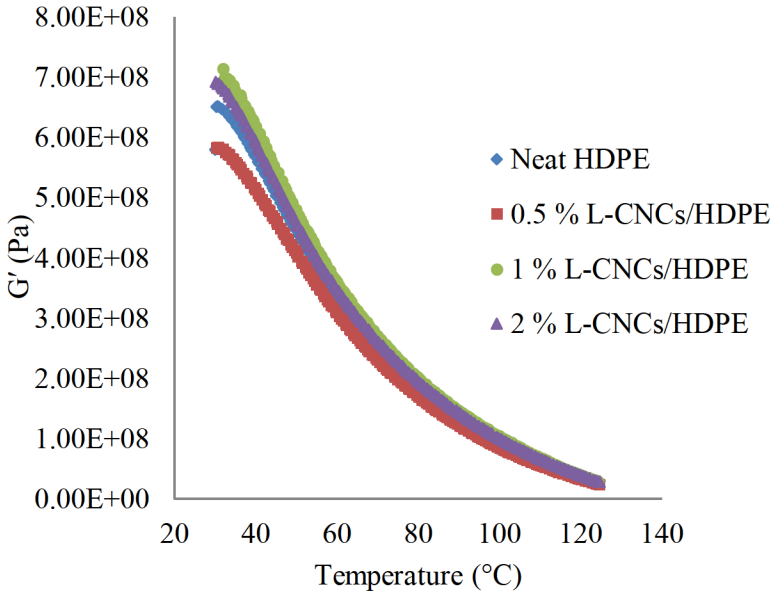

Figure 38. Storage modulus (G′) of neat HDPE and L-CNCs/HDPE nanocomposites as a function of temperature.

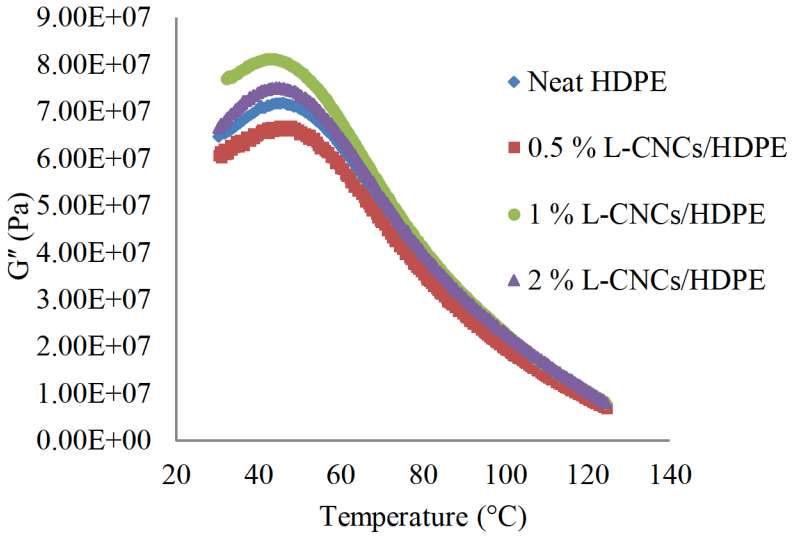

Figure 39. Loss modulus (G″) of neat HDPE and L-CNCs/HDPE nanocomposites as a function of temperature.

Figure 40 shows the variation of the damping parameter, tan δ as a function of temperature for neat HDPE and the L-CNCs/HDPE nanocomposites. There is relatively no change in the peak intensity with the addition of L-CNCs. However, the slight increase with 1 wt.% is attributed to the restricted movement in the macromolecular chains in the surface layer and the interaction between the HDPE and L-CNCs.[143]

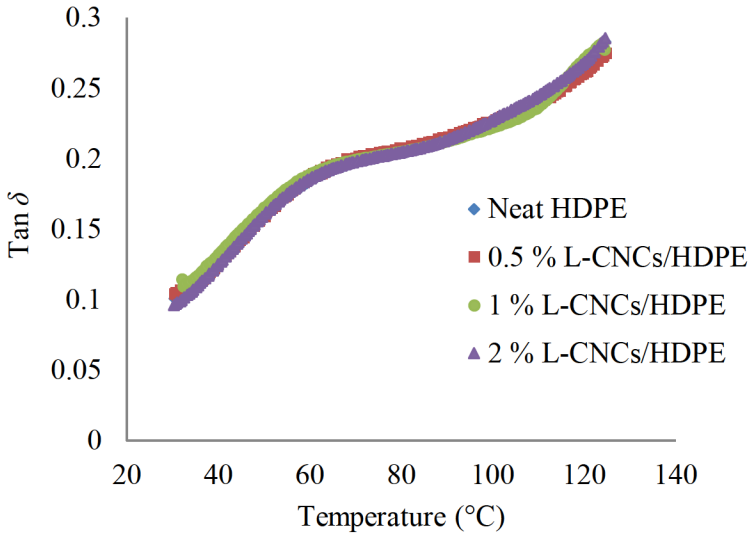

Figure 40. Tan δ of neat HDPE and L-CNCs/HDPE nanocomposites as a function of temperature.

4.4.2 Viscoelastic Properties of L-CNCs/Functionalized HDPE Nanocomposites

The dynamic mechanical properties of functionalized HDPE with the incorporation of L-CNCs have been studied by DMA. Figures 41, 42, and 43 present G′, G″, and tan δ plots as a function of temperature for neat HDPE and L-CNCs/*f*HPDE nanocomposites. The general shape and transitions of L-CNCs/*f*HDPE nanocomposites were similar to L-CNCs/HDPE nanocomposites, but the corresponding values and intensity for the L-CNCs/*f*HDPE nanocomposites were similar; if not, lower than the L-CNCs/HDPE nanocomposites. As shown in Figure 41, there is a decrease in the storage modulus, and this is due to the presence of MA, which decreased the interfacial attraction between the polymer and filler.[143] However, the G″ values of 2% L-CNCs/*f*HDPE correspond to neat HDPE, which may be attributed to the enhanced interaction with high

loadings of L-CNCs in the presence of the coupling agent, which decreases the molecular mobility of the polymer chains.[143] There is relatively no change in the tan δ values with the addition of L-CNCs in *f*HDPE as shown in Figure 43.

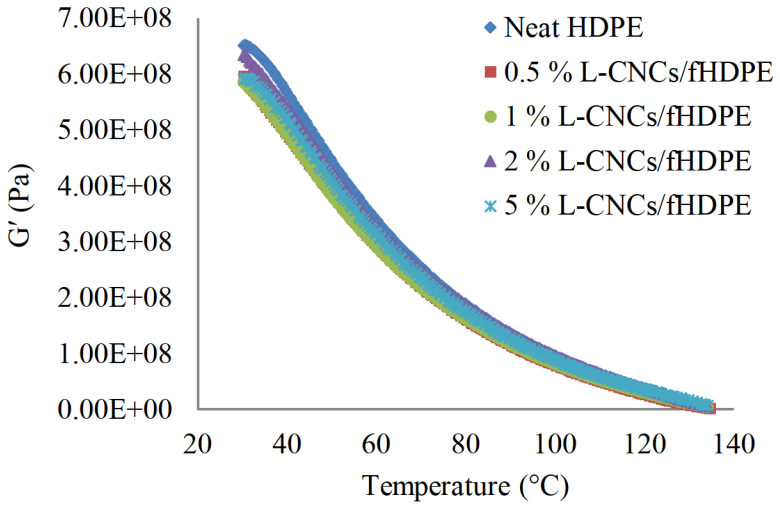

Figure 41. Storage modulus (G′) of neat HDPE and L-CNCs/*f*HDPE nanocomposites as a function of temperature.

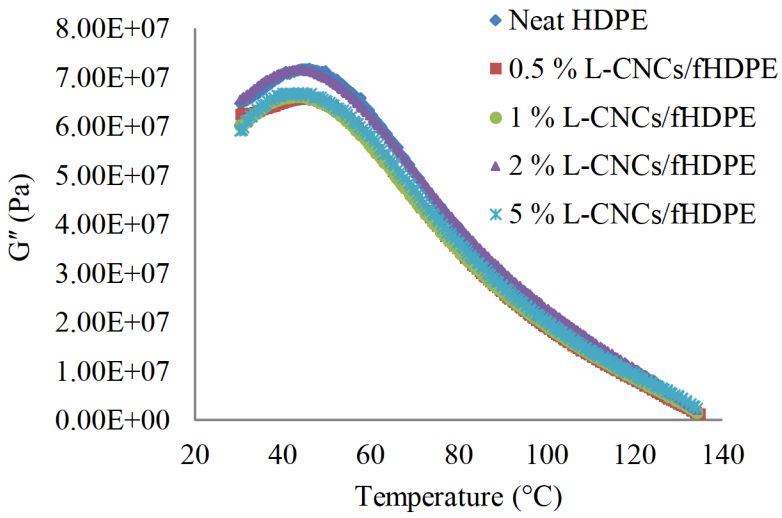

Figure 42. Loss modulus (G″) of neat HDPE and L-CNCs/HDPE nanocomposites as a function of temperature.

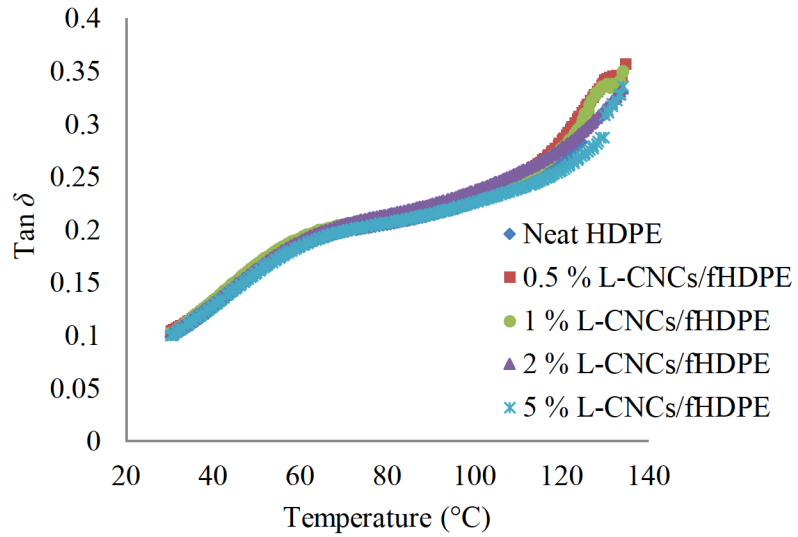

Figure 43. Tan δ of neat HDPE and L-CNCs/*f*HDPE nanocomposites as a function of temperature.

Isothermal time sweep studies using DMA were carried out in order to investigate the viscoelastic properties of neat HDPE and L-CNCs/*f*HDPE nanocomposites. Figures 44, 45, and 46 present the plots of G′, G″, and tan δ as a function of time for neat HDPE, and L-CNCs/*f*HPDE nanocomposites at 30 °C. The storage modulus values for all nanocomposites exhibited lower G′ values than neat HDPE as a function of time, as shown in Figure 44, which may be due to the plasticizing activity of some degraded MA under dynamic stress. In Figure 45, the addition 2 wt.% L-CNCs loss modulus values were similar to that of neat HDPE. All other nanocomposites dissipated less energy over time as compared to neat HDPE. For the L-CNCs/*f*HDPE nanocomposites, the damping parameter showed relatively no change in tan δ values over time, as shown in Figure 46.

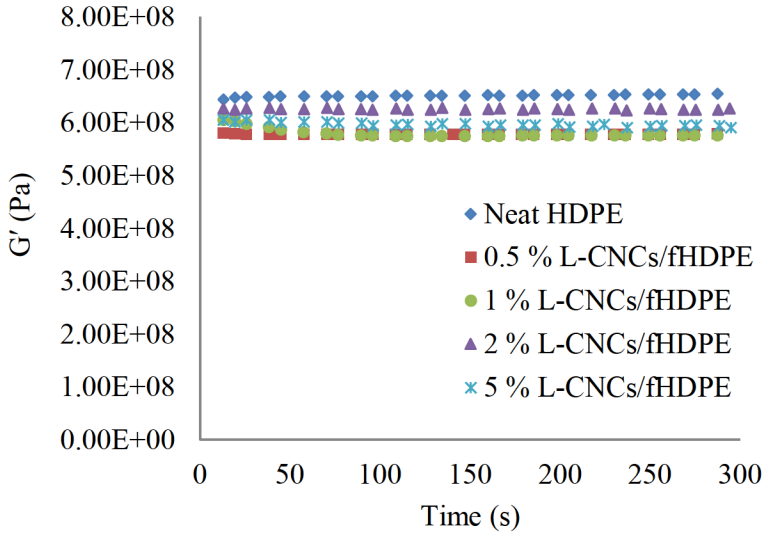

Figure 44. Dynamic time sweep experiment showing the variation of the storage modulus (G′) as a function time.

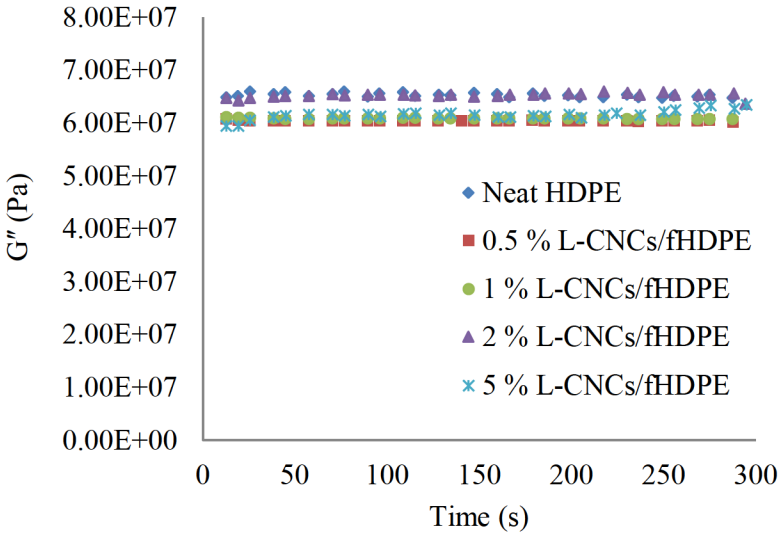

Figure 45. Dynamic time sweep experiment showing the variation of the loss modulus (G″) as a function of time.

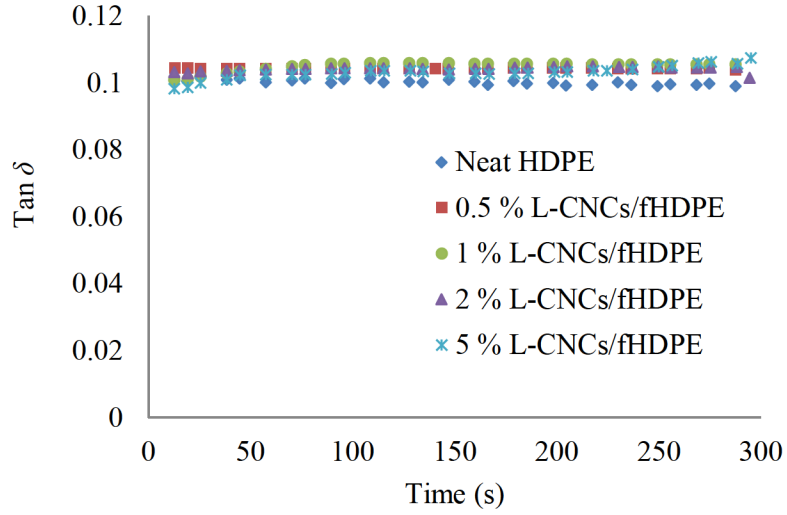

Figure 46. Dynamic time sweep experiment showing the variation of tan δ as a function of time.

4.5 Melt-Rheological Properties of HDPE Nanocomposites

It is important to study the rheological properties in order to understand the physical properties of polymer/filler nanocomposites. Rheological properties can help determine the internal structure and processability of nanocomposites. Information about the microstructure, dispersion of fillers, and the interactions between polymer matrix and fillers can also be determined. Adding fillers to polymers such as HDPE changes its rheology, influencing both the way the melt processes and the properties of the final product.[156]

4.5.1 Melt-Rheology Analysis of Neat HDPE and L-CNCs/HDPE Nanocomposites

The plots of storage modulus, G′ against angular frequency, ω at given loadings of L-CNCs are shown in Figure 47. It is interesting to note that 0.5 wt.% of L-CNCs/HDPE nanocomposite and neat HDPE exhibits the highest G′ values. Further addition of L-CNCs decreased G′ values, and the effect is pronounced at low and high frequencies. Figure 48 presents the plots for G″ values as a function of frequency for neat HDPE and L-CNCs/HDPE nanocomposites. An addition of 0.5 wt.% of L-CNCs behaved similarly to that of neat HDPE. Further addition of L-CNC loading resulted in low G″ values, which is due to the lack of interaction between the L-CNCs and HDPE. For the neat HDPE and L-CNC/HDPE nanocomposites, tan δ decreases as the angular frequency (ω) increases, this is indicative of liquid-like materials, as shown in Figure 49. For all samples, there is a gradual decrease in the intensity at frequencies below 5 rad/s and above 100 rad/s. With the addition of L-CNCs there is a change in the slope for all

nanocomposites between the frequencies of 10 and 100 rad/s. The change in slope suggests that there is a change in the microstructure, and a network filler structure has formed.[157] The decrease of the slope with increase loading suggests that the material begins to move towards more solid-like behavior.[156] At low frequencies, the filler interaction with the polymer slightly inhibits chain mobility, but as the frequency increases, these weak interactions are quickly overcome, and the resin returns to its viscous flow character. Addition of 0.5 and 1 wt.% L-CNC loadings is shown to absorb less energy over the frequency range of 0.1 to 1000 rad/s. Overall, 2 wt.% L-CNC loading retained a higher intensities as compared to neat HDPE and HDPE nanocomposites. Similar rheological behavior was observed for HDPE with the incorporation of pristine multiwall carbon nanotubes (CNT).[157] Figure 50 presents the miscibility at 1 and 2 wt.% likely leads to a better dispersion with some level of HDPE chain-L-CNC interaction, i.e., weak van der Waals forces, and this could probably cause decreased chain entanglements and more free volume in the melt, thus resulting in lower complex viscosity, η*. This effect is similar to that observed in the case of storage modulus as shown in Figure 47. However, at low L-CNC loadings, it is not completely miscible at the molecular level and aggregates are formed, which hinders the flow and raises the viscosity. These results indicate that the filler acts as a barrier to chain flow.[157] The rheological properties of L-CNCs/HDPE nanocomposites were studied using Han plots of G′ versus G″ of neat HDPE and L-CNCs/HDPE nanocomposites. This plot indicates the sensitivity of rheological properties to composition and frequency. As shown in Figure 51, the plots for both neat HDPE and 0.5% L-CNCs/HDPE follow the

same trend, with no changes in the slope. However, the slope of the plots increases sharply, as the L-CNC loading exceeds 0.5 wt.%. This indicates that the rheological behavior of HDPE is affected by L-CNC loading significantly at high frequencies and high loadings of L-CNCs. Linear viscoelastic characteristics were derived from the results of rheological measurements, as shown in Figure 52, using Cole-Cole plots for neat HDPE and L-CNCs/HDPE nanocomposites. For these plots, the η'' parameter, the imaginary viscosity, is plotted against dynamic viscosity, η'. The plot should be a perfect semi-circle if high order structures are absent and the relaxation behavior of the melt can be described by single relaxation times.[158-159] Data shown in Figure 52 indicated the addition 2 wt.% L-CNCs led to an increase in the elastic behavior of the nanocomposites and a large relaxation time, indicating the presence of L-CNC aggregates. Lower loadings, 0.5 wt.%, behaved similarly to neat HDPE.

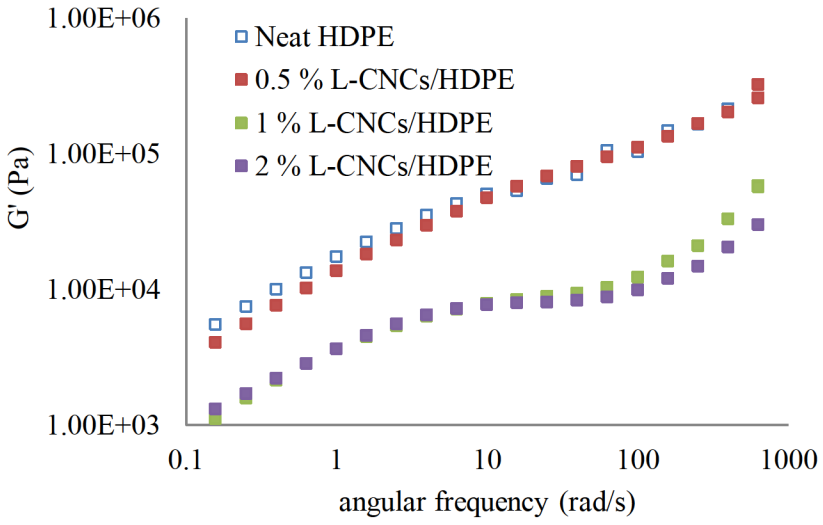

Figure 47. Storage modulus (G′) of neat HDPE and L-CNCs/HDPE nanocomposites as a function of angular frequency at 150 °C.

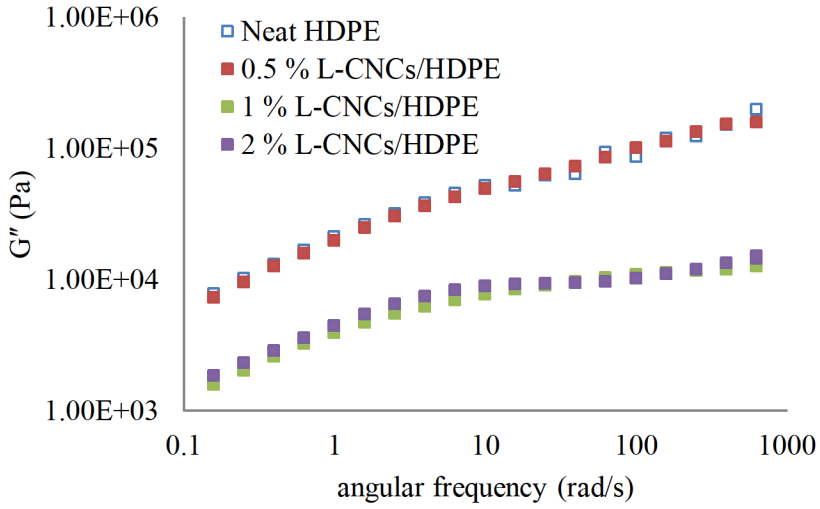

Figure 48. Loss modulus (G″) of neat HDPE and L-CNCs/HDPE nanocomposites as a function of angular frequency at 150 °C.

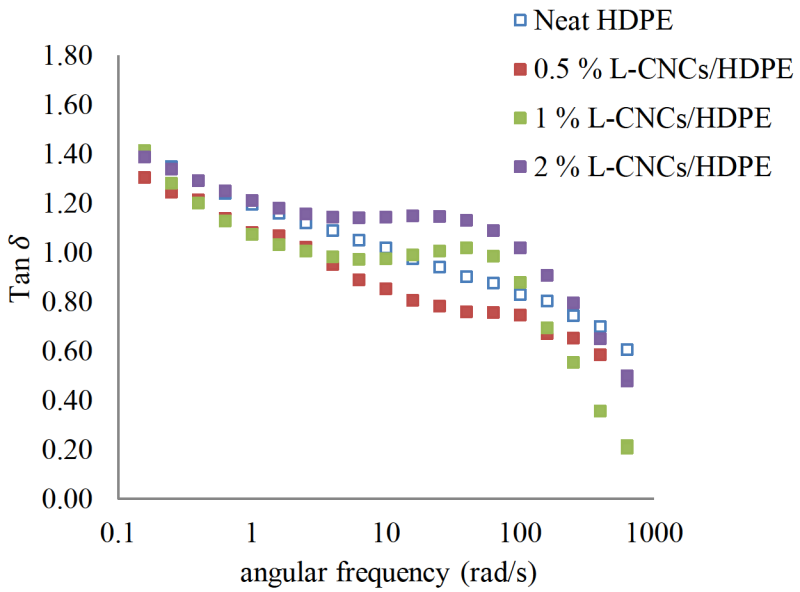

Figure 49. Tan δ of neat HDPE and L-CNCs/HDPE nanocomposites as a function of angular frequency at 150 °C.

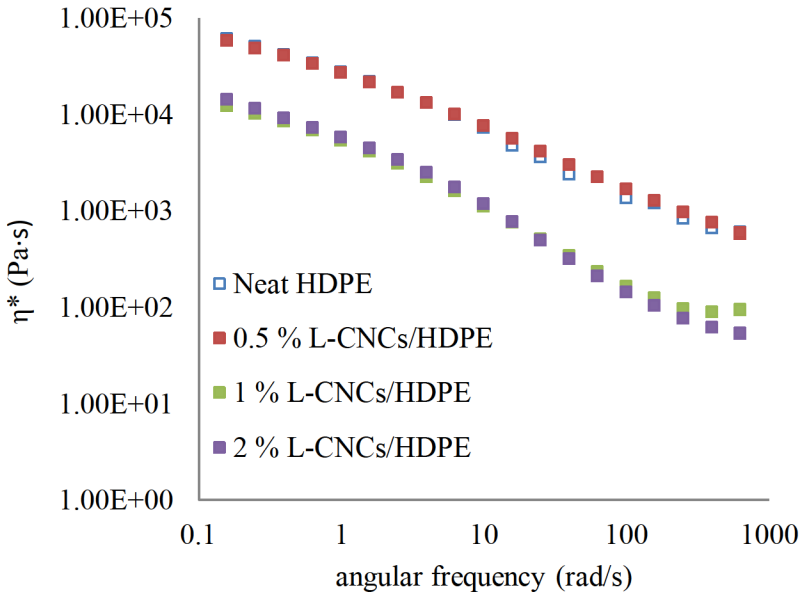

Figure 50. Complex viscosity (η*) of neat HDPE and L-CNCs/HDPE nanocomposites as a function of angular frequency at 150 °C.

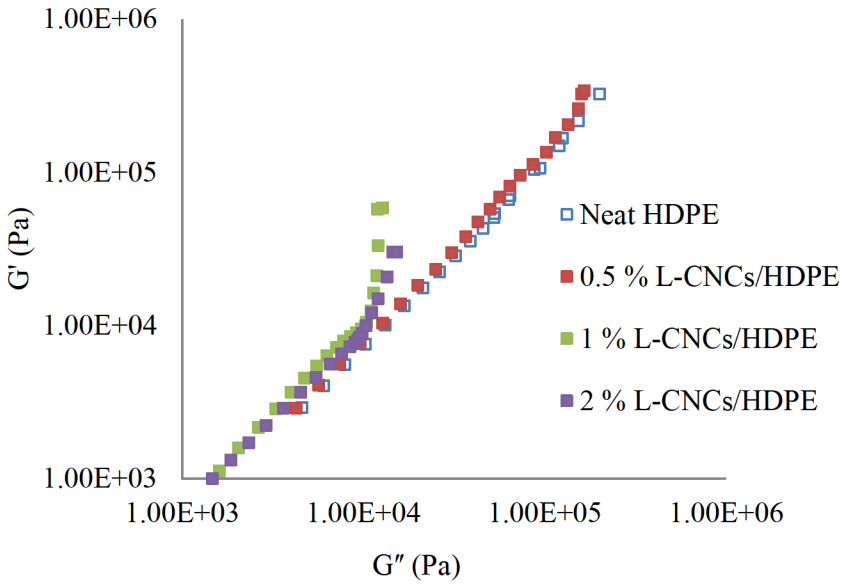

Figure 51. Han plots of neat HDPE and HDPE nanocomposites.

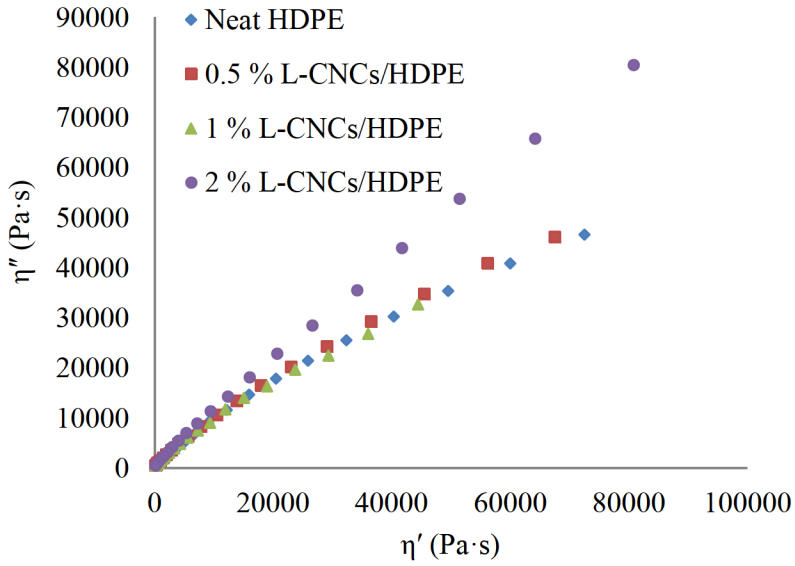

Figure 52. Cole-Cole plots of neat HDPE and HDPE nanocomposites.

Figures 53 and 54 presents the storage modulus, G′, as a function of L-CNC loading at low and high frequency, respectively. With increasing L-CNC loading, there is a decrease in the G′ at a low angular frequency of 0.1578 rad/s. This change in *G′* is attributed to the agglomeration of L-CNCs in HDPE. The 1 and 2 wt.% L-CNCs/HDPE nanocomposites behaved similarly at a high angular frequency of 250 rad/s, as shown in Figure 54. However, the addition of 0.5 wt.% L-CNCs at high frequency exhibited the highest storage modulus as compared to neat HDPE and all other nanocomposites.

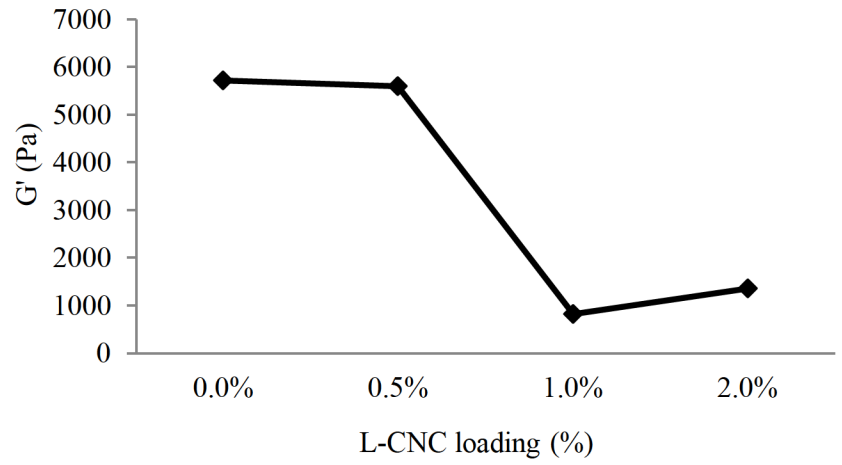

Figure 53. Storage modulus (G′) as a function of L-CNC loading measured at the lowest angular frequency (0.1578 rad/s).

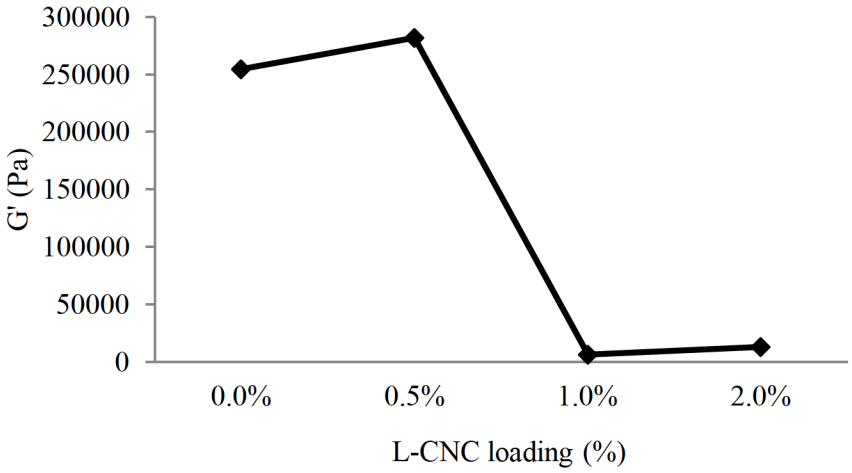

Figure 54. Storage modulus (G′) as a function of L-CNC loading at the highest angular frequency (250 rad/s).

4.5.2 Melt-Rheology Analysis of L-CNCs/*f*HDPE Nanocomposites

The variation of storage modulus, G′, loss modulus, G″, tan δ, and complex viscosity, η*, as a function of angular frequency, ω, at 150 °C for HDPE and L-

CNCs/*f*HDPE nanocomposites are shown in Figures 55, 56, 57, and 58, respectively. It is observed that G′, G″, and η* of HDPE increase with the addition of 0.5 wt.% L-CNCs. The improvement is attributed to a better dispersion of L-CNCs in functionalized HDPE, indicating that the coupling agent, MA, has a strong influence on the dispersion of L-CNCs.[36] The non-terminal and terminal rheological behavior can be studied through the slope of G′, G″ vs. ω plots at low and high-frequency regions, which can effectively be used to interpret the microstructure. Table 16 shows the results obtained for the non-terminal and terminal slopes for G′, G″ vs. ω plots at low frequencies of 0.1 – 1 rad/s, and at high-frequencies of 100- 628 rad/s. At a constant frequency, both G' and G" increase with the addition of 0.5 and 2 wt.% of L-CNCs. Furthermore, at a fixed L-CNC loading, both G' and G" increase with increasing frequency. The non-terminal behavior at low frequencies for *f*HDPE with the addition of 1 wt.% of L-CNCs is due to the formation of L-CNC networks, which reduces long-range motions of polymer chains. Due to the restriction of the polymer chains caused by the formation of L-CNC-networks, this can also lead to changes in the crystallization kinetics of the polymer matrix.[160] For the terminal slopes for G′, and G″ at high frequencies, the reduction in the slope for the L-CNCs/*f*HDPE nanocomposites is due also to the strong interaction of L-CNCs with *f*HDPE; confirming that the interfacial bonds improved the stress transfer from the matrix to filler. It is observed that the slope values in Table 16 for G′, G″ vs. ω plots showed no consistent trend with increasing loading. This could be various reasons: (1) thermo-oxidative degradation of polymer chains upon addition of MA, (2) aggregation of L-CNC

particles during melt-mixing, and (3) lack of sufficient interfacial interaction between filler and polymer chain.

Figure 57 shows the tan δ values of L-CNCs/*f*HDPE nanocomposites as a function of angular frequency at 150 °C. The addition of L-CNCs in functionalized HDPE caused a decrease in intensity as compared to neat HDPE, with 0.5% L-CNCs/HDPE nanocomposite absorbing the least amount of energy. The addition of 1 and 5 wt.% of L-CNCs in functionalized HDPE resulted in no significant change and behaved similarly to neat HDPE from 0.01 to 1000 rad/s. Figure 59 presents the plots of G′ versus G″, which is a typical Han plot. Plots for both neat HDPE and L-CNCs/*f*HDPE nanocomposites follow the same pathway. However, the slope increases with the addition of L-CNCs. Figure 60 presents the Cole-Cole plots of neat HDPE and L-CNCs/*f*HDPE nanocomposites. The addition of 0.5 wt.% of L-CNCs leads to an increase in the elastic behavior of the nanocomposites and a high relaxation time which is an indication of filler aggregates.[158]

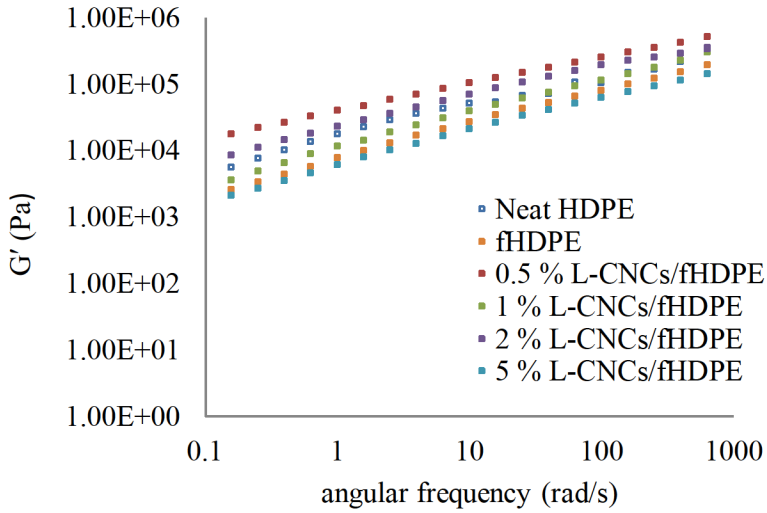

Figure 55. Storage modulus (G′) of neat HDPE, *f*HDPE, and L-CNCs/*f*HDPE nanocomposites as a function of angular frequency at 150 °C.

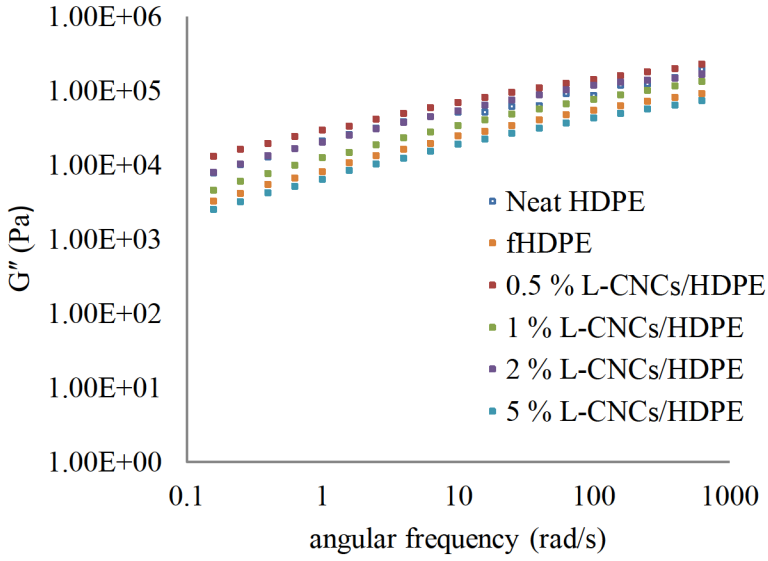

Figure 56. Loss modulus (G″) of neat HDPE, *f*HDPE, and L-CNCs/*f*HDPE nanocomposites as a function of angular frequency at 150 °C.

Table 16. Non-Terminal and Terminal Slopes of the Storage (G′) and Loss Moduli (G″).

Sample designation	Non-terminal Slopes		Terminal Slopes	
	G′	G″	G′	G″
neat HDPE	1.5307	1.3134	0.001968	0.001386
*f*HDPE	1.4510	1.2283	0.000836	0.000609
0.5% L-CNCs/*f*HDPE	1.0861	1.0476	0.001232	0.000823
1% L-CNCs/*f*HDPE	1.5490	1.3218	0.001744	0.000990
2% L-CNCs/*f*HDPE	1.3122	1.2288	0.000991	0.000581
5% L-CNCs/*f*HDPE	1.4197	1.2452	0.001410	0.000908

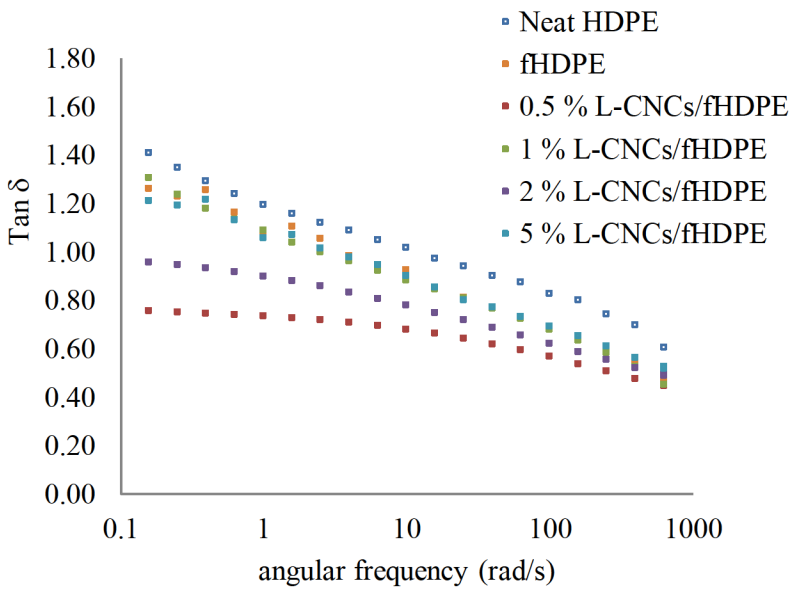

Figure 57. Tan δ of neat HDPE, *f*HPDE, and L-CNCs/*f*HDPE nanocomposites as a function of angular frequency at 150 °C.

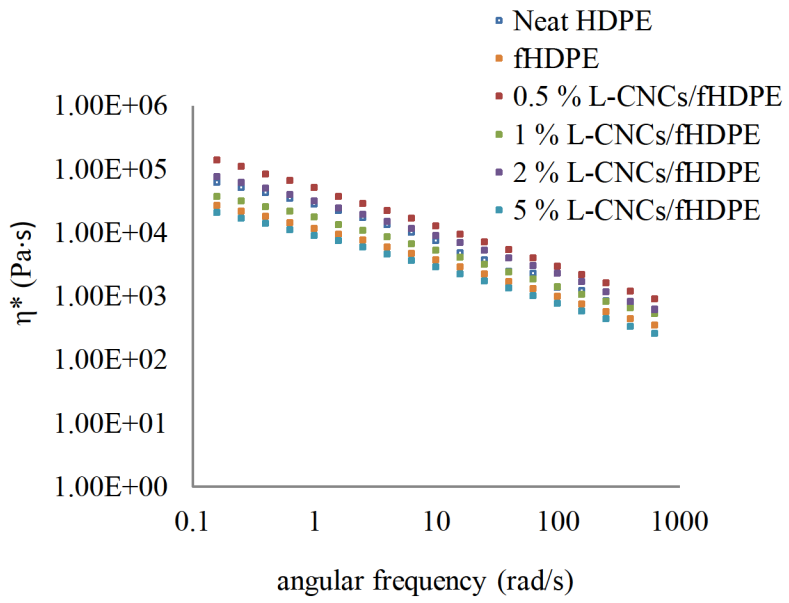

Figure 58. Complex viscosity (η*) of neat HDPE and L-CNCs/*f*HDPE nanocomposites as a function of angular frequency at 150 °C.

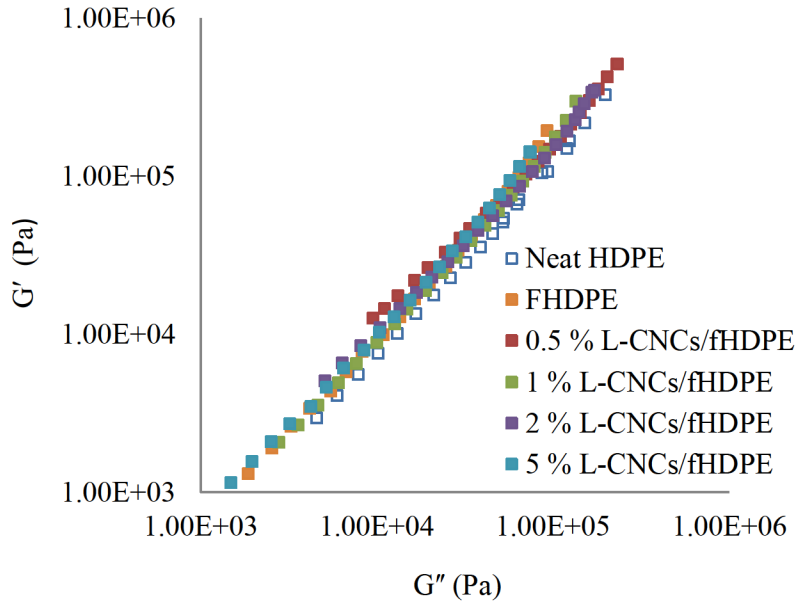

Figure 59. Han plots of neat HDPE and L-CNCs/*f*HDPE nanocomposites.

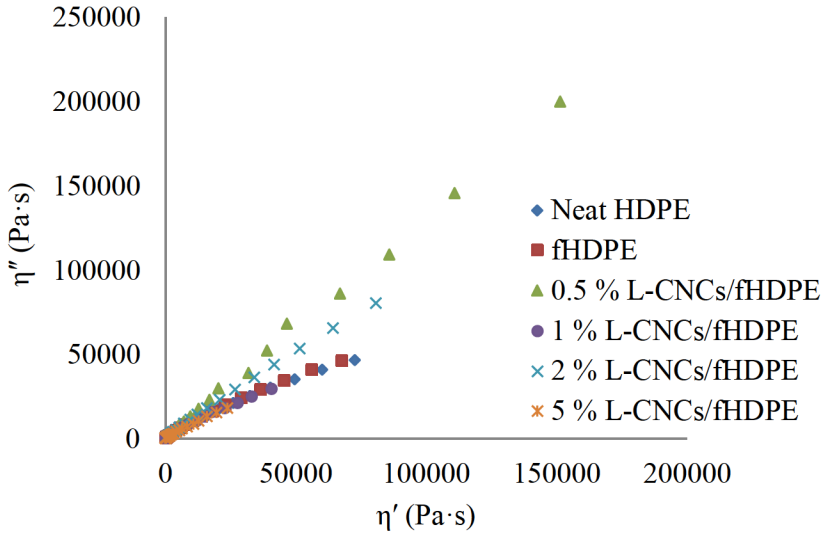

Figure 60. Cole-Cole plots of neat HDPE and L-CNCs/*f*HDPE nanocomposites.

Figures 61 and 62 shows the storage modulus, G′, at 150 °C for neat HDPE, 0.5% L-CNC/HDPE, and 0.5% L-CNC/*f*HDPE at low, and high frequency. At a low and high angular frequency of 0.1578 and 250 rad/s, respectively, there is improvement in the G′ values when L-CNCs are incorporated in *f*HPDE. The improvement is due to the increased interaction between L-CNCs and MA grafted on HDPE which resulted in better dispersion of L-CNCs.[50, 161]

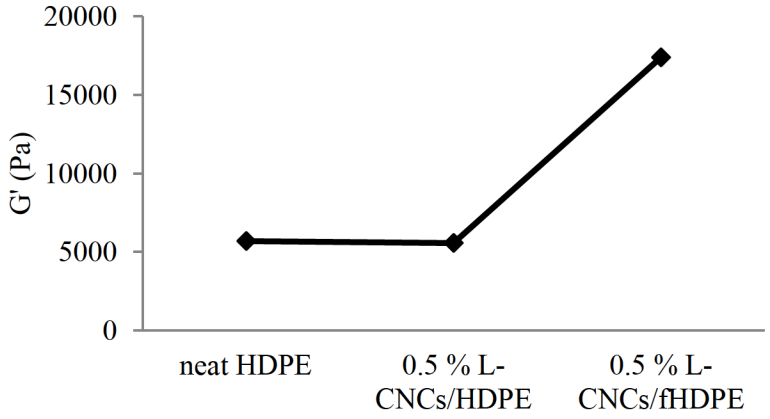

Figure 61. Neat HDPE, 0.5% L-CNCs/HDPE and 0.5% L-CNCs/*f*HDPE storage modulus (G′) values at the lowest angular frequency of 0.1578 rad/s.

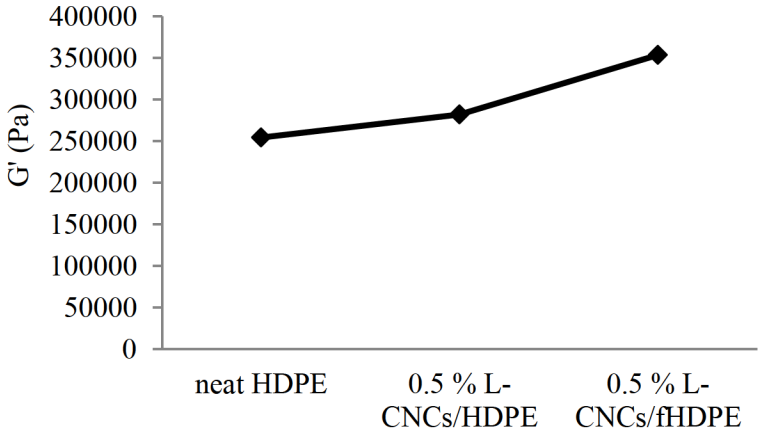

Figure 62. Neat HDPE, 0.5% L-CNCs/HDPE and 0.5% L-CNCs/*f*HDPE storage modulus (G′) values at the highest angular frequency of 250 rad/s.

4.6 Non-Isothermal Crystallization Behavior of HDPE Nanocomposites: Avrami Analysis

In order to better understand and interpret the effects of microstructure on the crystallization behavior of the L-CNCs/HDPE nanocomposite systems, a series of non-isothermal crystallization experiments were conducted. The samples were cooled at

controlled cooling rates of 1, 5, 10, 15, and 20 °C from the melt and the exotherms of the crystallization were analyzed. The obtained exothermic peaks of crystallization at different cooling rates are shown in Figure 63. Crystallization peaks were shifted to lower temperatures via an increase in ramp rates. Figure 63 show that increasing the cooling rates results in a decrease in the peak crystallization temperatures for all samples. In addition, the onset of crystallization temperature occurs at lower temperatures, and the crystallization exotherms become broader. In fact, as the cooling rate increases, the available response time of the polymer chains in order to overcome the nucleation energy barrier becomes shorter. Therefore, crystallization occurs at low temperatures resulting in enhanced nucleation rates. Figure 64 presents the relative crystallinity as a function of time for neat HDPE and L-CNCs/HDPE nanocomposites, exhibiting sigmoidal type behavior as expected. The first slope is indicative of the nucleation period; the second slope corresponds to the primary crystallization stage and, at higher degrees of relative crystallinity, > 85%, the third slope is indicative of secondary crystallization.

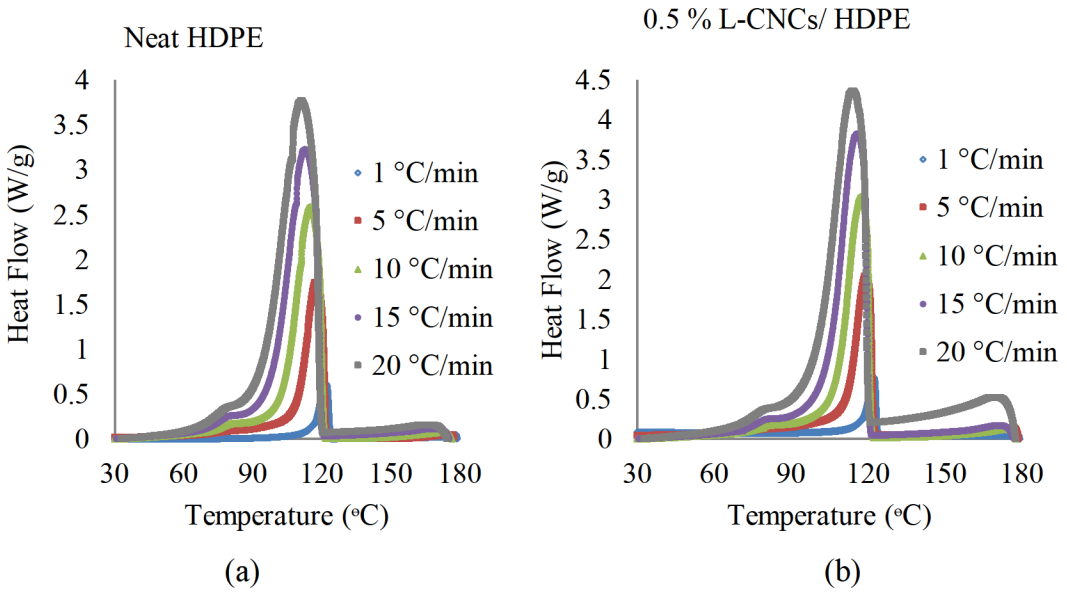

Figure 63. The heat flow of (a) neat HDPE and (b) 0.5% L-CNCs/HDPE nanocomposite as a function of temperature at various cooling rates.

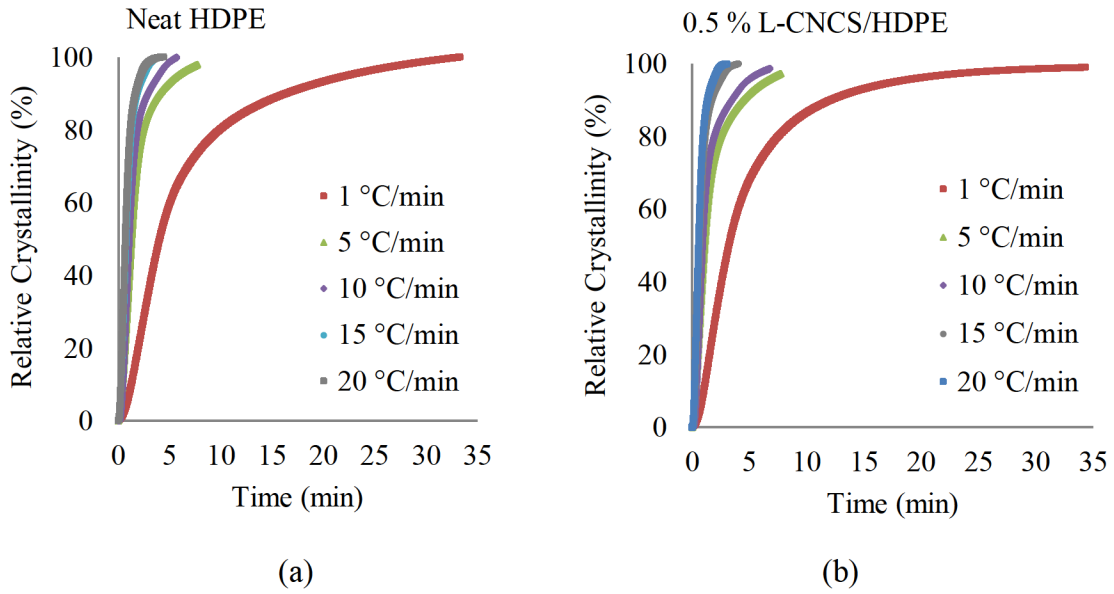

Figure 64. The relative degree of crystallinity of (a) neat HDPE and (b) 0.5% L-CNCs/HDPE nanocomposite as a function of time at various cooling rates.

Figure 65 presents ln[-ln (1-X_t)] versus ln t for each cooling rate, the value of n and k can be directly obtained from the slope and intercept of the best-fitted lines respectively, where both k and n are the parameters used to interpret the crystalline morphology and type of nucleation quantitatively. The crystallization parameters; n, and k for L-CNCs/HDPE nanocomposites calculated from the plot of ln[-ln(1-X_t)] vs. ln t as shown in Figure 65, are summarized in Table 17. For neat HDPE, the values of Avrami exponent, n, were non-integral and ranged from 1.5 to 2.1. Generally, the n value close to 2 indicates two-dimensional crystal growth and heterogeneous nucleation.[162] The k values of the L-CNC/HDPE nanocomposites are higher than those of neat HDPE, indicating faster crystallization.

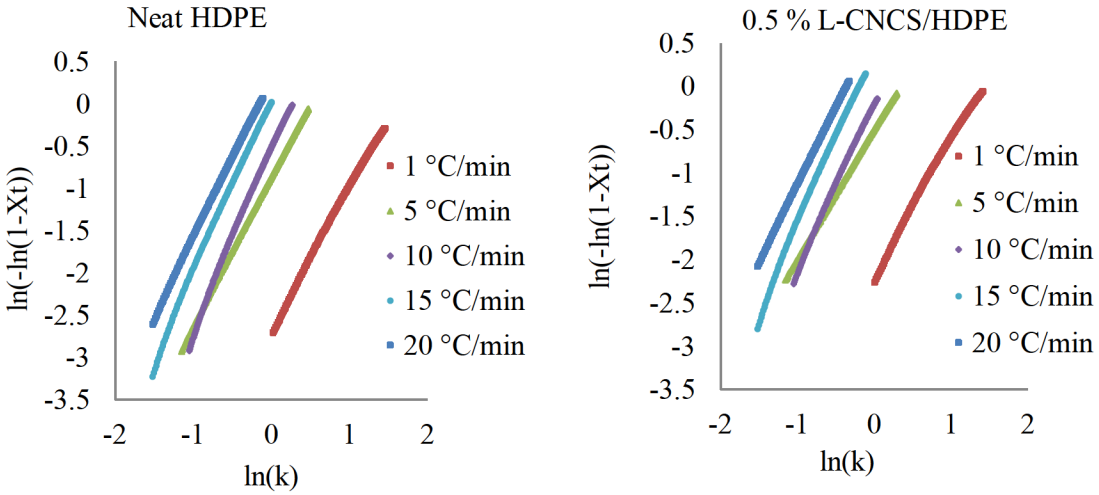

(a) (b)

Figure 65. Plots of ln[-ln(1-X_t)] versus ln t for (a) neat HDPE and (b) 0.5% L-CNCs/HDPE nanocomposites.

Table 17. Values of n, and k for Neat HDPE and L-CNCs/HDPE Nanocomposites Obtained from Avrami Analysis for Non-Isothermal Crystallization Processes.

	Cooling rate (°C/min)	Neat HDPE	0.5% L-CNCs/HDPE	1% L-CNCs/HDPE	2% L-CNCs/HDPE
n	1	1.7	1.5	1.5	1.6
	5	1.7	1.5	1.6	1.5
	10	2.1	1.9	2.0	2.0
	15	2.0	2.0	2.1	2.0
	20	1.9	1.8	1.8	1.9
k/min^{-1}	1	0.071	0.115	0.109	0.079
	5	0.417	0.606	0.635	0.519
	10	0.593	0.842	0.936	0.799
	15	1.055	1.532	1.629	1.100
	20	1.344	1.917	2.046	1.579

The crystallization time (t) can be calculated by converting temperature to time using Equation 11:[126]

$$t = \frac{T_0 - T}{\beta} \tag{11}$$

where T is the temperature at crystallization time t, T_0 is the initial temperature of crystallization, and β is the cooling rate.[126] The overall crystallization time (t_c), of the L-CNCs/HDPE nanocomposites at various cooling rates are given in Figure 66. The

addition of L-CNCs reduces the time it takes for HDPE to crystallize, which is a direct consequence of the remarkable nucleation effect caused by the L-CNCs. Table 18 shows the overall crystallization time (t_c), and percent crystallinity (X_c%) of neat HDPE and L-CNCs/HDPE nanocomposites at 1, 5, 10, 15 and 20 °C/min. At a cooling rate of 20 °C/min, 2% L-CNCs/HDPE nanocomposite showed no significant change in the amount of time it takes for HDPE to crystallize, as compared to the neat HDPE. All other nanocomposites tested showed a decrease in the t_c at all cooling rates in comparison to the neat HDPE, which is due to L-CNCs acting as a nucleating agent. At a cooling rate of 1 °C/min, the addition of L-CNCs increased the crystallinity from 3-4% as compared to the neat HDPE. For all other nanocomposites, there was no significant difference crystallinity in the nanocomposites as compared to the neat HDPE. It is important to note, the crystallinity increases as the cooling rate decreases for all specimens tested. At a cooling rate of 1 °C/min, the 0.5% nanocomposite exhibited a 4% increase in the crystallinity as compared to the neat HDPE. At high cooling rates, there was no significant difference in percent crystallinity for L-CNCs/HDPE nanocomposites. Similarly, Han et al. incorporated nanocellulose in polyurethane during isothermal crystallization by using the Avrami model and found that nanocellulose acts as nucleating agents.[163]

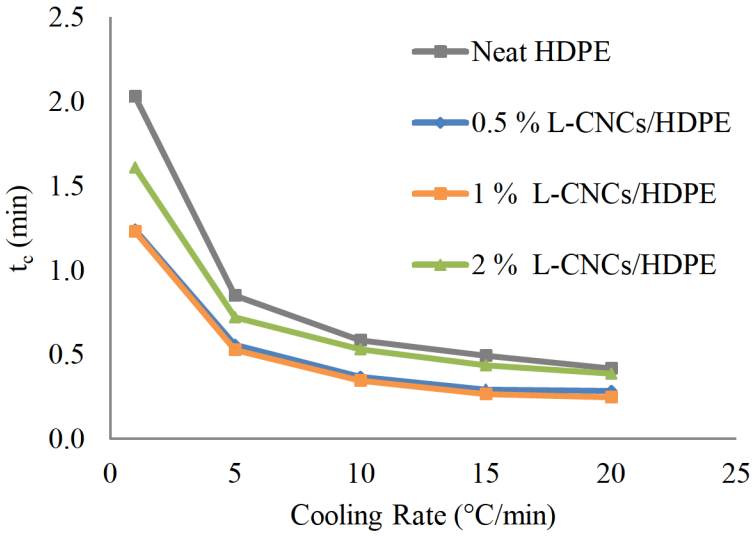

Figure 66. Overall crystallization time (t_c) of the L-CNCs/HDPE nanocomposites at various cooling rates.

Table 18. Overall Crystallization Time (t_c) as Compared to the Percent Crystallinity (%) of the L-CNCs/HDPE Nanocomposites at Various Cooling Rates.

Sample designation	1 °C/min		5 °C/min		10 °C/min		15 °C/min		20 °C/min	
	t_c (min)	X_c (%)	t_c (min)	X_c (%)	t_c (min)	X_c (%)	t_c (min)	X_c (%)	t_c (min)	X_c (%)
neat HDPE	2.0	80.1	0.9	79.8	0.6	76.7	0.5	74.4	0.4	73.7
0.5% L-CNCs/ HDPE	1.2	83.9	0.6	79.4	0.4	76.0	0.3	74.5	0.3	73.0
1% L-CNCs/ HDPE	1.2	83.0	0.5	80.4	0.3	77.3	0.3	75.6	0.2	74.3
2% L-CNCs/ HDPE	1.6	84.3	0.7	80.5	0.5	76.5	0.4	73.7	0.4	74.0

4.7 Determination of the Effective Activation Energy of Non-Isothermal Crystallization using the Isoconversional Approach

The activation energy of the crystallization process is an important kinetic parameter to understanding and interpreting the interrelation of the microstructure and crystallization process. Using the isoconversional method proposed by Vyazovkin and Friedman,[137] the effective activation energies, E_α, are calculated for every degree of crystallinity or extent of conversion, α, using equation 6 in Chapter 3, section 4 from DSC experimental data. The calculated effective activation energies plotted as a function of the relative extent of crystallization for neat HDPE and L-CNCs/HDPE nanocomposites are presented in Figure 67. The evaluated E_α is negative and increased with the extent of α and decreased in temperature for both the neat HDPE and L-CNCs/HDPE nanocomposites. The calculated E_α values increased from -492 to -76 kJ/mol in correspondence with an increase in melt conversion from 0.75 to 1α. This indicates that the HDPE crystallization rate increases with decreasing temperature. The E_α value is determined as the temperature-dependent relative contribution of the mass transport and nucleation processes to the crystallization growth rate and thus understood as overall effective activation energy, E_α rather than the activation energy, representing the magnitude of the energy barrier. The neat HDPE and L-CNCs/HDPE nanocomposites show low negative effective activation energies. These low values indicate that the crystallization rate in nanocomposites increases with decreasing temperature and ultimately controlled by the nucleation rate. The observed results suggest that initially, it is easier for neat HDPE and the HDPE nanocomposites to

crystallize while it becomes rather difficult to crystallize greater than 0.80α, thus indicating that more energy is required to transport the HDPE-chains to the crystallization surface with decreasing temperature.

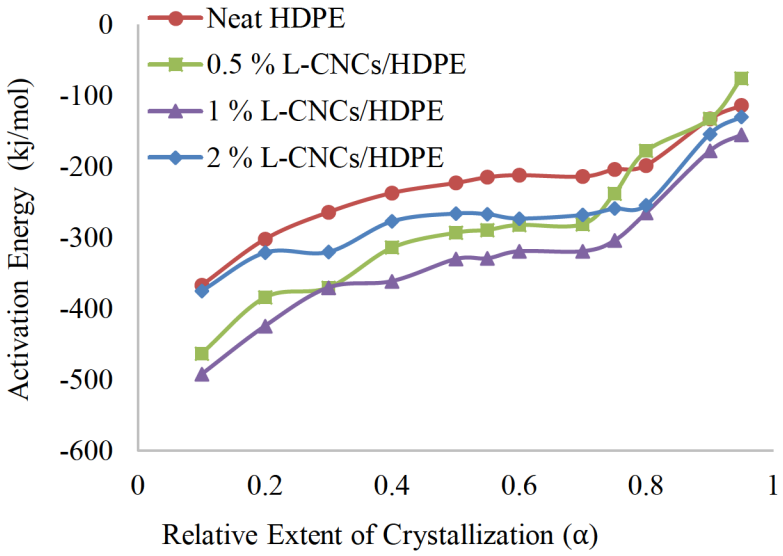

Figure 67. Dependence of the effective activation energy on the relative extent of crystallization.

The dependence of the effective activation energy as a function of the average temperature for neat HDPE and L-CNCs/HDPE nanocomposites is shown in Figure 68. The E_α values are highly negative as the average temperature decreases; this is indicative of the crystallization rate being minimum at temperatures closer to the melting point. The E_α dependence against the average temperature plot of HDPE demonstrates an abrupt change in upward direction range at 379 K that corresponds to the extent of conversion of 0.8α. Figure 69 presents the variation of the average temperature with the relative extent of crystallization. The addition of L-CNCs shows an increase in temperatures from 0-

0.8α. Overall, the results indicate that L-CNCs act as heterogeneous nucleating filler by accelerating the non-isothermal process. Similarly, Han et al. incorporated nanocellulose in polyurethane during isothermal crystallization and found that nanocellulose act as nucleating agents due to the lower activation energies of crystallization as well as shorter half-times of the nanocomposite samples as compared to the neat polymer.[163]

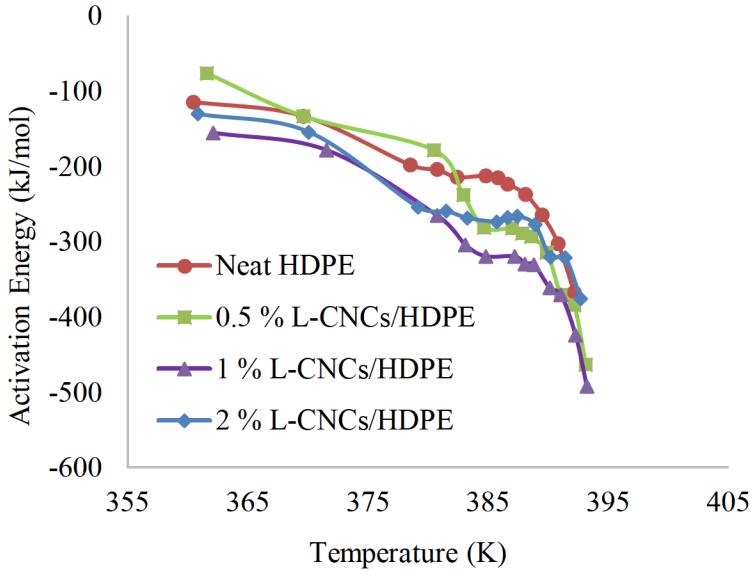

Figure 68. Dependence of the effective activation energy on average temperature (K).

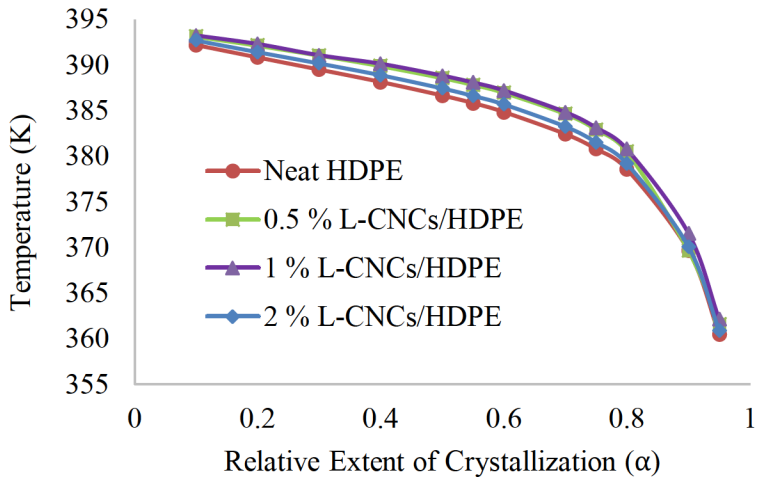

Figure 69. The variation of the average temperature with the relative extent of crystallization.

4.8 Thermogravimetric Analysis (TGA) of HDPE Nanocomposites

4.8.1 Thermal Degradation of Neat HDPE and L-CNCs/HDPE Nanocomposites

The thermal stability of neat HDPE and L-CNCs/HDPE nanocomposites were tested by TGA, and their TGA curves in N_2 atmosphere are shown in Figure 70. Neat HDPE shows a one-step decomposition process, while two stages were noticed for the L-CNCs/HDPE nanocomposites, as summarized in Table 19. With increasing L-CNC loading, the initial onset temperature of L-CNCs/HDPE nanocomposite decreases. At the initial stage of the degradation, before 400 °C, the L-CNCs/HDPE nanocomposites degrade faster than neat HDPE; however, temperatures higher than 400 °C showed L-CNCs/HDPE nanocomposites being more stable than neat HDPE. The addition of L-CNCs in HDPE influenced thermal stability. The maximum decomposition temperature for neat HDPE was seen at 489 °C, while those of L-CNCs/HDPE nanocomposites were

determined to be from 490 to 495 °C. It can be inferred from these results that L-CNCs/HDPE nanocomposites had higher thermal stability than neat HDPE.

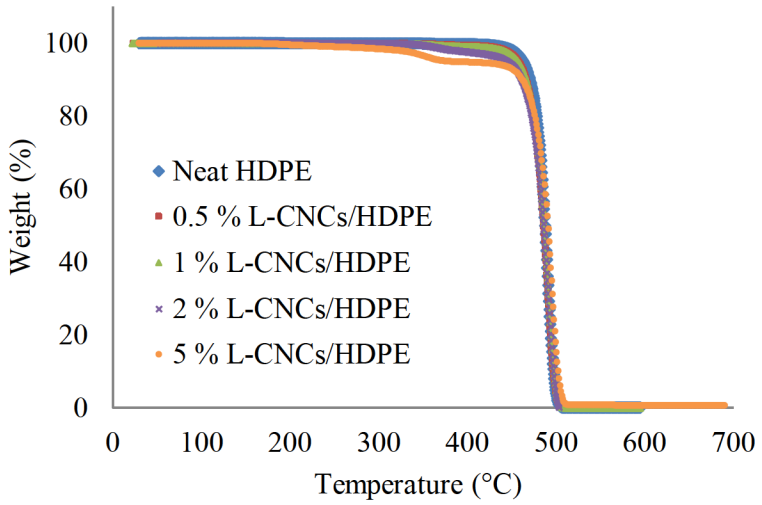

Figure 70. TGA curves of neat HDPE and L-CNCs/HDPE nanocomposites heated at 10 °C/min.

Table 19. Thermal Decomposition Parameters for Neat HDPE and L-CNCs/HDPE Nanocomposites.

Sample Designation	1st Onset T_d (°C)	2nd Onset T_d (°C)	DTG (°C)
neat HDPE	-	472.8	489.4
0.5% L-CNCs/HDPE	400.0	474.4	490.8
1% L-CNCs/HDPE	347.3	474.6	491.3
2% L-CNCs/HDPE	339.4	473.4	492.3
5% L-CNCs/HDPE	329.3	480.0	495.6

4.8.2 Thermal Degradation of L-CNCs/*f*HDPE Nanocomposites

Figure 71 presents the TGA curves of neat HDPE and L-CNCs/*f*HDPE nanocomposites. There is a one-step decomposition process seen for neat HDPE, while two stages were noticed in the L-CNCs/*f*HDPE nanocomposites. In the first stage, the L-CNCs decomposition occurred from 316 to 368 °C, as shown in Table 20. The second step depolymerization and breakdown of the HDPE chain took place at or above 472 °C. The incorporation of L-CNCs in functionalized HDPE influenced thermal stability. The maximum decomposition temperature for neat HDPE was seen at 489 °C, while those of L-CNCs/*f*HDPE nanocomposites were determined to be from 488 to 495 °C. It can be concluded from these results that L-CNCs/*f*HDPE nanocomposites had higher thermal stability than neat HDPE. Ozmen et al. reported that chemical functionalized wood flour/fiber fillers in HDPE increased thermal stability of the composites.[164]

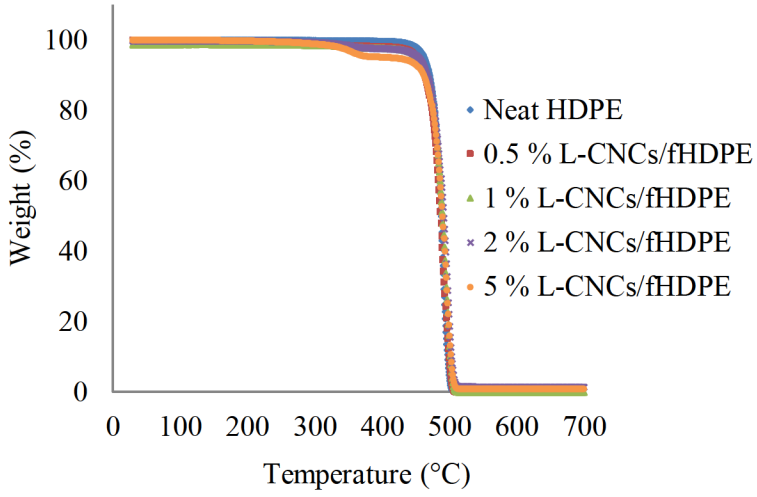

Figure 71. TGA curves of neat HDPE and L-CNCs/*f*HDPE nanocomposites heated at 10 °C/min under N_2.

Table 20. Thermal Decomposition Parameters for Neat HDPE and L-CNCs/*f*HDPE Nanocomposites.

Sample Designation	1st Onset T_d (°C)	2nd Onset T_d (°C)	DTG (°C)
neat HDPE	-	472.8	489.4
0.5 % L-CNCs/*f*HDPE	368.4	474.7	488.4
1 % L-CNCs/*f*HDPE	317.6	475.9	495.2
2 % L-CNCs/*f*HDPE	316.0	474.9	496.4
5 % L-CNCs/*f*HDPE	316.0	478.1	495.2

4.9 Mechanical Properties: Tensile Testing of HDPE Nanocomposites

4.9.1 Mechanical Properties of Neat HDPE and L-CNCs/HDPE Nanocomposites

The typical stress-strain curve shows the effect of L-CNCs on HDPE mechanical properties, as shown in Figure 72. The Young's modulus, ultimate tensile strength, tensile strength at break, and elongation at break have been determined from the stress-strain curves in Figures 73, 74, 75, and 76, respectively.. All tensile data were tabulated in Table 21. It is noted that Young's modulus increased 87% upon the incorporation of 2 wt.% L-CNCs in HDPE, almost twice the improvement that was observed for the incorporation of UHMWPE, as referenced in Chapter 3 section 3.5. The reason for this phenomenon is that the cellulosic materials exhibit a higher modulus of elasticity as compared to the polymer matrix and good interaction between the filler and matrix.[165] The ultimate tensile strength and tensile strength at break of the resultant nanocomposite properties had little to no effect with the addition of L-CNCs. These observations are in accordance with previous studies.[154, 165-166]

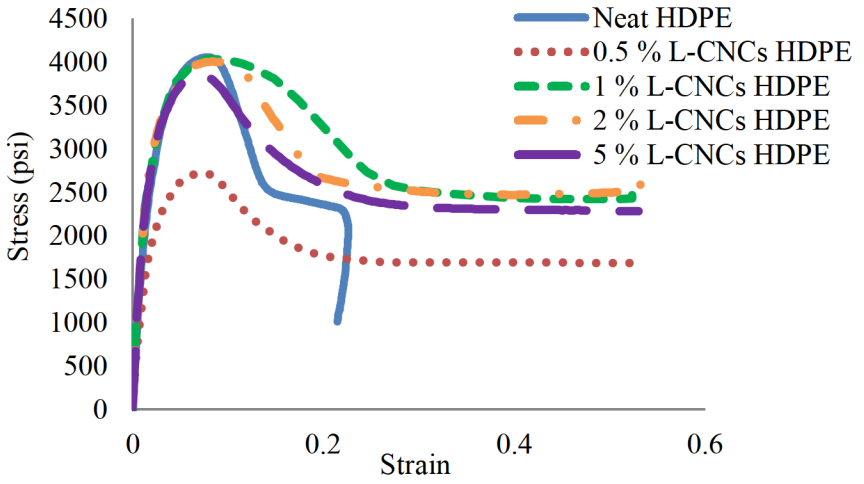

Figure 72. Representative stress-strain curves at a strain rate of (2 in/min) for neat HDPE and L-CNCs/HDPE nanocomposites.

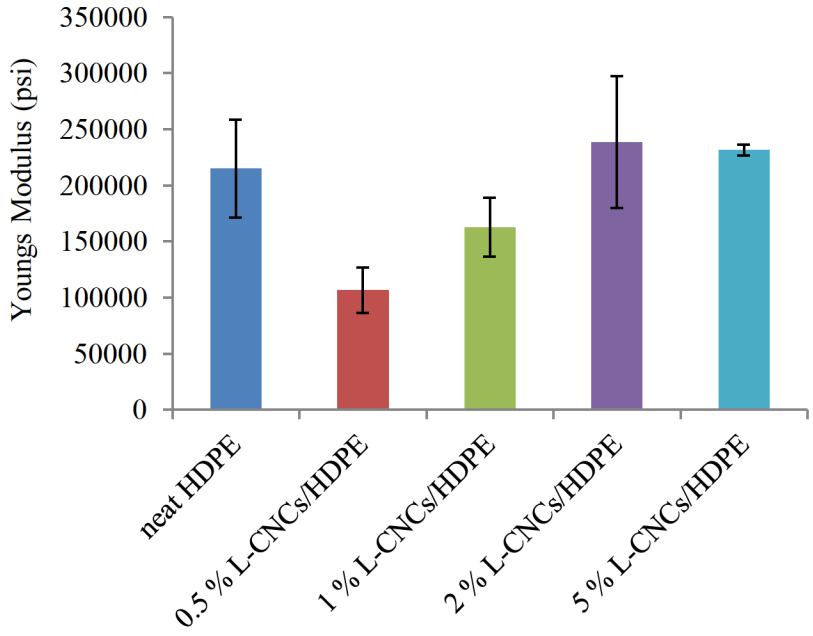

Figure 73. Young's modulus of neat HDPE and L-CNCs/HDPE nanocomposites as a function of L-CNC loading.

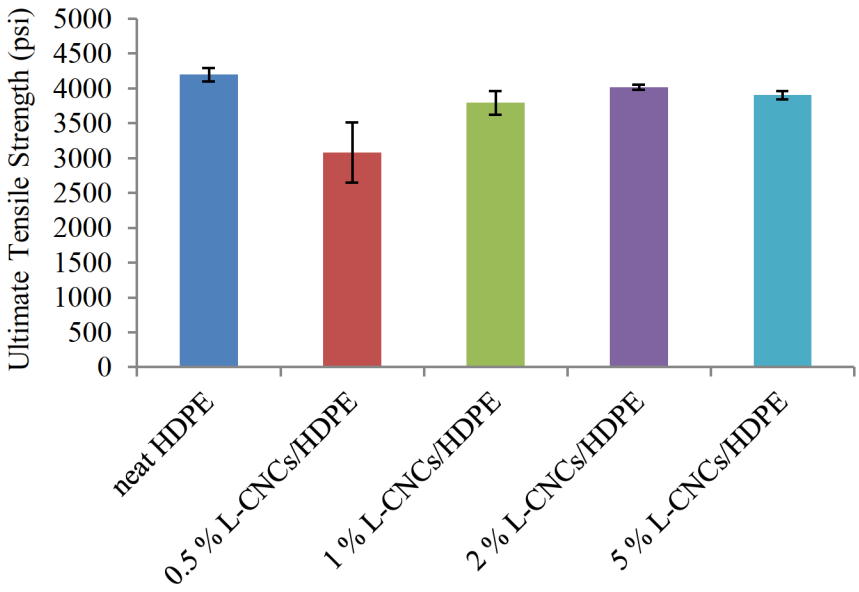

Figure 74. Ultimate tensile strength of neat HDPE and L-CNCs/HDPE nanocomposites as a function of L-CNC loading.

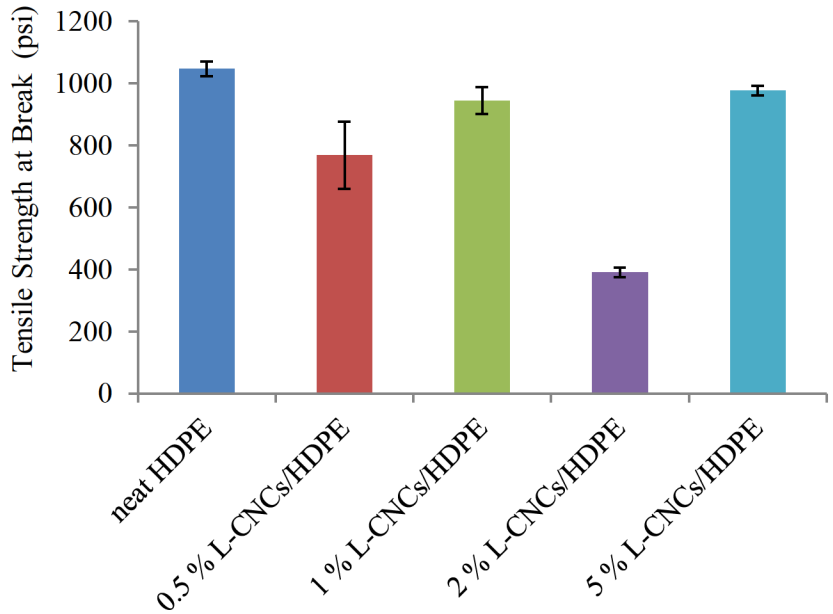

Figure 75. Tensile strength at break of neat HDPE and L-CNCs/HDPE nanocomposites as a function of L-CNC loading.

The elongation at break versus L-CNC loading of the HDPE nanocomposites shows improvement with the addition of 0.5 and 1 wt.% loading of L-CNCs, as shown in Figure 76. This behavior is a result of the improved interactions between HDPE and L-CNCs. At L-CNC loadings above 2 wt.%, there is a slight decrease in elongation at break. According to Ardhyananta et al., the decrease in elongation at break values is due to the formation of micro fillers and poor interaction between matrix and filler.[167] Therefore, the polymer will lose its plastic properties due to the increased stiffness value. This stands true for 2 and 5% L-CNCs/HDPE nanocomposites, but 0.5 and 1% L-CNCs/HDPE nanocomposites exhibited a decrease in stiffness and a dramatic increase in elongation at break as shown in Table 21.

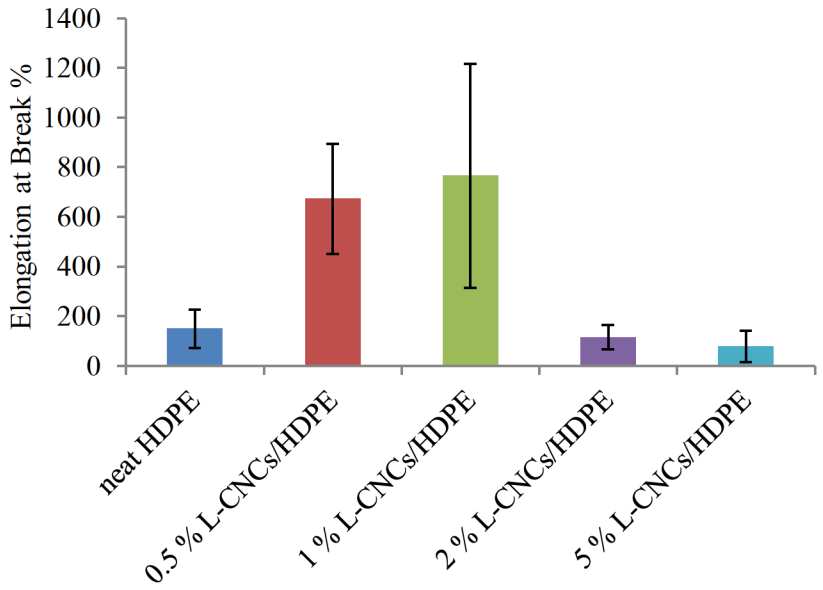

Figure 76. Elongation at break percentage of neat HDPE and L-CNCs/HDPE nanocomposites as a function of L-CNC loading.

Table 21. Results Obtained from Stress-Strain Curves of Neat HDPE and L-CNCs/HDPE Nanocomposites.

Sample Designation	Young's Modulus (psi)	Ultimate Tensile Strength (psi)	Tensile Strength at Break (psi)	Elongation at Break (psi)
neat HDPE	214992 ± 43808	4192 ± 96	1047 ± 24	149± 78
0.5% L-CNCs/HDPE	106437 ± 20099	3078 ± 431	769 ± 108	527 ± 343
1% L-CNCs/HDPE	162658 ± 26054	3792 ± 167	944 ± 43	765 ± 451
2% L-CNCs/HDPE	238536 ± 58656	4017 ± 41	391 ± 16	115 ± 48
5% L-CNCs/HDPE	231425 ± 4646	3904 ± 61	976 ± 16	78 ± 64

4.9.2 Mechanical Properties of L-CNCs/*f*HDPE Nanocomposites

Tensile testing was used to examine the tensile properties of the HDPE nanocomposite materials. The stress-strain behavior of the functionalized HDPE with the addition of L-CNCs is represented in Figure 77. The Young's modulus, tensile strength, tensile strength at break, and elongation at break data are shown in Figures 78, 79, 80, and 81, respectively. All tensile data are as summarized in Table 22. A general increase in the mechanical properties of the nanocomposites containing HDPE-g-MA was observed when compared with neat HDPE, which contains no compatibilizer or filler. This shows that the presence of MA has increased the interfacial attraction between the HDPE and L-CNCs. CNC fillers are hydrophilic, and the HDPE polymer matrix is hydrophobic which leads to challenges when trying to disperse the filler throughout the polymer.[168-169] HDPE nanocomposites with no compatibilizers can contain large agglomerates of nanocellulose because of a lack of polymer-filler interaction.[169] The strength of these nanocellulose composites is dependent on the ability of the polymer to

transfer the stress from the polymer matrix to the load-bearing nanofillers. Poor adhesion and dispersion limit the ability of the polymer to transfer this stress.[50] The presence of MA increases the interaction between HDPE and nanocellulose, resulting in better dispersion of the filler and better adhesion between the L-CNCs and HDPE. The presence of MA leads to the formation of covalent bonds between the MA and CNC-OH groups resulting in better dispersion of the nanocellulose.[49]

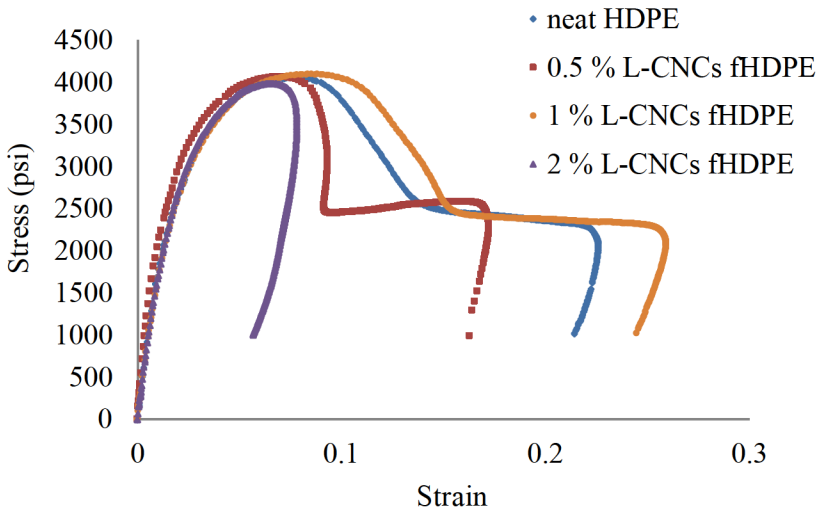

Figure 77. Representative stress-strain curves at a strain rate of (2 in/min) for neat HDPE and L-CNCs/*f*HDPE nanocomposites.

The improvement of Young's modulus properties of the resultant L-CNCs/*f*HDPE nanocomposites was mainly related to functionalizing HDPE with maleic anhydride. It also indicates the best dispersion of L-CNCs due to the small particle size with a large surface area at low loadings of 0.5-2 wt.%. The addition of 1 wt.% of L-CNCs showed an increase in ultimate tensile strength, Young's modulus, and elongation at break

properties, as summarized in Table 22. According to Uhl et al., the filler reduced the molecular mobility of polymer chains resulting in a less flexible material with a high Young's modulus.[170] The reinforcing ability of the fillers was dependent on the covalent bonding between L-CNCs and HDPE, surface characteristics, and particle size of the fillers. These results are comparable to those published by Lu et al.[50]

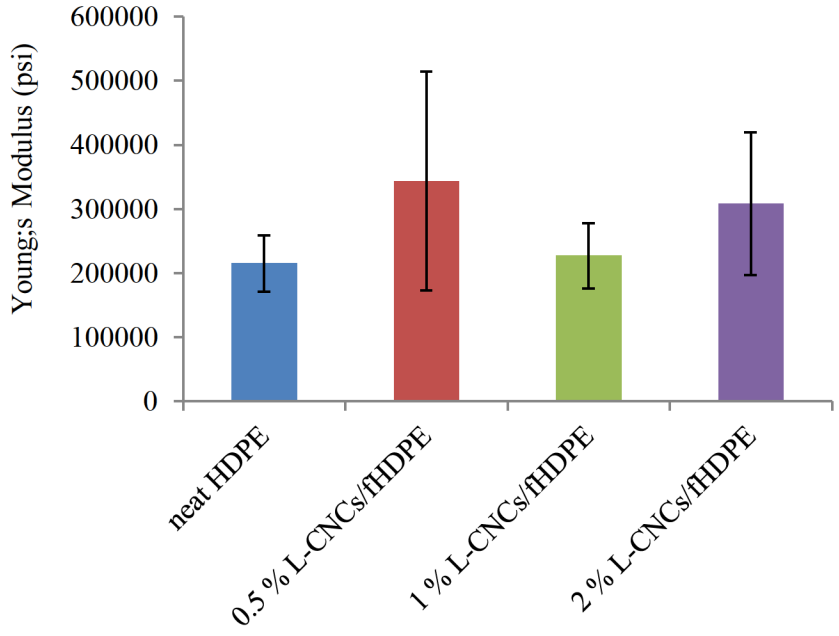

Figure 78. Young's modulus of neat HDPE and L-CNCs/*f*HDPE nanocomposites as a function of L-CNC loading.

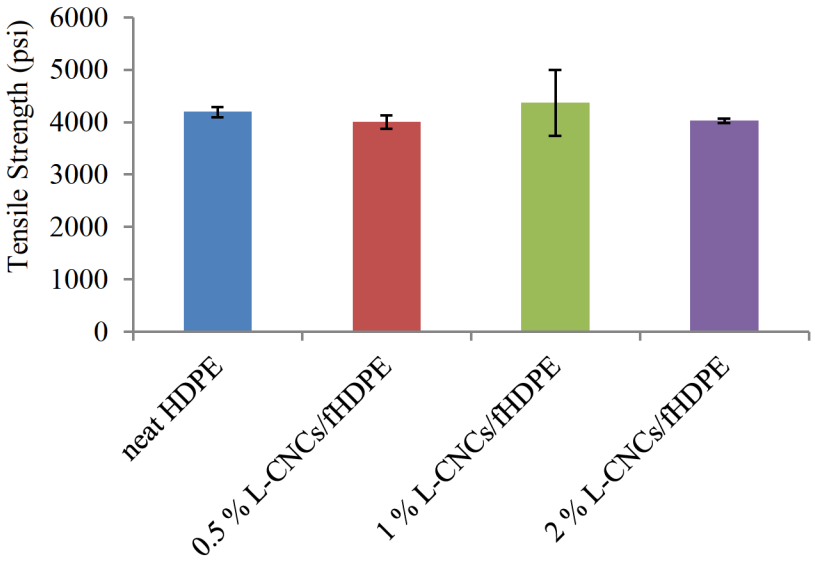

Figure 79. Tensile strength of neat HDPE and L-CNCs/*f*HDPE nanocomposites as a function of L-CNC loading.

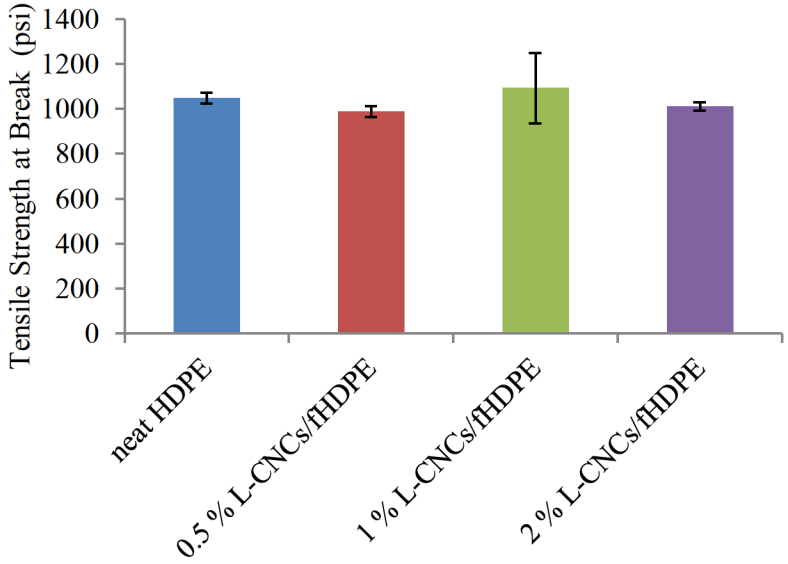

Figure 80. Tensile strength at break of neat HDPE and L-CNCs/*f*HDPE nanocomposites as a function of L-CNC loading.

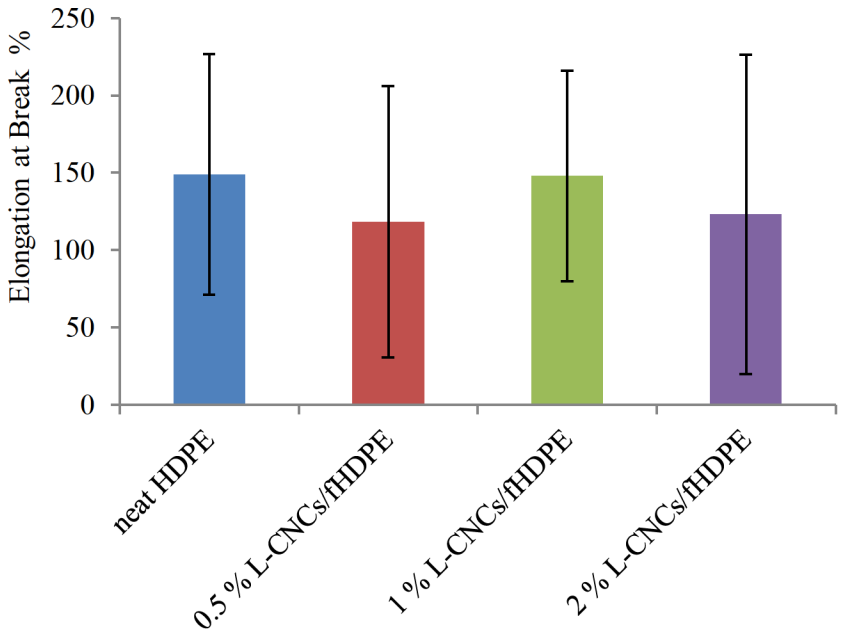

Figure 81. Elongation at break percentage of neat HDPE and L-CNCs/*f*HDPE nanocomposites as a function of L-CNC loading.

Table 22. Results Obtained from Stress-Strain Curves of Neat HDPE and L-CNCs/*f*HDPE Nanocomposites.

Sample Designation	Young's Modulus (psi)	Tensile Strength (psi)	Elongation at Break (psi)
neat HDPE	214992 ±43808	4192 ±96	149 ±78
0.5% L-CNCs/*f*HDPE	343307 ±170752	4000 ±124	118 ±88
1% L-CNCs/ *f*HDPE	226982 ±51064	4371 ±629	148 ±68
2% L-CNCs/ *f*HDPE	308192 ±111631	4020 ±42	123 ±102

4.10 Optical Microscopy of HDPE Nanocomposites

In order to study the dispersion of L-CNCs throughout the HDPE matrix at a small and large scale, the optical micrographs of 0.5 and 5 wt.% of L-CNCs in HDPE and *f*HDPE were selected and studied using optical microscopy. The technique used for studying the dispersion was based on the conventional melt-pressing method.

4.10.1 Optical Microscopy of Neat HDPE and L-CNCs/HDPE Nanocomposites

The optical results for 0.5 and 5% L-CNCs/HDPE nanocomposites are shown in Figure 82. The L-CNCs are randomly dispersed in HDPE in these images. The optical micrographs show the agglomeration of L-CNCs in clusters in HDPE. These L-CNC aggregates are observed as dark spots with a broad particle size distribution. At 0.5 wt.%, the L-CNCs aggregates are in low magnitude and well dispersed, while at 5 wt.% larger aggregates are formed. This is due to the tendency of L-CNCs to interact through weak van der Wal's forces or hydrogen bonding creating agglomerates.

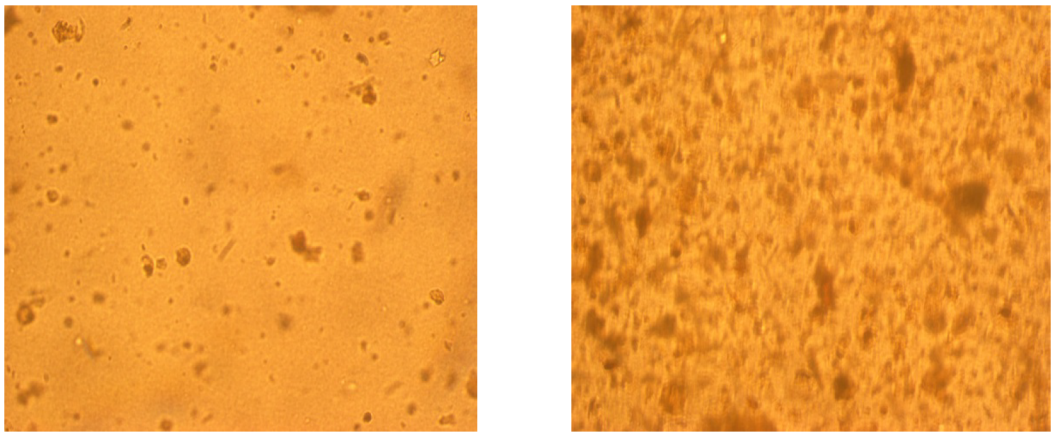

(a) (b)

Figure 82. Optical micrographs of (a) 0.5% L-CNCs/HDPE and (b) 5% L-CNCs/HDPE nanocomposites.

4.10.2 Optical Microscopy of L-CNCs/*f*HDPE Nanocomposites

Figure 83 shows the optical micrographs for 0.5 and 5% L-CNCs/*f*HDPE nanocomposites. The L-CNC particles are randomly dispersed in functionalized HDPE in these images. The addition of 0.5 wt.% L-CNCs is better dispersed in *f*HDPE than 5 wt.%. At a high loading of 5 wt.%, agglomerates of L-CNCs can be seen clearly in the optical micrographs. This is due to the tendency of L-CNCs to interact through covalent and hydrogen bonding.

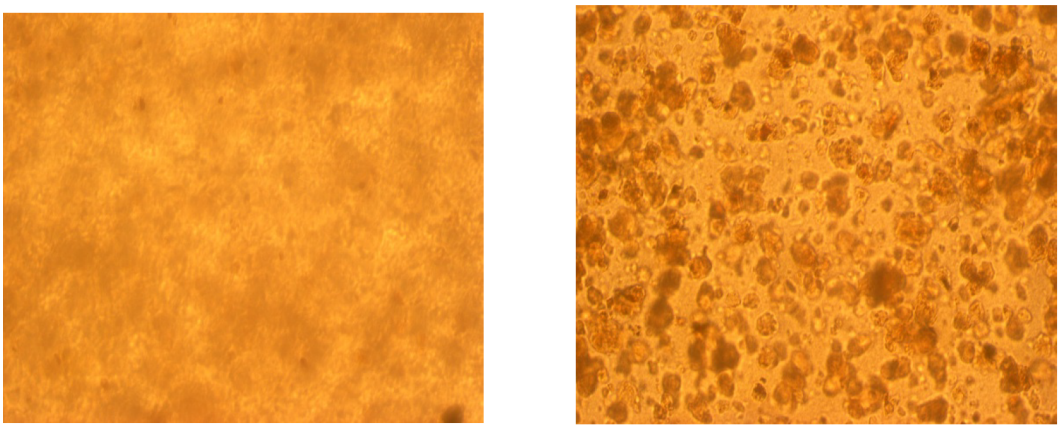

(a) (b)

Figure 83. Optical micrographs of (a) 0.5% L-CNCs/*f*HDPE and (b) 5% L-CNCs/*f*HDPE nanocomposites.

4.11 Conclusion

The reinforcement of HDPE with L-CNCs was prepared by high-torque melt-mixing. At low-loadings, the melt and crystallization temperatures were reduced, and the degree of crystallinity was increased. For analysis of the crystallization kinetics data, the Avrami and Isoconversional theories were successful in describing the non-isothermal crystallization process. The addition of L-CNCs in HDPE accelerated the crystallization

process but negatively impacted the degree of crystallinity. Isoconversional studies showed that the effective activation energy for the crystallization of the L-CNCs/HDPE nanocomposites decreased as compared to neat HDPE, which indicates that the L-CNCs act as nucleating agents. The thermal stability of the L-CNCs/HDPE nanocomposites is improved with increased loading of L-CNCs. The onset temperature of thermal degradation reflected this and maximum degradation increased with the incorporation of L-CNCs in HDPE. L-CNCs significantly improved Young's modulus of HDPE by ~87 % on addition of 2 wt.% and enhanced the elongation at break on the addition of 0.5 and 1 wt.%. The ultimate tensile strength and tensile strength at break are unaffected in the presence of L-CNCs. The significant enhancement in Young's modulus shows that lignin-coating improved the dispersion of CNCs by preventing the re-aggregation of CNCs in hydrophobic HDPE. However, all these improvements are dependent on the amount of L-CNCs added in the polymer matrix. At high-loadings of L-CNCs, the storage and loss modulus values were increased, which indicated the nanocomposites exhibited high-stiffness and energy absorption properties as compared to neat HDPE. The improvement in the L-CNCs/HDPE nanocomposites DMA properties was attributed to the fact that incorporation of L-CNCs in HDPE provides mechanical restraints which obstruct the crystallization process, thus, decreasing the crystallinity of HDPE.

One of the advantages of CNCs as a reinforcement agent is their large surface area, which can induce better interfacial interactions with the polymeric matrix, which is an important factor for enhanced nanocomposite properties. However, CNCs tend to aggregate into bundles, and hence they are difficult to be dispersed homogeneously in

hydrophobic polymer matrices. For this reason, mechanical properties are reduced at specific CNC loadings.

Functionalization of HDPE by grafting MA on HDPE with the addition of L-CNCs resulted in improved interfacial interactions between the filler and matrix and better dispersion and distribution of L-CNCs in HDPE. For functionalized HDPE, the optimum L-CNC loading to enhance Young's modulus, ultimate tensile strength, and tensile strength at break were achieved at 1 wt.%. The improvement in these properties was due to the functionalization of HDPE with MA, which improved interfacial interactions between the filler and polymer matrix. DMA properties corresponding to the storage modulus, loss modulus, and tan δ values for L-CNCs/*f*HDPE nanocomposites were not improved on the addition of L-CNCs in *f*HPDE. This may be due to the degradation of the coupling agent to some extent in dynamic loading conditions. However, the addition of 2 wt.% L-CNCs behaved similarly to neat HDPE for dynamic mechanical analysis. The crystallization behaviors of L-CNCs/*f*HDPE nanocomposites were not affected as related to neat HDPE. The thermal stability of the L-CNCs/*f*HDPE nanocomposites was improved with increased loadings of L-CNCs. In conclusion, the dispersion and distribution properties of the L-CNCs in HDPE were enhanced and led to further property improvement of the nanocomposite materials.

CHAPTER 5

POLYPROPYLENE (PP) NANOCOMPOSITES RESULTS & DISCUSSION

5.1 General Overview

Polypropylene (PP) is one of the most important semicrystalline thermoplastic materials due to its exceptional chemical resistance and mechanical strength, such as high-stiffness.[55-56] Cellulose nanocrystals (CNCs) have gained particular interest among bio-derived nanofillers due to their excellent mechanical properties such as high-stiffness and high surface area, biodegradability, low cost, and potential environmentally-friendly alternative to conventional reinforcements such as glass fiber, silicates, and carbon fiber.[19-20] CNCs have been used as an effective reinforcing agent in many polymer systems, including polyvinyl acetate adhesives,[171] polyurethanes,[163] polylactic acid (PLA),[43] and polyethylenes.[169] Spoljaric et al. used microcrystalline cellulose (MCC) as a reinforcing agent in PP and found that MCC can increase the storage modulus and glass transition temperature of PP at various MCC loading.[172]

In the present study, the CNCs surface was coated with lignin to establish a hydrophobic surface to better disperse in hydrophobic PP during high-torque melt-mixing. We have also investigated the incorporation of L-CNCs in PP by high torque melt-mixing with in situ free radical reactions with maleic anhydride, MA, and a free radical catalyst, dicumyl peroxide, DCP. The functionalization of PP by MA is an

effective way of increasing the polarity of PP.[49] In fact, these kinds of PP-g-MA have been widely used to improve interfacial adhesion between the phases in polymer-filler composites.[49, 72, 173] It has been reported that the incorporation of CNCs in PP tends to aggregate and form bundles due to strong Van der Waal's forces and hydrogen bonding, which makes the dispersion of CNCs in the PP polymer matrix difficult.[112, 174] Hence, in order to achieve better dispersion of CNCs in the PP matrix, PP is grafted with MA to create a hydrophilic surface to interact with the L-CNCs. The neat PP, L-CNCs/PP and lignin-coated cellulose nanocrystals/functionalized polypropylene (L-CNCs/*f*PP) nanocomposites mechanical, thermomechanical, and crystallization behavior were investigated by tensile testing, DMA, melt-rheology, DSC, and TGA. The methods of preparation of these materials are described in Chapter 2. The results obtained are analyzed and interpreted using various software analysis tools.

5.2 Melt-Processed Neat PP and PP Nanocomposites

Neat PP, L-CNCs/PP, and L-CNCs/*f*PP nanocomposites were weighed and dried for 60 minutes at 90 °C to remove water. The L-CNCs/PP nanocomposites were prepared by adding the polymer to the melt-mixer over a 3 min time span, followed by the addition of L-CNCs over 5 min and then melt-mixing continued for a total of 10 min. The MA grafted samples were prepared by initially melt-mixing the PP pellets for 3 min, followed by the addition of DCP for 30 seconds. MA was added and melt-mixed for 2 min, and then the appropriate loadings of L-CNCs were added, and melt-mixing continued for a total of 11 min. The samples changed from dry-free flowing powders to

large solid masses upon melt-mixing. After melt-mixing, the nanocomposites displayed a uniform light brown to dark brown color as L-CNC loading was increased, indicating a uniform dispersion and distribution of L-CNCs throughout the nanocomposite. The presence of the L-CNCs could be identified by the brownish color of the nanocomposite. Increased loadings of L-CNCs caused a steadily decreasing appearance of the original opaque white PP, and the nanocomposites took on the appearance of L-CNCs, as shown in Figures 84 and 85. The melt-mixed materials were broken up upon removal from the melt-mixer. Neat PP was melt mixed to compare with L-CNCs/PP nanocomposites. Following melt-mixing, all samples were characterized, as described in Chapter 2.

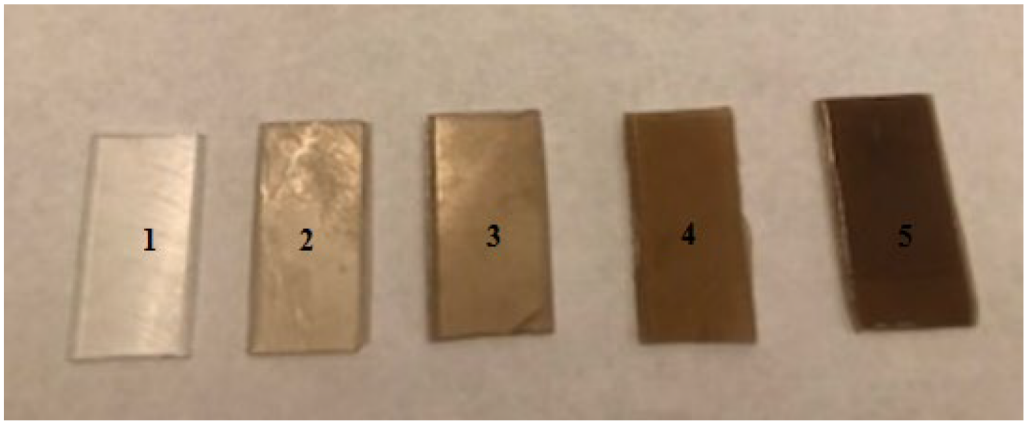

Figure 84. PP samples were designated as 1, 2, 3, 4, and 5 respectively for neat PP, 0.5% L-CNCs/PP, 1% L-CNCs/PP, 2% L-CNCs/PP, and 5% L-CNCs/*f*PP.

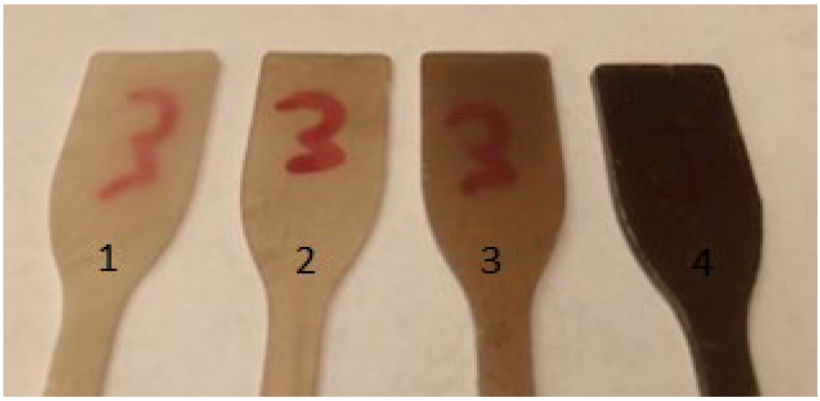

Figure 85. PP samples were designated as 1, 2, 3, and 4, respectively for 0.5% L-CNCs/*f*PP, 1% L-CNCs/*f*PP, 2% L-CNCs/*f*PP, and 5% L-CNCs/*f*PP.

5.3 Thermal Analysis of PP Nanocomposites by DSC

5.3.1 Thermal Analysis of Neat PP and L-CNCs/PP Nanocomposites

DSC analysis of neat PP and L-CNCs/PP nanocomposites was carried out to analyze the effect of L-CNC loading on the thermal characteristics of PP. Figure 86 presents the DSC scans of neat PP and L-CNCs/PP nanocomposites showing the presence of crystallization exotherm (T_c), melting endotherm (T_m) peaks and glass transition temperature (T_g). The DSC thermal characteristics are summarized in Table 23, showing the melting, crystallization and glass transition temperatures, percent crystallinity, and change in enthalpy for neat PP and L-CNCs/PP nanocomposites. From experimental ΔH_m values, percent crystallinity was calculated using equation 1, in Chapter 3, section 3.2; where, ΔH_m° is the standard enthalpy of melt for 100% crystalline PP, taken from the literature as 207 J/g.[175] The data suggest the addition of L-CNCs for the T_c, T_m and percent crystallinity remained unchanged and the thermal characteristics of these L-CNCs/PP nanocomposites are comparable to those of neat PP. These results indicate that

the L-CNCs tend to promote the agglomerate formation, which would prevent the nucleation effect of the L-CNCs particles, and as a result, the thermal characteristics remain unchanged. Similarly, Bagheriasl et al. research showed no change in the crystalline content of the PP reinforced with CNCs.[174] However, our work indicated there was an increase in the T_g values upon the addition of L-CNCs, which is due to the L-CNCs restricting chain mobility. Formation of a network of an interphase polymer may create significant increases in the nanocomposite T_g at low loadings.[176] Ramanathan et al. reported an increase in T_g values on the addition of thermally expanded graphite oxide (TEGO) in poly(acrylonitrile) (PAN), at only 0.05 wt.% loading of TEGO which was due to the hydroxyl groups present on the TEGO surfaces promoting a favorable non-covalent interaction with the polymer.[177]

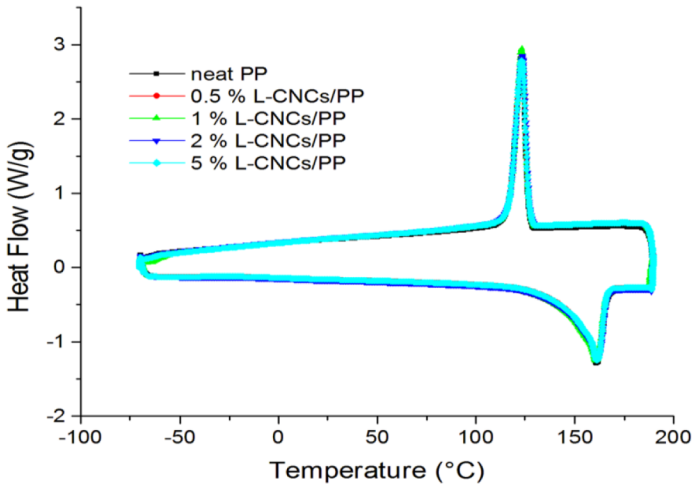

Figure 86. DSC scans for neat PP and L-CNCs/PP nanocomposites at 10 °C/min.

Table 23. DSC Thermal Parameters of Neat PP and L-CNCs/PP Nanocomposites Derived from Cooling and Second Heating Scans at 10 °C/min.

Sample designation	X_c (%)	T_m (°C)$_{onset}$	T_c (°C)$_{onset}$	ΔH_m (J/g)	T_g (°C)$_{mid}$
neat PP	47.4%	150.4	126.9	98.1	-42.4
0.5% L-CNCs/PP	48.4%	149.6	126.6	99.7	-34.6
1% L-CNCs/PP	48.7%	150.6	127.0	99.8	-32.7
2% L-CNCs/PP	48.4%	151.0	126.9	98.1	-35.9
5% L-CNCs/PP	48.0%	150.7	126.6	94.3	-34.7

5.3.2 Thermal Analysis of L-CNCs/*f*PP Nanocomposites

Figure 87 presents the DSC cooling and second heating scans at 10 °C/min for neat PP and L-CNCs/*f*PP nanocomposites. The DSC scans show the presence of crystallization exotherm, T_c, melting endotherm, T_m, peaks, and glass transition, T_g. The typical DSC parameters corresponding to melt, crystallization and glass transition temperatures, change in enthalpy, and percent crystallinity are given in Table 24. From the experimental ΔH_m values, percent crystallinity was calculated using equation 1, in Chapter 3, section 3.2; where, ΔH_m° is the standard enthalpy of melt for 100% crystalline PP, taken from the literature as 207 J/g.[175] The addition of L-CNCs in *f*PP show an increase in enthalpy of melting from 106.1 to 114.1 J/g which is correlated to the increase in percent crystallinity from 51.8 to 63.6% as compared to neat PP. The melting temperatures of the PP nanocomposites are slightly increased and the onset of crystallization temperatures decrease which is indicative of the L-CNCs acting as

nucleating agents in functionalized PP. The improved interfacial interaction between L-CNCs and PP is attributed to the functionalization PP with MA.[49] An increase in T_g values was observed on the addition of L-CNCs for all nanocomposites. Similarly, Salavagione et al. reported an increase in T_g values due to the incorporation of graphene oxide (GO) in grafted poly (vinyl alcohol) (PVA) via esterification.[178] We suggest that there is a strong interfacial interaction between PP and L-CNCs, which inhibits the molecular motion and viscous flow of the polymer chains, resulting in an increase in the T_g. These observations could be ascribed to the efficiency of MA as a compatibilizer that favored a better dispersion and wetting of L-CNCs within the hydrophobic PP.

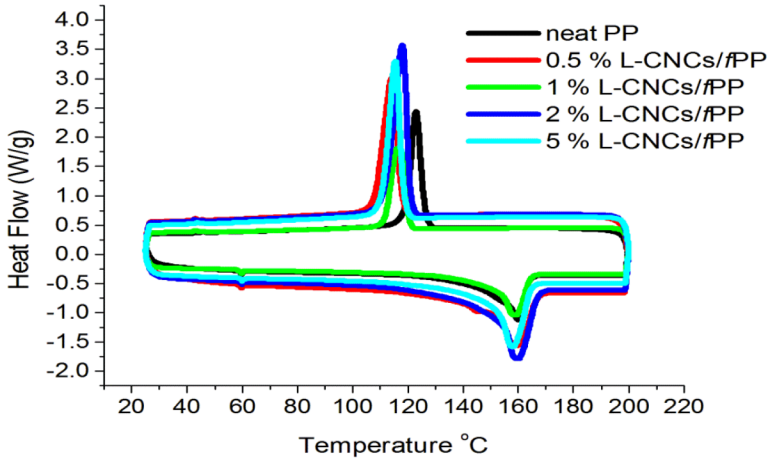

Figure 87. DSC scans for neat PP and L-CNCs/*f*PP nanocomposites at 10 °C/min.

Table 24. DSC Thermal Parameters of Neat PP and L-CNCs/*f*PP Nanocomposites Derived from Cooling and Second Heating Scans at 10 °C/min.

Sample designation	X_c (%)	T_m (°C)$_{onset}$	T_c (°C)$_{onset}$	ΔH_m (J/g)	T_g (°C)$_{mid}$
neat PP	47.4%	150.4	126.9	98.1	-42.4
0.5% L-CNCs/*f*PP	51.8%	149.4	119.7	106.7	-35.5
1% L-CNCs/*f*PP	30.7%	152.4	120.3	63.0	-36.7
2% L-CNCs/*f*PP	63.6%	152.8	121.2	129.1	-36.7
5% L-CNCs/*f*PP	58.0%	151.6	121.4	114.1	-37.0

5.4 Melt-Rheology Properties of PP Nanocomposites

5.4.1 Melt-Rheology Analysis of Neat PP and L-CNCs/PP Nanocomposites

Melt-rheology was used to examine the variation of G′, G″, tan δ and η* as a function of angular frequency at 175 °C for neat PP and L-CNCs/PP nanocomposites as shown in Figures 88, 89, 90, and 91, respectively. The observed storage modulus G′ and loss modulus G″ of PP decreases on the addition of L-CNCs at high frequency, which is due to the agglomeration of L-CNCs resulting in decrease stiffness. As presented in Figure 90, the tan δ values of all PP samples decrease with an increase in frequency, which is typical behavior of liquid-like material. With the addition of L-CNCs, tan δ values increased at high frequency, absorbing more energy at frequencies higher than 10 rad/s as compared to neat PP. The reduction in tan δ values are more pronounced in the low-frequency region, as the L-CNC loading is increased by 2 wt.%. Rahimi et al. reported that the tan δ values of the nanocomposites are expected to decrease due to the

presence of CNCs dispersed in the polymer matrix.[179] Furthermore, the strong interaction between PP and CNCs surface will significantly reduce the chain mobility at the interface. This is consistent with the increase in T_g of the L-CNC/PP nanocomposites. We suggest that the coating of the lignin on the CNCs surface assisted in better dispersion of the CNCs and slightly increased chain mobility.

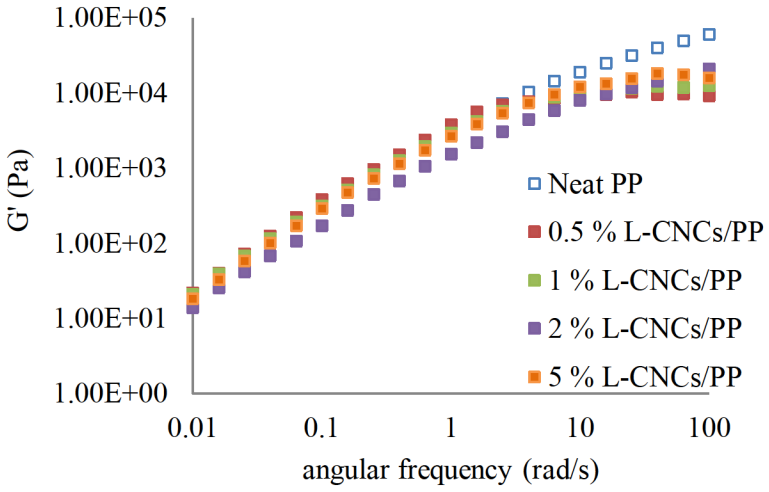

Figure 88. Storage modulus (G′) vs. angular frequency for neat PP and L-CNCs/PP nanocomposites at 175 °C.

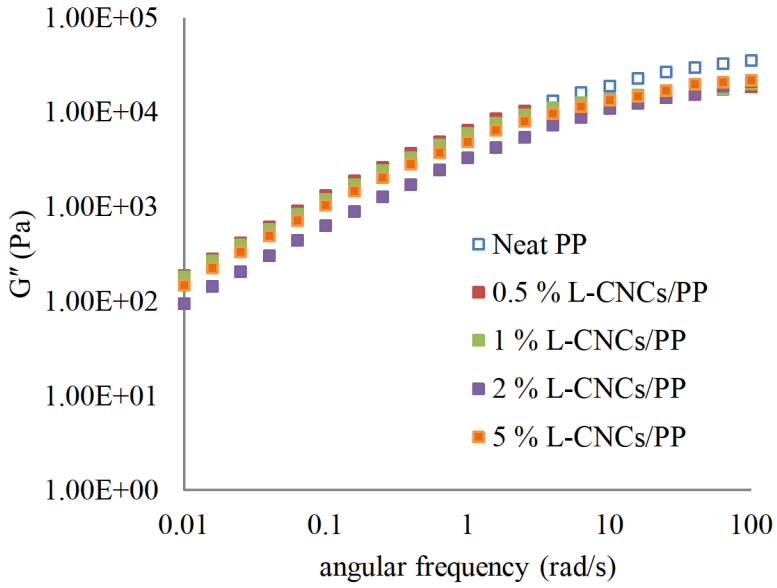

Figure 89. Loss modulus (G″) vs. angular frequency for neat PP and L-CNCs/PP nanocomposites at 175 °C.

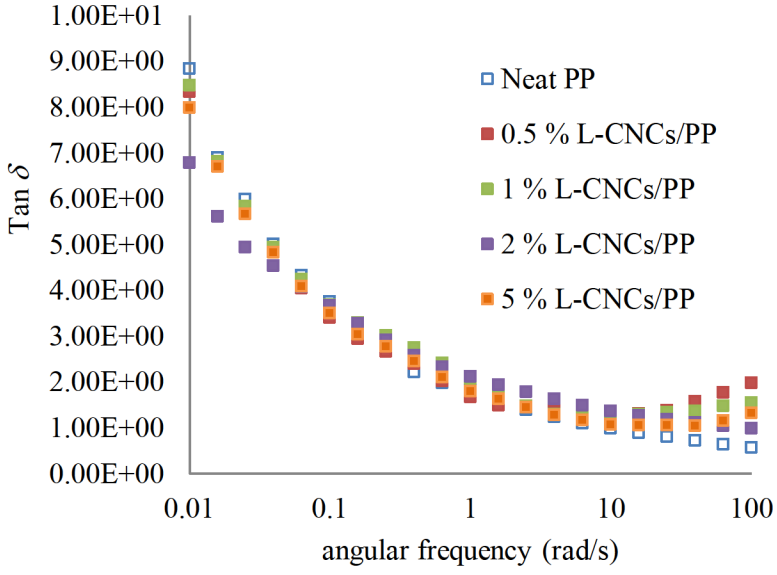

Figure 90. Tan δ vs. angular frequency for neat PP and L-CNCs/PP nanocomposites at 175 °C.

The complex viscosity curves of the neat PP and L-CNCs/PP nanocomposites are shown in Figure 91. The addition of 2 wt.% of L-CNCs in PP resulted in a decrease in complex viscosity across the frequency range. With the addition of 0.5% and 1% L-CNCs, the complex viscosity curves mimicked the behavior of neat PP up to 5 rad/s. The rheology data was further examined using Cole-Cole plots to represent the relationship between the real, η', and the imaginary, η'', parts of the complex viscosity, as shown in Figure 92. It has been reported that the plot can be used to analyze the miscibility of polymer-filler components.[180-181] If the data plotted presents a semicircular shape, this would suggest good compatibility. However, any deviation from the shape shows a non-homogeneous dispersion of L-CNCs and phase segregation due to immiscibility. It appears at 175 °C, L-CNCs are miscible or at least finely dispersed, as is evident from the semicircular shape of the plots. The addition of 0.5 wt.% of L-CNCs Cole-Cole plot was slightly higher than that of the neat PP, suggesting that a longer relaxation time appeared. The Han plot has was used to investigate order-disorder transitions in PP and the effect of polydispersity and miscibility of L-CNCs in PP, as shown in Figure 93. PP relaxation time is affected by the presence of L-CNCs due to the nanocomposites deviation at high frequency from the scaling of G' vs. G'' of linear PP, indicating that a relaxation mechanism occurred in nanocomposites.

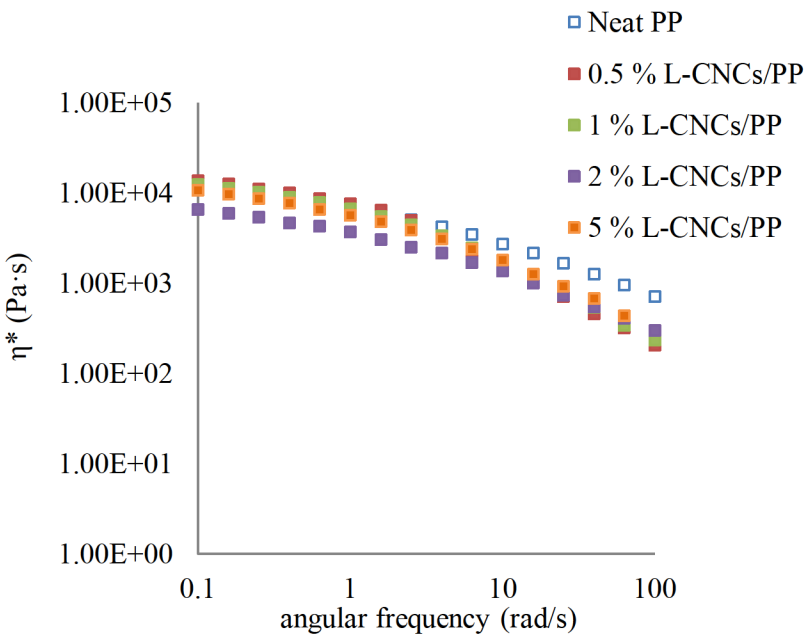

Figure 91. Complex viscosity (η*) vs. angular frequency for neat PP and L-CNCs/PP nanocomposites at 175 °C.

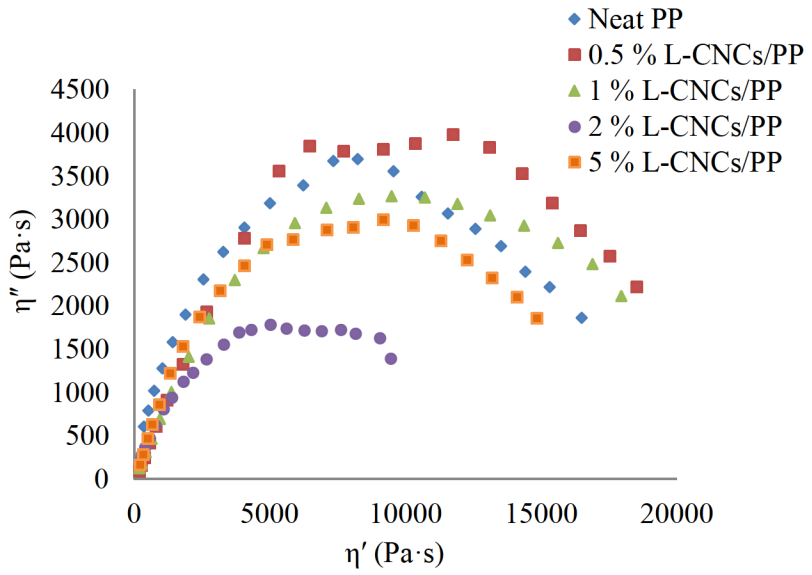

Figure 92. Imaginary viscosity (η″) vs. dynamic viscosity (η′) plots for neat PP and L-CNCs/PP nanocomposites at 175 °C.

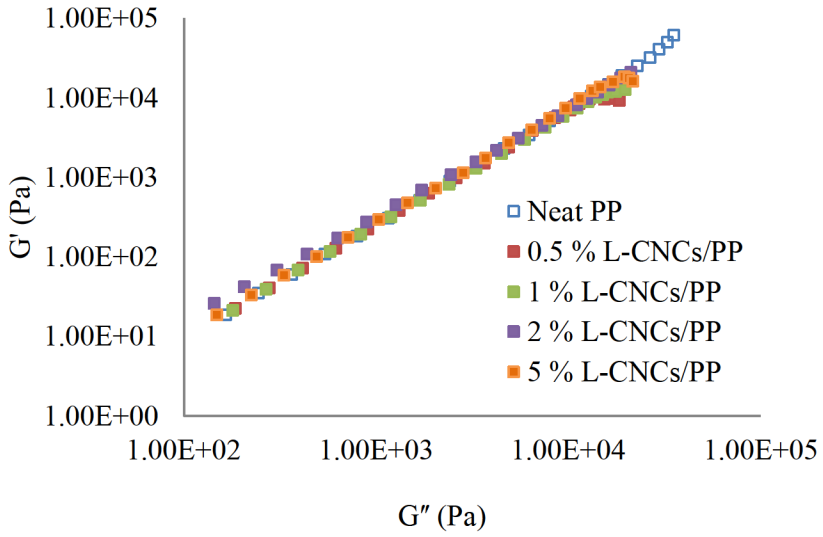

Figure 93. Storage modulus (G′) vs. loss modulus (G′) for neat PP and L-CNCs/PP nanocomposites at 175 °C.

5.4.2 Melt-Rheology Analysis of L-CNCs/*f*PP Nanocomposites

The rheological properties of L-CNCs in functionalized PP nanocomposites were studied to understand the structure-property relationship better. Figure 94 presents the storage modulus, G′, as a function of angular frequency, ω, for neat PP and L-CNCs/*f*PP nanocomposites. It is evident at low frequency; the addition of L-CNCs in *f*PP causes the G′ values to decrease. However, at high frequency, the addition of 1 and 2 wt.% of L-CNCs show higher G′ values than neat PP. This behavior is also seen in Figure 95 for loss moduli values, G″, as a function of frequency which is due to the influence of L-CNCs elastic properties in the melt. Furthermore, the obtained results in Table 25 for non-terminal and terminal slopes for G′, G″ vs. ω plots at low frequency, 0.1 – 1 rad/s, and high-frequency, 100- 628 rad/s, were calculated to interpret the rheological behavior

for neat PP and L-CNCs/*f*PP nanocomposites. As mentioned, at a fixed frequency, both G' and G" increase with the addition of 0.5 and 2 wt.% of L-CNCs. In addition, at a constant L-CNC loading, both G' and G" increase with increasing frequency. The non-terminal behavior at low frequencies for *f*PP with the addition of 0.5-5 wt.% of L-CNCs is due to strong polymer-particles and inter-particles interactions and a structural network of L-CNCs, which reduces long-range motions of polymer chains.[112] This observed increase in slope with the addition of L-CNCs can be explained by microstructural changes in the samples. The rheological data obtained are attributed to the fact that the high-frequency region is mainly governed by short-range dynamics of polymer chains and the rheological behavior of the system is dominated by the matrix properties.[112, 136] For the low-frequency region, the behavior of the nanocomposites is governed by relatively long-range interactions and the formation of L-CNC networks, instead of the relaxation of polymer matrix molecules as the CNC network resists the structural relaxation which is responsible for the observed enhanced melt elasticity as already discussed.[160]

Figure 96 presents the tan δ values as a function frequency for the neat PP and L-CNCs/*f*PP. It is observed that the addition of L-CNCs showed moderate increases in the tan δ values at low frequencies and behaved similarly to the neat PP at high frequencies. For the neat PP and L-CNCs/*f*PP nanocomposites, the plots were ascending with the frequency decreasing, which is typical terminal behavior of liquid-like material. With the addition of L-CNCs, tan δ values were rapidly reduced in the low-frequency region. At high frequency, the addition of L-CNCs in PP, tan δ values are superimposed and there

was no observed difference in the curves. The complex viscosity (η*) of the nanocomposites is also affected by the presence of L-CNCs in the functionalized polymer melt as shown in Figure 97. Generally, the addition of rigid nanofillers results in an increase in complex viscosity as a result of molecular movement and restriction forced by the nanofiller.[160] However, the results of the L-CNCs/*f*PP nanocomposites show a decrease in complex viscosity at low frequencies and at frequencies above 40 rad/s there is an increase. This effect is dependent on the state of dispersion of the L-CNC particles in the matrix.

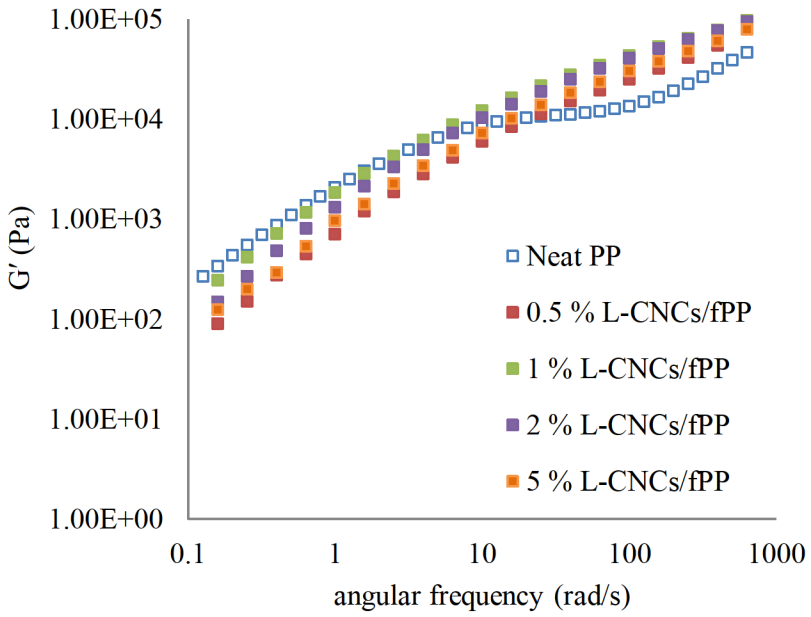

Figure 94. Storage modulus (G′) vs. angular frequency for neat PP and L-CNCs/*f*PP nanocomposites at 175 °C.

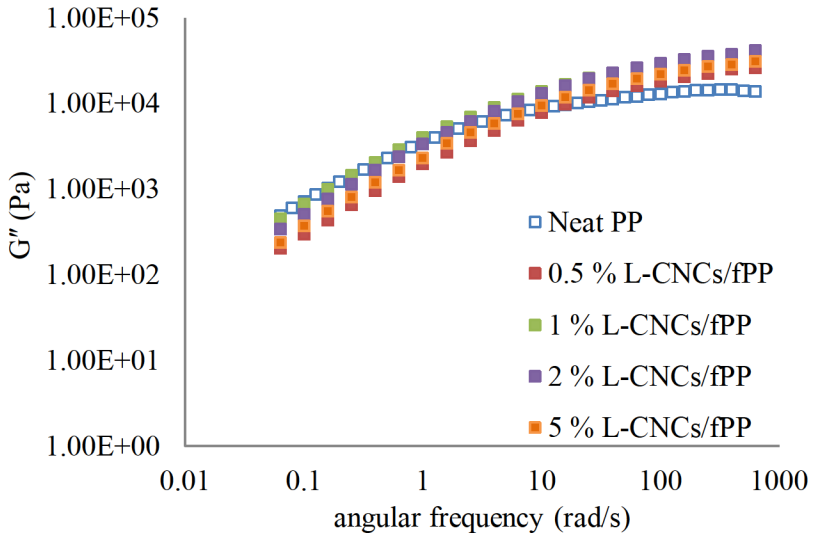

Figure 95. Loss modulus (G″) vs. angular frequency for neat PP and L-CNCs/*f*PP nanocomposites at 175 °C.

Table 25. Non-Terminal and Terminal Slopes of the Storage (G′) and Loss Moduli (G″).

Sample designation	Non-terminal Slopes		Terminal Slopes	
	G′	G″	G′	G″
neat PP	2.4581	1.6990	0.002372	0.000060
0.5% L-CNCs/*f*PP	2.6648	1.9916	0.002105	0.000646
1% L-CNCs/*f*PP	2.6896	1.8478	0.001440	0.000582
2% L-CNCs/*f*PP	2.7545	1.8574	0.001529	0.000583
5% L-CNCs/*f*PP	2.6280	1.8814	0.001748	0.000594

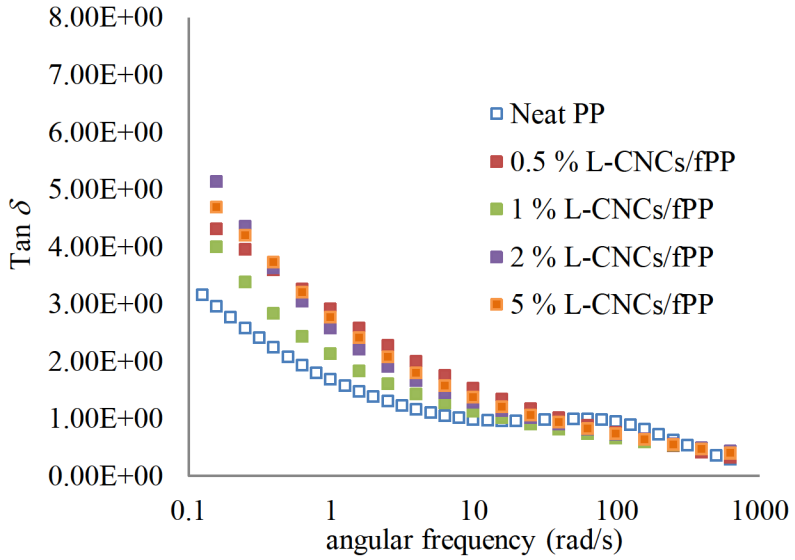

Figure 96. Tan δ vs. angular frequency for neat PP and L-CNCs/*f*PP nanocomposites at 175 °C.

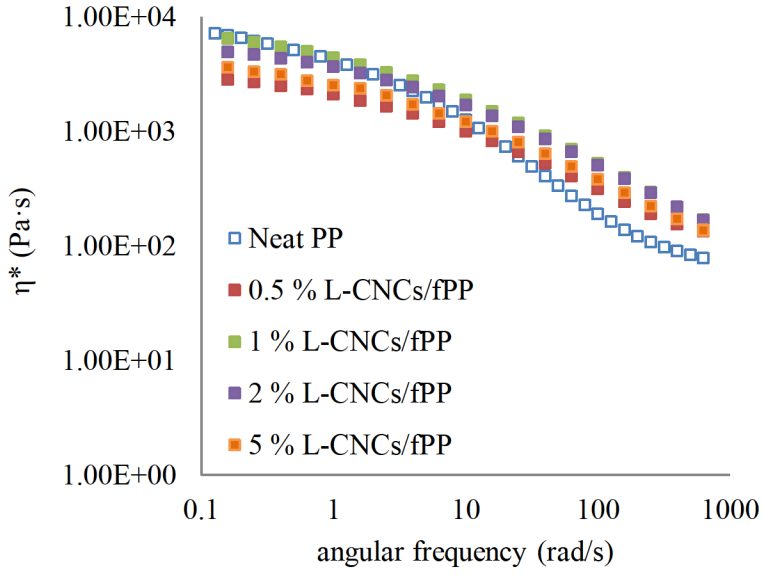

Figure 97. Complex viscosity (η*) vs. angular frequency plot for neat PP and L-CNCs/*f*PP nanocomposites at 175 °C.

For the neat PP and L-CNCs/PP nanocomposites, the Cole-Cole plots were close to a semi-circle, and the higher the molecular weight was, the bigger the radius was, as shown in Figure 98. The curves for 0.5 and 5 wt.% L-CNCs/PP nanocomposites were lower than neat PP, indicating that some degradation of the reaction took place. It is clear from the linear viscoelastic plots; a longer relaxation process appeared in the functionalized PP with the addition of L-CNCs. We suggest that this longer relaxation process is correlated to long-chain branching which resulted from the radical reactions in the presence of DCP and L-CNCs. The Han plots of functionalized PP with the addition of L-CNCs deviated considerably from the scaling G′ vs. G″ of the linear PP, indicating that an extended relaxation mechanism occurred in these nanocomposites as shown in Figure 99. These results are in accordance with the Tian et al. who attributed extended relaxation mechanisms to the grafting of long-chain branches on the PP backbone in the presence of pentaerythritol triacrylate (PETA) increasing the relaxation time.[182]

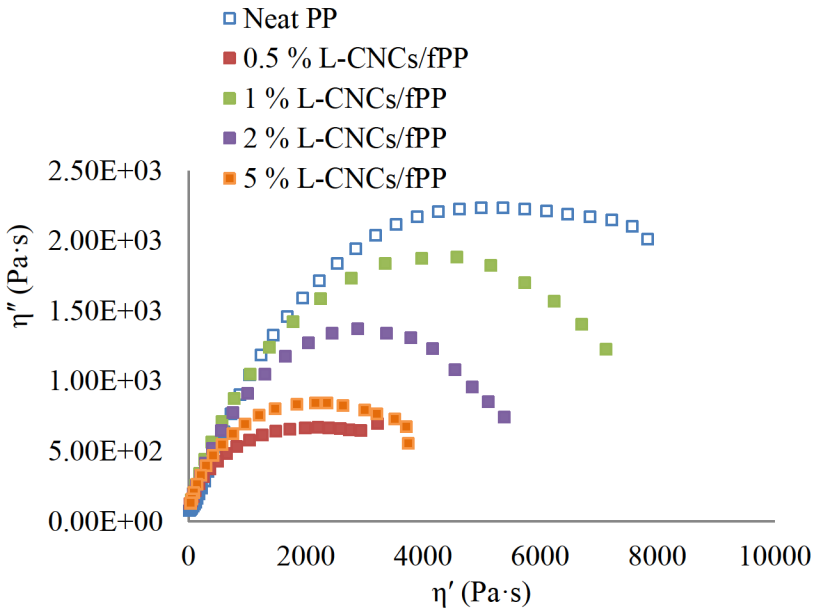

Figure 98. Imaginary viscosity (η″) vs. dynamic viscosity (η′) plot for neat PP and L-CNCs/*f*PP nanocomposites at 175 °C.

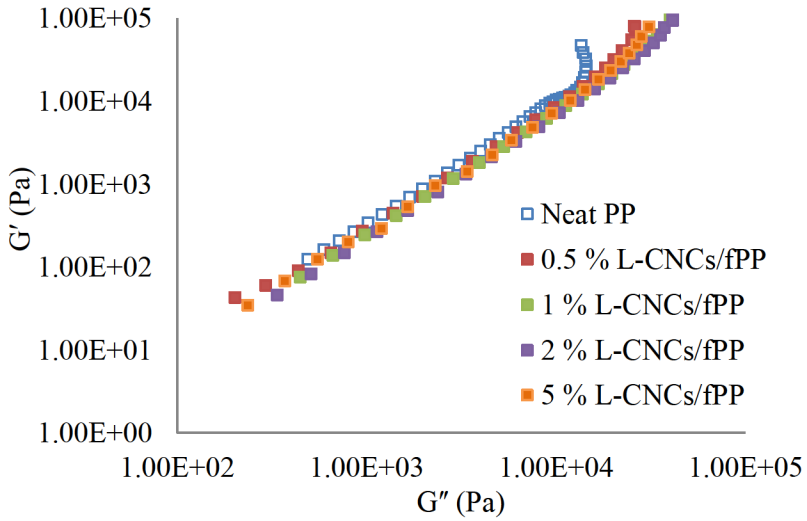

Figure 99. Storage modulus (G′) vs. loss modulus (G′) plot for neat PP and L-CNCs/*f*PP nanocomposites at 175 °C.

5.5 Viscoelastic Properties of Neat PP and L-CNCs/PP Nanocomposites by DMA

The dynamic mechanical characterization was performed on neat PP and L-CNCs/PP nanocomposites to evaluate the influence of L-CNCs on the thermomechanical properties of PP. The storage modulus plots of neat PP and PP/L-CNCs nanocomposites as a function of temperature are shown in Figure 100. It is clear from Figure 100 the storage modulus values for L-CNC/PP nanocomposites are higher than neat PP at low temperatures. The highest storage modulus values are displayed by nanocomposites with L-CNC loadings of 0.5 and 5 wt.%. Clearly, the addition of L-CNCs at low loadings increased the storage modulus of PP. The increase in modulus is due to the presence of the highly rigid L-CNCs, which improved the rigidity of PP. However, it should be noted that based on the DSC analysis, the overall percent crystallinity of the nanocomposites is not consistent with the stiffening of PP, as seen in DMA results, indicating that the L-CNCs are acting as reinforcing agents. Figure 101 presents the loss modulus, G″, values for neat PP and L-CNCs/PP nanocomposites as a function of temperature. The addition of L-CNCs increased the loss modulus values of PP from 30 to 100 °C, which is due to an increase in the interfacial interaction between L-CNCs and PP and better dispersion of L-CNCs in PP matrix. The temperature dependence of the L-CNCs/PP nanocomposites tan δ values is relative to neat PP in Figure 102. As the temperature approaches the melt-temperature for PP, we observe the α-transition and the addition of L-CNCs show higher tan δ values as compared to the neat PP.

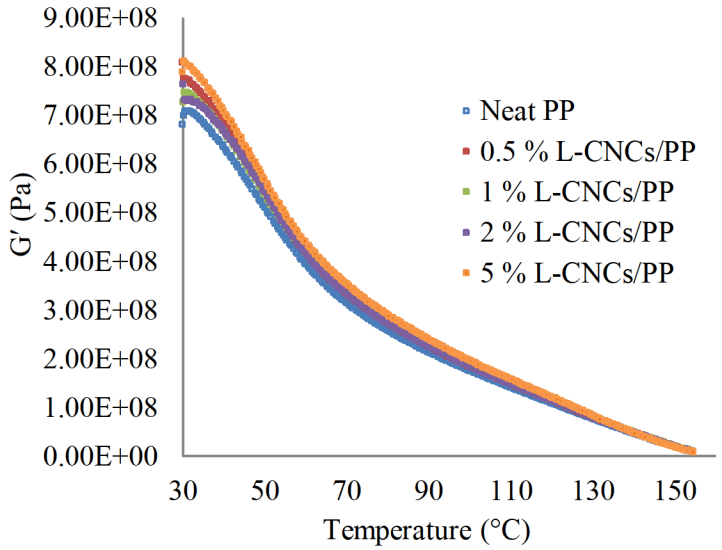

Figure 100. Storage modulus (G′) values for neat PP and L-CNCs/PP nanocomposites as a function of temperature at 3 °C/min.

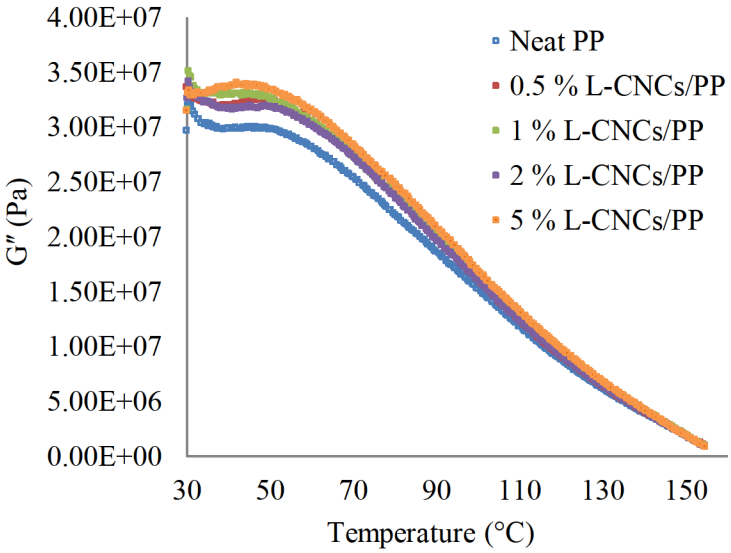

Figure 101. Loss modulus (G″) values for neat PP and L-CNCs/PP nanocomposites as a function of temperature at 3 °C/min.

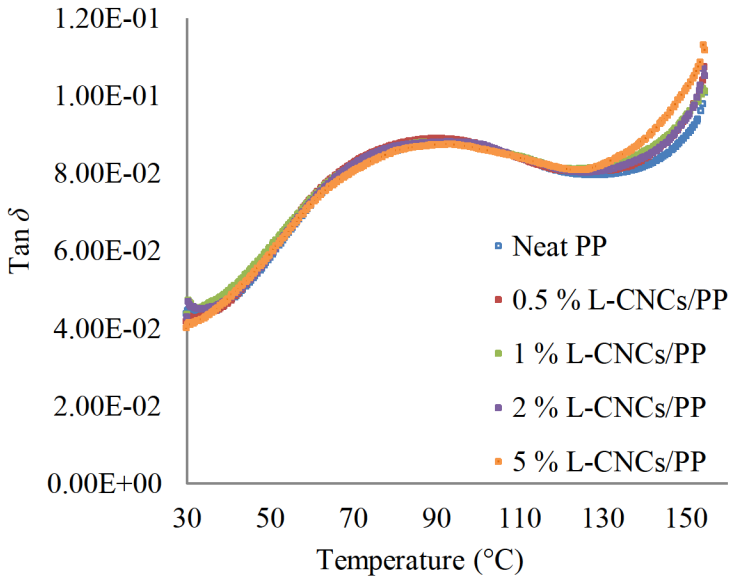

Figure 102. Tan δ values for neat PP and L-CNCs/PP nanocomposites as a function of temperature at 3 °C/min.

5.6 Thermogravimetric Analysis (TGA) of PP Nanocomposites

5.6.1 Thermal Degradation of Neat PP and L-CNCs/PP Nanocomposites

Figure 103 presents the TGA curves of neat PP and L-CNCs/PP nanocomposites at a heating rate of 20 °C/min in N_2. Table 26 summarizes the TGA data, including initial and secondary stages of decomposition temperatures, T_d, and maximum decomposition, *DTG*, for neat PP and L-CNCs/PP nanocomposites. It is clear that neat PP degrades in a single step. The step initiates at 490.3 °C and ends at 515.3 °C. In the first stage, the L-CNCs decomposition occurred from 355.9 to 371.6 °C; in the second stage, the depolymerization and breakdown of the PP chains took place at or above 490.3 °C, while the maximum decomposition rate, took place at or above 512.9 °C. The data indicates

that L-CNCs did not improve the thermal stability of PP. Similarly, Khoshkava et al. also observed a decrease in thermal stability for PP upon the addition of CNCs.[112]

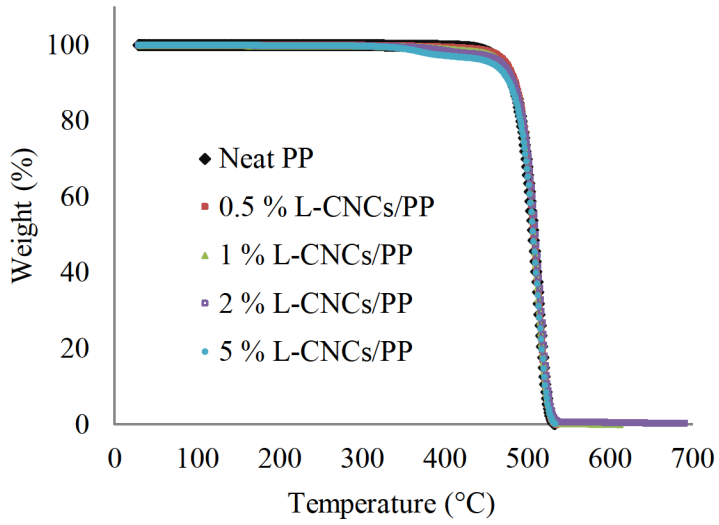

Figure 103. TGA curves of neat PP and L-CNCs/PP nanocomposites at a constant heating rate of 20 °C/min.

Table 26. TGA Data of Different Contents of Neat PP and L-CNCs/PP Nanocomposites at a Heating Rate of 20 °C/min.

Sample Designation	1st Stage T_d (°C)	2nd Stage T_d (°C)	DTG (°C)
neat PP	-	490.3	515.3
0.5% L-CNCs/PP	371.6	492.2	512.9
1% L-CNCs/PP	372.0	490.8	513.3
2% L-CNCs/PP	365.9	492.0	514.5
5% L-CNCs/PP	355.9	491.5	512.9

5.6.2 Thermal Degradation of L-CNCs/*f*PP Nanocomposites

The thermal stability of the neat PP and L-CNCs/*f*PP nanocomposites was investigated to determine the effect of the L-CNCs on functionalized PP. The TGA curves for the neat PP and L-CNCs/*f*PP nanocomposites at a constant heating rate of 20 °C/min are present in Figure 104. Figure 104 shows a predominantly single major thermal degradation peak for neat PP occurring at around 490.3 °C. The addition of L-CNCs in *f*PP nanocomposite samples showed a multi-step degradation process with the first stage of decomposition at 333.9 °C, the second stage of decomposition at 492.5 °C, and maximum decomposition at 517.0 °C as shown in Table 27. The thermal stability of PP was improved upon the addition of L-CNCs in the functionalized PP system, which is attributed to the interaction of functionalized PP and L-CNCs through covalent bonding. Correa et al. observed an improvement in the thermal stability of cellulose whiskers in the presence of polyamide as a compatibilizer.[183]

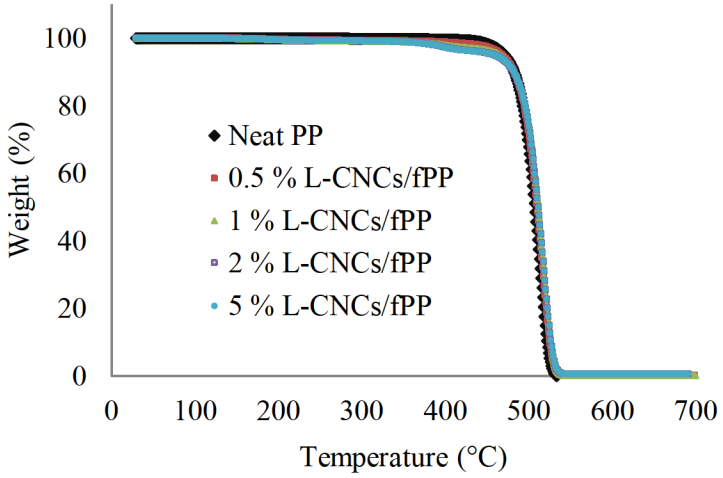

Figure 104. TGA curves for neat PP and L-CNCs/*f*PP nanocomposites at a constant heating rate of 20 °C/min.

Table 27. TGA Parameters of Neat PP and L-CNCs/*f*PP Nanocomposites at a Constant Heating Rate of 20 °C/min.

Sample Designation	1st Stage T_d (°C)	2nd Stage T_d (°C)	DTG (°C)
neat PP	-	490.3	515.3
0.5 % L-CNCs/*f*PP	333.9	492.5	517.0
1 % L-CNCs/*f*PP	345.5	494.3	517.4
2 % L-CNCs/*f*PP	351.0	493.8	517.8
5 % L-CNCs/*f*PP	354.3	495.9	517.7

5.7 Mechanical Properties: Tensile Testing of PP Nanocomposites

5.7.1 Mechanical Properties of Neat PP and L-CNCs/PP Nanocomposites

Representative tensile stress-strain curves of neat PP and L-CNCs/PP nanocomposites with respect to L-CNC loading are shown in Figure 105. From the stress-strain data, the tensile parameters including Young's modulus, ultimate tensile

strength, tensile strength at break and elongation at break were calculated for neat PP and L-CNCs/PP nanocomposites as shown in Figures 106, 107, 108, and 109, respectively. The actual values are summarized in Table 28. Figure 106 presents Young's modulus values of neat PP and L-CNCs/PP nanocomposites as a function of L-CNC loading. Due to the combination of CNCs tensile modulus of ~7.5-7.7 GPa and tensile strength of 110-220 GPa, these nanofillers are potentially effective as reinforcement for polymers.[9] Thus, the addition of L-CNCs at low loadings enhanced the Young's modulus of PP. The incorporation of L-CNCs also increased the ultimate tensile strength as shown in Figure 107. The addition of 0.5 wt.% of L-CNCs increased Young's modulus by 18% and increased the ultimate tensile strength by 7%. The improved mechanical properties of the nanocomposites depend on several characteristics, the most significant being: the morphology of the polymeric matrix, in reference to crystallinity and crystal dimensions, better dispersion of L-CNCs into the polymeric matrix and strong interfacial interaction between the phases.[160]

The significant improvement in the mechanical properties is attributed to the excellent dispersion of L-CNCs. Furthermore, the L-CNCs are acting as reinforcing agents due to the enhanced mechanical properties of PP. Figure 107 presents the tensile strength at break, which slightly decreases due to the L-CNCs acting as stress initiators in the PP matrix. For neat PP, the typical behavior of a ductile material is observed with very high elongation at break at 146%, as shown in Figure 109 and Table 28. The addition of L-CNCs also causes the elongation at break to drastically decrease. Generally, it has been reported that the addition of CNCs has been shown to reduce the

elongation at break in the nanocomposite material as compared to the neat polymer matrix due to the stiffening effect of CNCs in the polymer.[184-185]

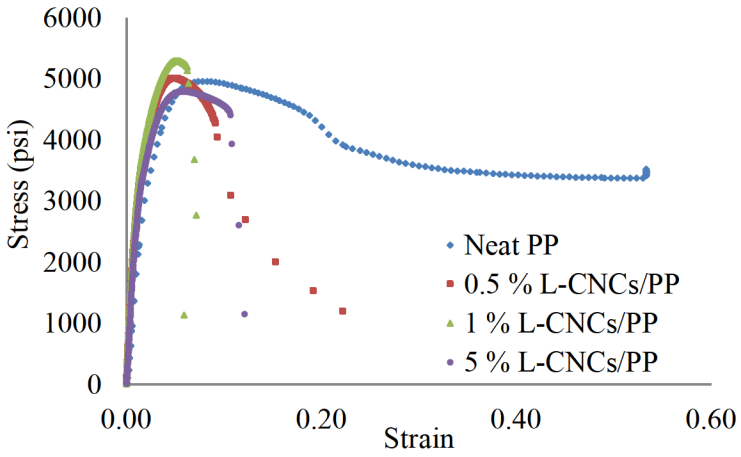

Figure 105. Representative stress-strain curves for neat PP and L-CNCs/PP nanocomposites.

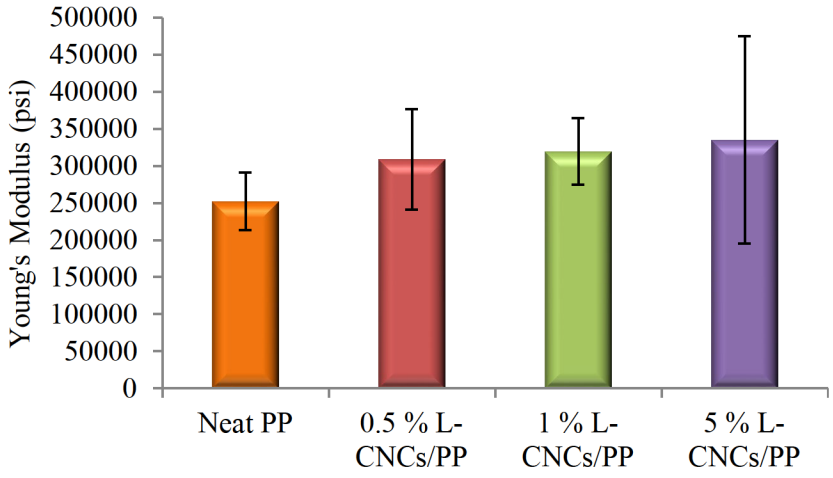

Figure 106. Young's modulus of neat PP and L-CNCs/PP nanocomposites as a function of L-CNC loading.

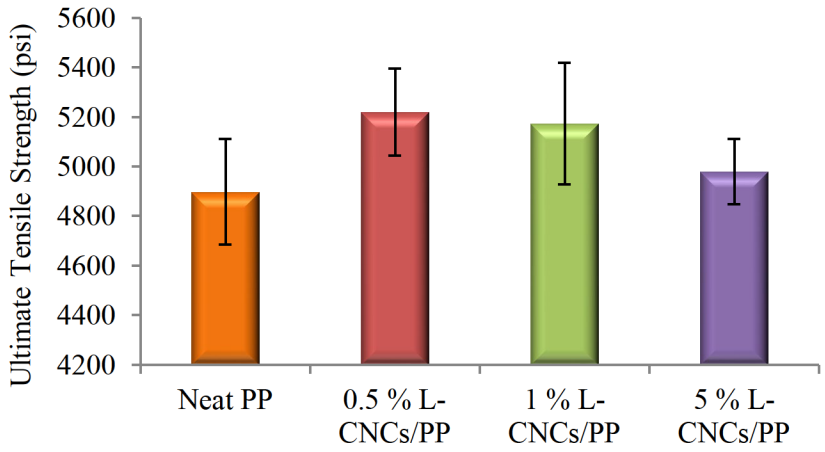

Figure 107. Ultimate tensile strength of neat PP and L-CNCs/PP nanocomposites as a function of L-CNC loading.

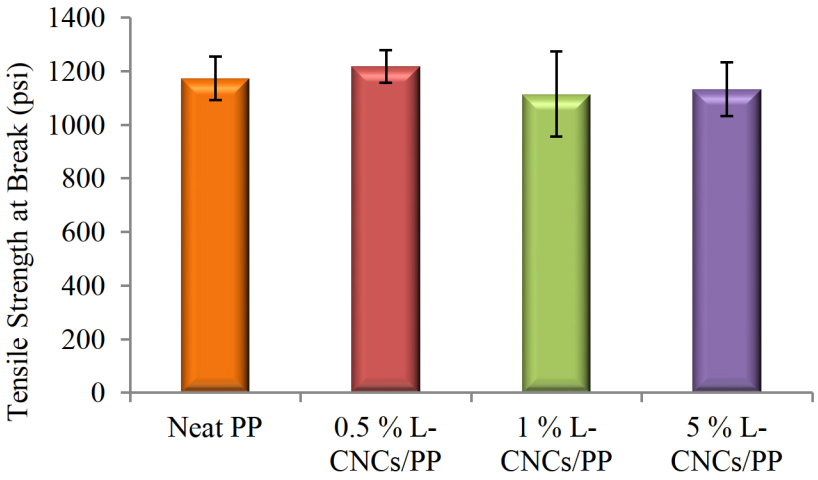

Figure 108. Tensile strength at break of neat PP and L-CNCs/PP nanocomposites as a function of L-CNC loading.

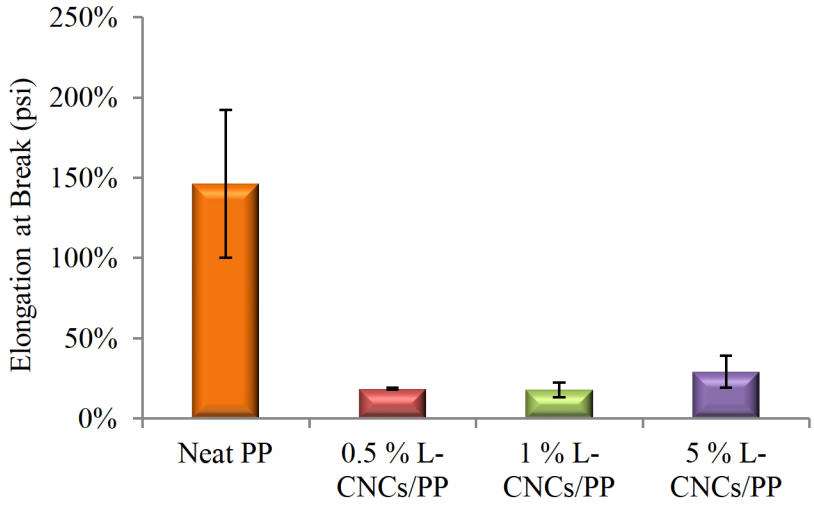

Figure 109. Elongation at break of neat PP and L-CNCs/PP nanocomposites as a function of L-CNC loading.

Table 28. The Tensile Properties of Neat PP and L-CNCs/PP Nanocomposites.

Sample Designation	Young's Modulus (psi)	Ultimate Tensile Strength (psi)	Tensile Strength at Break (psi)	Elongation at Break (%)
neat PP	252169 ±38573	4897 ±213	1174 ±81	146 ±46
0.5% L-CNCs/PP	297135±58125	5220 ±175	1218 ±61	19 ±1
1% L-CNCs/PP	296618±22581	5174 ±246	1115 ±158	18 ±5
5% L-CNCs/PP	290682 ±47058	4980 ±132	1133 ±100	29 ±10

5.7.2 Mechanical Properties of L-CNCs/*f*PP Nanocomposites

The mechanical properties of the neat PP and L-CNC/*f*PP nanocomposite samples were investigated using mechanical tensile tests. The stress-strain results are shown in Figure 110, and the values obtained are reported in Table 29. The addition of L-CNCs in

PP nanocomposites functionalized with MA resulted in an increase in Young's modulus, ultimate tensile strength, and tensile strength at break but lead to a decrease in the elongation at break values as shown in Figures 111, 112, 113, and 114, respectively. An increase in stiffness was observed due to the presence of MA, which can be related to the effect of the coupling agent on interfacial adhesion. It is evident in Figure 111 and Table 29 that the Young's modulus values of *f*PP increased by 8% and 7% due to the addition of 0.5 and 2 wt.% of L-CNCs, respectively. There is also a substantial improvement in the tensile strength at break for *f*PP, which increased by 23% and 112% due to the addition of 1 and 2 wt.% of L-CNCs, respectively. The increase in tensile strength at break is attributed to covalent bonding between L-CNCs and PP-g-MA polymer chains. As reported in Table 29, a marked increase of the Young modulus, ultimate tensile strength, and tensile strength at break was found for L-CNCs/*f*PP nanocomposites when compared to neat PP, while the elongation at break decreased, as reported for other natural fiber reinforced polymer composites.[186-188] All functionalized nanocomposites tensile tests showed a rather brittle behavior, other than that observed for neat PP. As mentioned, the addition of CNCs has been shown to decrease the elongation at break in the nanocomposite material compared to the neat polymer matrix due to the stiffening effect of CNCs in the polymer.[184-185] Results demonstrate that the incorporation of L-CNCs in functionalized PP enhanced the compatibility of a hydrophobic polymer and hydrophilic/hydrophobic L-CNCs. Comparable observations were reported for other lignocellulosic/PP composites.[189]

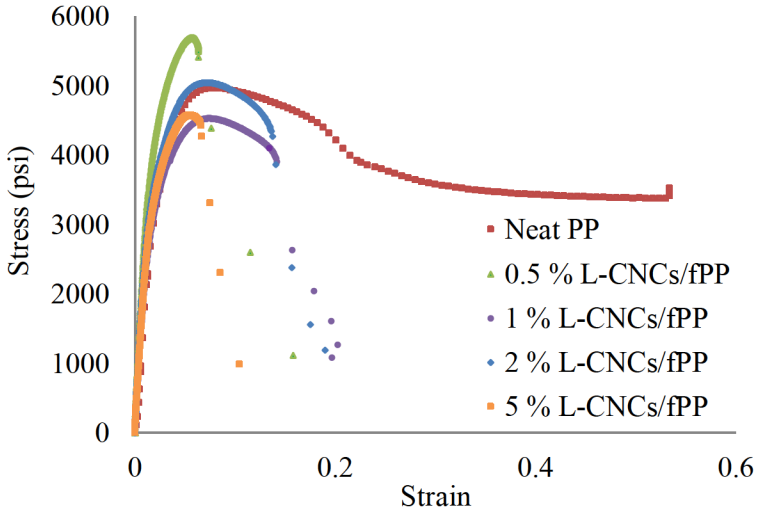

Figure 110. Representative stress-strain curves for neat PP and L-CNCs/*f*PP nanocomposites.

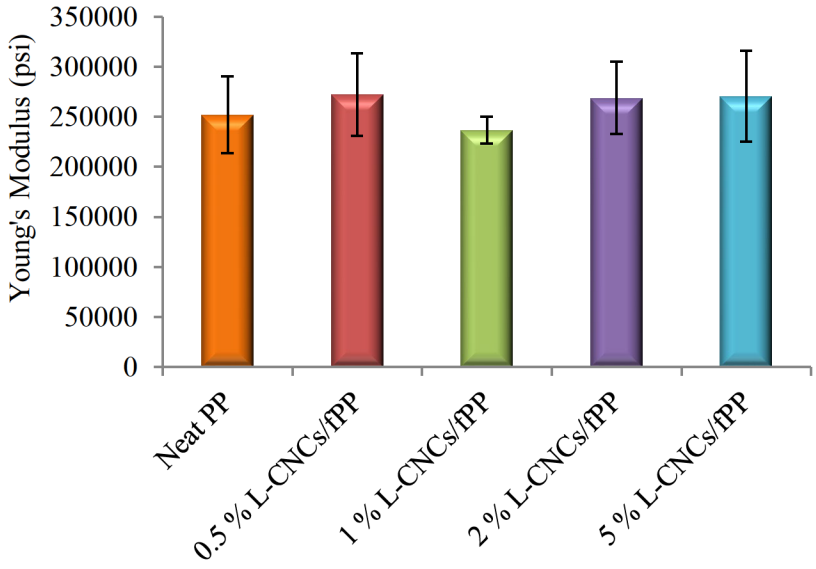

Figure 111. Young's modulus of neat PP and L-CNCs/*f*PP nanocomposites as a function of L-CNC loading.

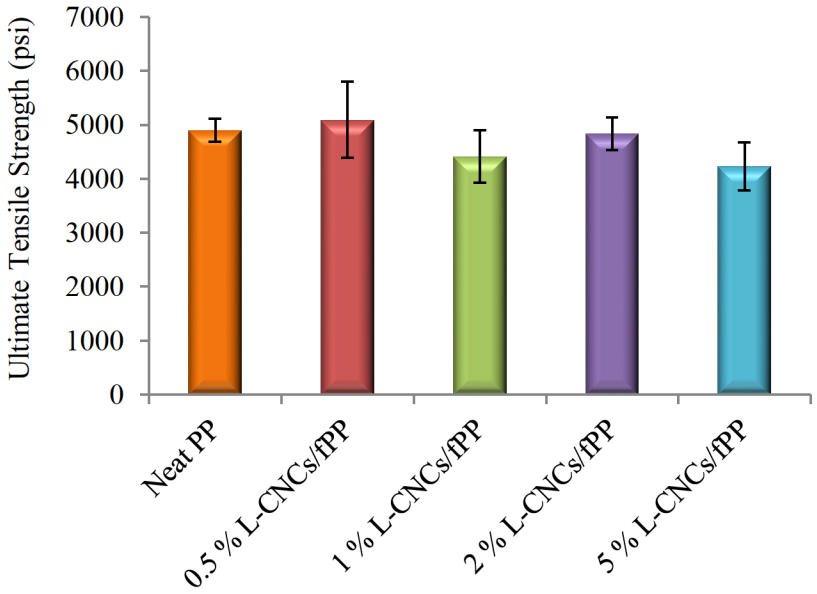

Figure 112. Ultimate tensile strength of neat PP and L-CNCs/*f*PP nanocomposites as a function of L-CNC loading.

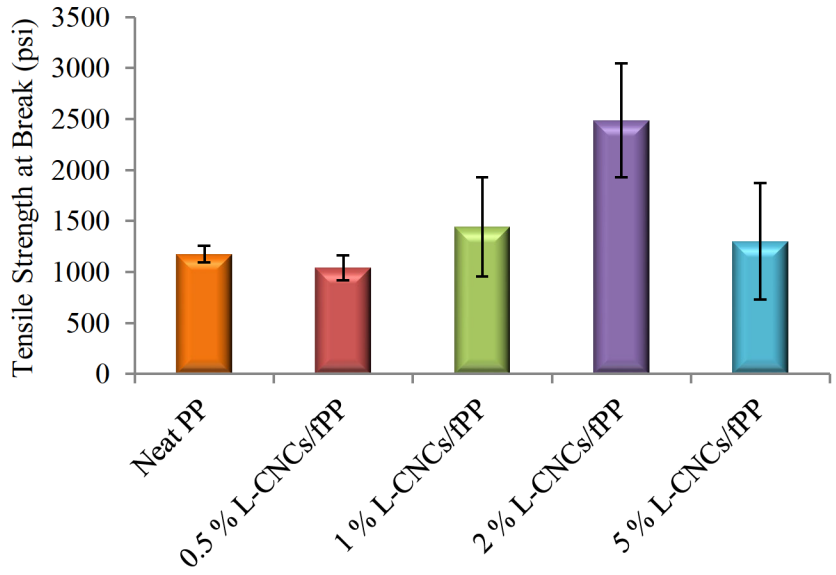

Figure 113. Tensile strength at break of neat PP and L-CNCs/*f*PP nanocomposites as a function of L-CNC loading.

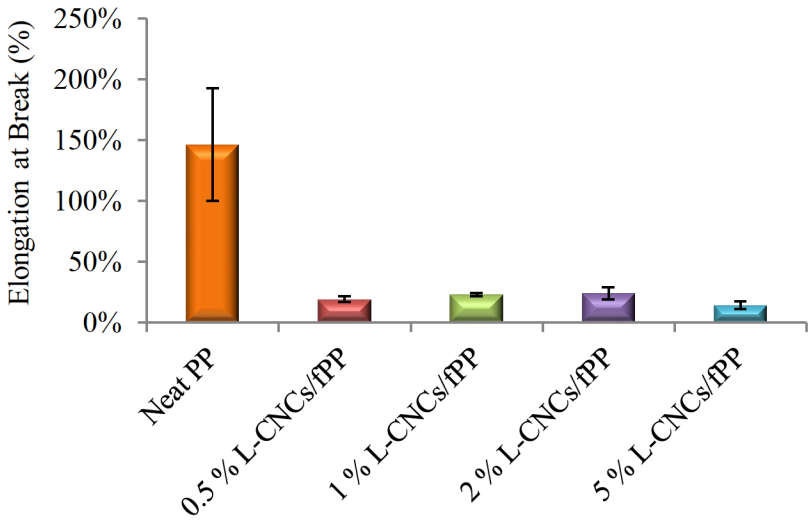

Figure 114. Elongation at break of neat PP and L-CNCs/*f*PP nanocomposites as a function of L-CNC loading.

Table 29. The Tensile Properties of Neat PP and L-CNCs/*f*PP Nanocomposites.

Sample Designation	Young's Modulus (psi)	Tensile Strength (psi)	Tensile Strength at Break (psi)	Elongation at Break (%)
neat PP	252169 ±38573	4897 ±213	1174 ±81	146 ±46
0.5% L-CNCs/*f*PP	272442±41301	5096 ±704	1041 ±125	19 ±2
1 % L-CNCs/*f*PP	236760±13661	4415 ±482	1444 ±485	23 ±1
2% L-CNCs/*f*PP	268997±36406	4838 ±304	2488 ±557	24 ±5
5% L-CNCs/*f*PP	231425 ±4646	4231 ±448	1300 ±573	14 ±3

5.8 Optical Microscopy of PP Nanocomposites

In order to study the dispersion of L-CNCs throughout the PP matrix at a small and large scale, the optical micrographs of 0.5 and 5 wt.% of L-CNCs in PP and *f*PP were

selected and studied using optical microscopy. As mentioned, the method used for studying the dispersion was based on the conventional melt-pressing method.

5.8.1 Optical Microscopy of L-CNCs/PP Nanocomposites

Figure 115 presents optical micrographs of PP with the addition of 0.5 and 5 wt.% L-CNCs. As shown in the images, L-CNC particles are randomly dispersed in PP and form aggregates. The dark spots observed in the optical micrographs are L-CNC aggregates. As mentioned, the particle sizes are depended on L-CNC loading. At 0.5 wt.%, the filler agglomerates are in lower magnitude and result in a better dispersion, while as 5 wt.%, larger agglomerates are formed. This is attributed to the interaction of weak van der Wal's forces or hydrogen bonding of L-CNCs.

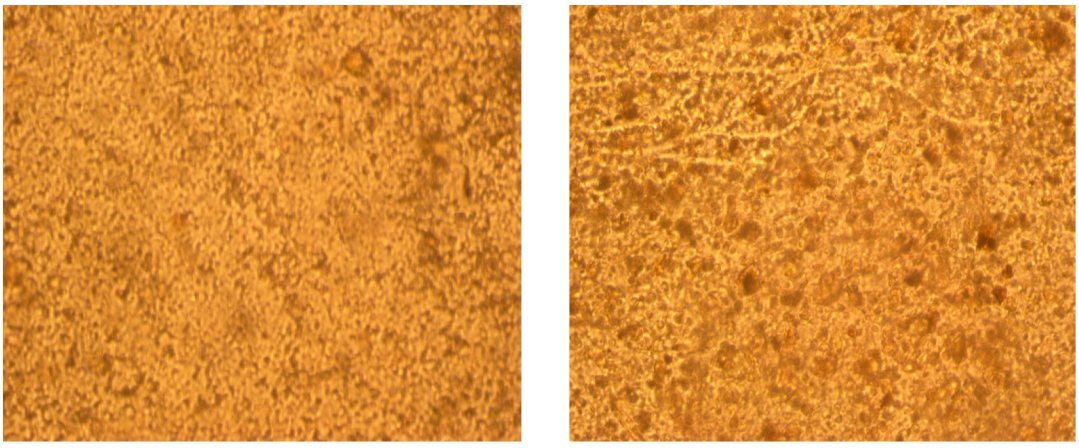

(a) (b)

Figure 115. Optical micrographs of (a) 0.5% L-CNCs/PP and (b) 5% L-CNCs/PP nanocomposites.

5.8.2 Optical Microscopy of L-CNCs/*f*PP Nanocomposites

The addition of L-CNCs in functionalized PP produced a more homogeneous nanocomposite with fewer filler aggregates, as shown in Figure 116. This indicated that the functionalization of PP had a positive effect on the interfacial interaction between filler and matrix. The optical images also suggest that there is improved interfacial bonding between L-CNCs and the PP matrix. The addition of 0.5 wt.% of L-CNCs showed a more homogeneous and a smoother surface with minimal aggregates as compared to high loading of 5 wt.% of L-CNCs.

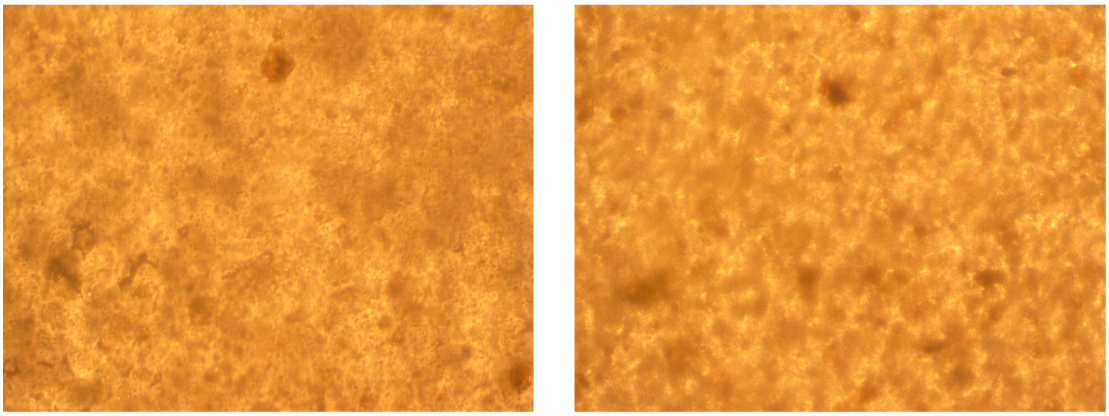

(a) (b)

Figure 116. Optical micrographs of (a) 0.5% L-CNCs/*f*PP and (b) 5% L-CNCs/*f*PP nanocomposites.

5.9 Conclusion

In this work, L-CNCs were incorporated in PP by high-torque melt-mixing, and PP was functionalized with MA with the addition of L-CNCs prepared by in situ free-radical polymerization by high-torque melt-mixing to facilitate better dispersion of L-CNCs within *f*PP and PP.

The effect of L-CNCs on the crystallinity properties of PP was investigated. The results showed no change in the crystalline behavior of PP; however, there was an observed increase in glass transition temperatures for all nanocomposites. Thermal decomposition results for the nanocomposites showed that the addition of L-CNCs in PP had a limited influence. It has been reported that L-CNCs incorporated in PP produce the following improvements in mechanical properties: Young's modulus, tensile strength at break, ultimate tensile strength can be improved. Mechanical testing results suggested a significant increase in tensile properties at 0.5 wt.% loading of L-CNCs, compared to that of neat PP. This was attributed to the coating of lignin on CNCs which resulted in significantly better CNC dispersion within the matrix. Rheology characterization suggested at low- and high-frequency rheological characteristics, loss modulus, storage modulus, and complex viscosity decreased upon the addition of L-CNCs. Increased interfacial area resulting from the high-level of dispersion of L-CNCs in PP was credited for the improvement in rheological parameters. For DMA results, L-CNCs/PP nanocomposites storage and loss modulus values increased upon the addition of L-CNCs. The highest storage modulus values are displayed by nanocomposites with L-CNC loadings of 0.5 and 5 wt.%. Clearly, the addition of L-CNCs at low loadings increased the storage modulus of PP. The increase in modulus is due to the presence of the highly rigid L-CNCs, which improved the rigidity of PP. The addition of L-CNCs increased the loss modulus values of PP from 30 to 100 °C, which is due to an increase in the interfacial interaction between L-CNCs and PP. From optical microscopy studies, it was

found that in the case of the 0.5 % L-CNCs/PP nanocomposites that the L-CNCs were better dispersed as compared to 5 % L-CNCs/PP nanocomposites.

As a result of poor dispersion and inefficient load transfer, the mechanical properties of PP/CNCs composites are often not as good as anticipated. The functionalization of PP will result in improved filler to matrix interaction. This, in turn, will enhance the dispersion of the L-CNCs leading to further property improvement of nanocomposite materials. Due to the functionalization of PP by grafting MA on PP, followed by the addition of L-CNCs, the mechanical properties of PP were improved while elongation at break values was reduced significantly. The maximum enhancement for Young's modulus, tensile strength at break, and tensile strength were achieved upon the addition of 0.5 and 2 wt.% of L-CNC loading. These observations confirmed that the efficiency of MA as a coupling agent favored a better dispersion of hydrophilic CNCs coated with lignin within the hydrophobic PP. The strong intermolecular van der Waals interactions among the CNCs, in combination with their high surface area and high aspect ratio as well as weak affinity to the nonpolar PP matrix, commonly causes significant agglomeration. The presence of MA can lead to strong hydrogen and covalent bonding of CNCs and maleic anhydride groups of PP-g-MA. The L-CNCs/*f*PP nanocomposites mechanical properties were enhanced due to increased interfacial interactions between L-CNC particles and *f*PP and better dispersion of L-CNCs. DSC analysis for L-CNCs/*f*PP nanocomposites showed an increase in percent crystallinity and glass transition temperatures as related to neat PP. All other DSC properties were unaffected by the addition of L-CNCs in functionalized PP. The addition of L-CNCs in *f*PP exhibited

superior thermal stability as related to neat PP. This was reflected by the fact that the onset temperature of thermal degradation and maximum decomposition increased with the incorporation of L-CNCs in *f*PP.

Rheology characterization suggested that the addition of L-CNCs obtained yielded nanocomposites with significantly better dispersion in the PP matrix. At low- and high-frequency rheological characteristics, loss modulus, storage modulus, and complex viscosity decreased upon the addition of L-CNCs. Rheological experiments determined that there was a change to the microstructure by the addition of L-CNCs in *f*PP. This may have been due to the functionalization of MA on the PP backbone and increased interfacial interactions between *f*PP. From optical microscopy studies, it was observed that in the case of the 0.5 % L-CNCs/*f*PP nanocomposites that the L-CNCs were better dispersed as compared to 0.5 % L-CNCs/PP nanocomposites. The optical data suggest that in the presence of MA, L-CNCs and PP interfacial interactions are enhanced due to homogeneous dispersion of CNCs.

As mentioned, the dispersion and distribution properties of the L-CNCs in PP were enhanced and led to further property improvement of the nanocomposite materials. For all data reported, the performance of all the nanocomposites depend on the amount of L-CNCs added in PP and mainly on the prepared microstructure. The improvement in the thermomechanical properties is attributed to the increased interaction between the PP and L-CNCs, leading to better interfacial interactions and higher levels of dispersion.

CHAPTER 6

CONCLUSION

6.1 General Overview

With the increasing development of nanomaterials, studies on nanocellulose based composites have been extensively carried out in order to find promising alternatives to traditional composites. This study describes the process-structure-property relationship of thermoplastic polymers reinforced with nanocellulose. The main objectives of this research were to enhance the interfacial interactions at filler and matrix interface and improve the dispersion of nanocellulose in UHMWPE, HDPE, and PP to achieve desired properties by various approaches. One of the advantages of CNCs as reinforcement agents is their large surface area, which can induce better interfacial interaction with the polymeric matrix, which is an essential factor for a useful improvement of the nanocomposite properties. However, CNCs tend to aggregate into bundles, and hence they are challenging to be dispersed homogeneously in polymer matrices. For this reason, lignin was coated on CNCs surface to induce better adhesion between CNCs and the polymer matrix. We were able to prepare novel nanocellulose composites via power sintering, high-torque melt-mixing, and *in situ* free radical polymerization. This work clearly shows that L-CNCs and L-CNFs can be effectively used as reinforcing agents in

polyolefin matrices. Our work also suggests that from the combination of L-CNCs and optimal grafting of MA with the use of DCP as a radical initiator, and reaction conditions, one can succeed in the preparation of high-performance nanocomposite materials.

REFERENCES

1. Thakur, V. K.; Thakur, M. K.; Asokan, P. *Hybrid Polymer Composite Systems: Applications*. Woodhead Publishing: 2017.

2. Thompson, R. C.; Moore, C. J.; vom Saal, F. S.; Swan, S. H. Plastics, the environment and human health: current consensus and future trends. *Philos. Trans. R. Soc. Lond. B. Biol. Sci.* **2009,** *364*, 2153-2166.

3. David, N. V.; Gao, X.-L.; Zheng, J. Ballistic Resistant Body Armor: Contemporary and Prospective Materials and Related Protection Mechanisms. *Applied Mechanics Reviews - APPL MECH REV.* **2009,** *62*.

4. Han, J. S.; Rowell, J. S. Chemical Composition of Fibers. In *Paper and Composites from Agro-Based Resources* [Online] Rowell R.M., Y. R. A., Rowell J., Ed. CRC Press: London, 1996; p pp. 83-130. (accessed April 7, 2018).

5. Varshney, V. K.; Naithani, S. Chemical Functionalization of Cellulose Derived from Nonconventional Sources. In *Cellulose Fibers: Bio and Nano-Polymer Composites*, Kalia S, K. B., Kaur I, Ed. Springer: Berlin, 2011; pp 43–60.

6. Lavanya, D.; Kulkarni, P.; Dixit, M.; Raavi, P. K. Sources of cellulose and their applications- A review. *International Journal of Drug Formulation and Research.* **2011,** *2*, 19-38.

7. Postek, M.; Vladar, A.; Dagata, J.; Farkas, N.; Ming, B.; Wagner, R.; Raman, A.; Moon, R. J.; Sabo, R.; Wegner, R. T. H.; Beecher, J. *Meas. Sci. Technol.* **2011,** *22*.

8. Moon, R. J.; Martini, A.; Nairn, J.; Simonsen, S.; J., Y. Cellulose nanomaterials review: structure, properties and nanocomposites. *Chem. Soc. Rev.* **2011,** *40*, 3941–3994.

9. Börjesson, M.; Westman, G. Crystalline Nanocellulose — Preparation, Modification, and Properties. *Cellulose – fundamental aspects and current trends.* [Online] 2015, p. 159–191. (accessed April 5, 2018)

10. Poletto, M.; Pistor, V.; Zattera, A. Structural Characteristics and Thermal Properties of Native Cellulose. In *Cellulose - Fundamental Aspects*, 2013.

11. Nishiyama, Y. Molecular interactions in nanocellulose assembly. *Philos. Trans. A. Math Phys. Eng. Sci.* **2018,** *376*, 2017-47.

12. De Carvalho, K. C. C.; Montoro, S. R.; Cioffi, M. O. H.; Voorwald, H. J. C. Chapter 13 - Polyhydroxyalkanoates and Their Nanobiocomposites With Cellulose Nanocrystals. In *Design and Applications of Nanostructured Polymer Blends and Nanocomposite Systems*, Thomas, S.; Shanks, R.; Chandrasekharakurup, S., Eds. William Andrew Publishing: Boston, 2016; pp 261-285.

13. Saba, N.; Jahir, P. M.; Jawaid, M. *A Review on Potentiality of Nano Filler/Natural Fiber Filled Polymer Hybrid Composites*. 2014; p 2247-2273.

14. Boluk, Y.; Ensor, D.; Moon, R. Roadmap for the Development of International Standards for Nanocellulose. 2011, p. 1-26. (accessed October 24, 2011).

15. Moon, R. J.; Frihart, C. R.; Wegner, T. Nanotechnology Applications in the Forest Products Industry. *For. Prod. J.* **2006,** *56*, 4-10.

16. Dong, X. M.; Revol, J.-F.; Gray, D. G. Effect of microcrystallite preparation conditions on the formation of colloid crystals of cellulose. *Cellulose.* **1998,** *5*, 19–32.

17. Habibi, Y.; Lucia, L.; Rojas, O. Cellulose Nanocrystals: Chemistry, Self-Assembly, and Applications. *Chem. Rev.* **2010,** *110*, 3479-3500.

18. Saito, T.; Hirota, M.; Tamura, N.; Kimura, S.; Fukuzumi, H.; Heux, L.; Isogai, A. Individualization of Nano-Sized Plant Cellulose Fibrils by Direct Surface Carboxylation Using TEMPO Catalyst under Neutral Conditions. *Biomacromolecules.* **2009,** *10*, 1992-1996.

19. Mishra, R. K.; Ha, S. K.; Verma, K.; Tiwari, S. K. Recent progress in selected bio-nanomaterials and their engineering applications: An overview. *Journal of Science: Advanced Materials and Devices.* **2018,** *3*, 263-288.

20. Stevanovic, T. Cellulose. In *Chemistry of Lignocellulosics: Current Trends*, CRC Press: 2018; p 308.

21. Chakrabarty, A.; Teramoto, Y. Recent Advances in Nanocellulose Composites with Polymers: A Guide for Choosing Partners and How to Incorporate Them. *Polymers.* **2018,** *10*, 517.

22. Håkansson, H.; Ahlgren, P. Acid hydrolysis of some industrial pulps: Effect of hydrolysis conditions and raw material. *Cellulose.* **2005,** *12*, 177-183.

23. Beck-Candanedo, S.; Roman, M.; Gray, D. G. Effect of Reaction Conditions on the Properties and Behavior of Wood Cellulose Nanocrystal Suspensions. *Biomacromolecules.* **2005,** *6*, 1048–1054.

24. Pang, W.; Ni, Z.; Chen, G.; Huang, G.; Huang, H.; Zhao, Y. Mechanical and thermal properties of graphene oxide/ultrahigh molecular weight polyethylene nanocomposites. *RSC Advances.* **2015,** *5*, 63063-63072.

25. Marchessault, R. H.; Morehead, F. F.; Koch, M. J. Some hydrodynamic properties of neutral suspensions of cellulose crystallites as related to size and shape. *J. Colloid Sci.* **1961,** *16*, 327–344.

26. Valencia, L.; Nomena, E. M.; Mathew, A. P.; Velikov, K. P. Biobased Cellulose Nanofibril–Oil Composite Films for Active Edible Barriers. *ACS Appl. Mater. Interfaces.* **2019,** *11*, 16040-16047.

27. Bhatnagar, A.; Sain, M. Processing of Cellulose Nanofiber-reinforced Composites. *J. Reinf. Plast. Comp.* **2005,** *24*, 1259–1268.

28. Kamel, S. Nanotechnology and its applications in lignocellulosic composites, a mini review. *eXPRESS Polym. Lett.* **2007,** *1*, 546-575.

29. De Menezes, A. J.; Siqueira, G.; Curvelo, A.; Dufresne, A. Extrusion and Characterisation of Functionalised Cellulose Whiskers Reinforced Polyethylene Nanocomposites. *Polymer.* **2009,** *50*, 4552-4563.

30. Pereda, M.; Kissi, N. E.; Dufresne, A. Extrusion of Polysaccharide Nanocrystal Reinforced Polymer Nanocomposites through Compatibilization with Poly(ethylene oxide). *ACS Appl. Mater. Interfaces.* **2014,** *6*, 9365-9375.

31. Volk, N.; He, R.; Magniez, K. Enhanced homogeneity and interfacial compatibility in melt-extruded cellulose nano-fibers reinforced polyethylene via surface adsorption of poly(ethylene glycol)-block-poly(ethylene) amphiphiles. *Eur. Polym. J.* **2015,** *72*, 270-281.

32. Dufresne, A. Comparing the Mechanical Properties of High Performances Polymer Nanocomposites from Biological Sources. *J. Nanosci. Nanotechnol.* **2006,** *6*, 322-330.

33. Azizi Samir, M. A. S.; Alloin, F.; Dufresne, A. Review of Recent Research into Cellulosic Whiskers, Their Properties and Their Application in Nanocomposite Field. *Biomacromolecules.* **2005,** *6*, 612-626.

34. Cavdar, A. D.; Mengeloglu, F.; Karakus, K.; Dizman Tomak, E. Effect of Chemical Modification with Maleic, Propionic, and Succinic Anhydrides on Some Properties of Wood Flour Filled HDPE Composites. *BioResources.* **2014,** *9*, 12.

35. Capron, I.; Rojas, O. J.; Bordes, R. Behavior of nanocelluloses at interfaces. *Curr. Opin. Colloid Interface Sci.* **2017,** *29*, 83–95.

36. Yuan, W.; Guo, M.; Miao, Z.; Liu, Y. Influence of maleic anhydride grafted polypropylene on the dispersion of clay in polypropylene/clay nanocomposites. *Polym. J.* **2010,** *42*.

37. Sato, A.; Kabusaki, D.; Okumura, H.; Nakatani, T.; Nakatsubo, F.; Yano, H. Surface modification of cellulose nanofibers with alkenyl succinic anhydride for high-density polyethylene reinforcement. *Compos. Pt. A Appl. Sci. Manuf.* **2016,** *83*, 72–79.

38. Peng, Y.; Gallegos, S. A.; Gardner, D. J.; Han, Y.; Cai, Z. Maleic anhydride polypropylene modified cellulose nanofibril polypropylene nanocomposites with enhanced impact strength. *Polym. Compos.* **2016,** *37*, 782–793.

39. Nelson, K.; Retsina, T.; Iakovlev, M.; van Heiningen, A.; Deng, Y. *American Process: Production of Low Cost Nanocellulose for Renewable, Advanced Materials Applications*. Springer International Publishing: Switzerland, 2016.

40. Nelson, K.; Retsina, T. Innovative nanocellulose process breaks the cost barrier. *TAPPI.* **2014,** *13*, 19 – 23.

41. Marshall, J. S. Comparative kinetic study of the thermal decomposition of nanocellulose produced by H_2SO_4 hydrolysis, Tempo, and AVAP processes. Clark Atlanta University, ETD Collection for AUC, Robert W. Woodruff Library, 2015.

42. Gupta, A.; Simmons, W.; Schueneman, G.; Mintz, E. Lignin-coated cellulose nanocrystals as promising nucleating agent for poly(lactic acid). *J. Therm. Anal. Calorim.* **2016**, 1-9.

43. Gupta, A.; Simmons, W.; Schueneman, G. T.; Hylton, D.; Mintz, E. A. Rheological and Thermo-Mechanical Properties of Poly(lactic acid)/Lignin-Coated Cellulose Nanocrystal Composites. *ACS Sustain. Chem. Eng.* **2017,** *5*, 1711-1720.

44. Hambardzumyan, A.; Foulon, L.; Chabbert, B.; Aguié-Béghin, V. Natural Organic UV-Absorbent Coatings Based on Cellulose and Lignin: Designed Effects on Spectroscopic Properties. *Biomacromolecules.* **2012,** *13*, 4081-4088.

45. Ago, M.; Jakes, J. E.; Johansson, L.-S.; Park, S.; Rojas, O. J. Interfacial Properties of Lignin-Based Electrospun Nanofibers and Films Reinforced with Cellulose Nanocrystals. *ACS Appl. Mater. Interfaces.* **2012,** *4*, 6849-6856.

46. Cavallaro, P. V. *NUWC-MPT Technical report 12,057*; August, 2011.

47. Benitez, A.; Walther, A. Cellulose nanofibril nanopapers and bioinspired nanocomposites: A review to understand the mechanical property space. *J. Mater. Chem. A.* **2017,** *5*, 16003-16024.

48. Geyer, R.; Jambeck, J. R.; Law, K. L. Production, use, and fate of all plastics ever made. *Sci. Adv.* **2017,** *3*, 1700-1782.

49. Oromiehie, A.; Ebadi-Dehaghani, H. Chemical Modification of Polypropylene by Maleic Anhydride: Melt Grafting, Characterization and Mechanism. *Int. J. Chem. Eng. Appl.* **2014,** *5*, 117-122.

50. Lu, J. Z.; Wu, Q.; Negulescu, I. I. Wood-fiber/high-density-polyethylene composites: Coupling agent performance. *J. Appl. Polym. Sci.* **2005,** *96*, 93-102.

51. Zadorecki, I.; Flodin, P. The effect of cellulose fiber treatment on the performance of cellulose-polyester composite. *J. Appl. Polym. Sci.* **1985,** *30*, 3971-3983.

52. El-Sonbati, A. Z. *THERMOPLASTIC– COMPOSITE MATERIALS*. INTECH: Rijeka, Croatia, 2012; p 156.

53. Maddah, H. Polypropylene as a Promising Plastic: A Review. *Am. J. Polym. Sci.* **2016,** *6*, 1-11.

54. Bledzki, A. K.; Fink, H. P.; Specht, K. Unidirectional hemp and flax EP- and PP-composites: Influence of defined fiber treatments. *J. Appl. Polym. Sci* **2004,** *93*, 2150–2156.

55. Shubhra, Q. T. H.; Alam, A. K. M. M.; Quaiyyum, M. A. Mechanical properties of polypropylene composites: A review *J. Thermoplast. Compos. Mater.* **2011,** *26*, 362–391.

56. Shubhra, Q. T. H.; Alam, A. K. M. M.; Beg, M. D. H.; Khan, M. A.; Gafur, M. A. Mechanical and degradation characteristics of natural silk and synthetic phosphate glass fiber reinforced polypropylene composites. *J. Compos. Mater.* **2011,** *45*, 1305–1313.

57. The Universal Selection Source: Plastics & Elastomers. https://omnexus.specialchem.com/selection-guide/polypropylene-pp-plastic.

58. Morrison, R. T.; Boyd, R. N. *Organic Chemistry*. 6th ed.; Prentice-Hall, Inc.: Englewood Cliffs, NJ, 1992.

59. Maldas, D.; Kokta, B. V. Improving adhesion of wood fiber with polystyrene by chemical treatment of fiber with coupling agent and the influence of the mechanical properties of the composites. *J. Adhes. Sci. Technol.* **1989,** *3*, 529-539.

60. John, W. E. Isocyanatc as wood binders: A review. *J. Adhes.* **1982,** *15*, 59-67.

61. Beshay, A. D.; Kokta, B. V.; Dancault, C. Use of wood fibers in thermoplastic composites: polyethylene. *Polym. Comp. 6*, 261-271.

62. *Dow UNIPOL Technology Handbook*. Chem Systems: 2001.

63. Karian, H. G. *Handbook of Polypropylene and Polypropylene Composites*. New York: Marcel Dekker: 1999.

64. He, C. Molecular structure of high melt strength polypropylene and its application to polymer design. *Polymer.* **2003,** *44*, 7181-7188.

65. Gatenholm, P.; Felix, J.; Klason, C.; Kubat, J. Cellulose-polymer composites with improved properties. In *Contemporary topics in polymer science: Advances in new materials* Salamone, J. C.; Riffle, J. S., Eds. Plenum Press New York, NY, 1992; Vol. 7, pp 75-82.

66. Samay, G.; Nagy, T.; White, J. L. Grafting maleic anhydride and comonomers onto polyethylene. *J. Appl. Polym. Sci.* **1995,** *56*, 1423-1433.

67. Vito, G. D.; Lanzetta, N.; Maglio, G.; Malinconico, M.; Musto, P.; Palumbo, R. Functionalization of an amorphous ethylenepropylene copolymer by free radical initiated grafting of unsaturated molecules. *J. Polym. Sci. Polym. Lett. Chem.* **1984,** *22*, 1335-1347.

68. De Roover, B.; Sclavons, M.; Carlier, V.; Devaux, J.; Legras, R.; Momtaz, A. Molecular characterization of maleic anhydride-functionalized polypropylene. *J. Polym. Sci. Pt. A Pol. Chem* **1995,** *33*, 829-842.

69. Alireza, A.; Amir, N. Polypropylene cellulose-based composites: The effect of bagasse reinforcement and polybutadiene isocyanate treatment on the mechanical properties. *J. Appl. Polym. Sci.* **2009,** *111*, 1684–1689.

70. Yuan, X.; Zhang, Y.; Zhang, X. Maleated polypropylene as a coupling agent for PP-waste news paper flour composites. *J. Appl. Polym. Sci* **1999,** *71*, 333–337.

71. Sanadi, A. R.; Young, R. A.; Clemons, C.; Rowell, R. M. Recycled newspaper fibres as reinforcing fillers in thermoplastics: Part I—Analysis of tensile and impact properties in PP. *J. Reinforc. Plast. Comp.* **1994,** *13*, 54–66.

72. Pracella, M.; Chionna, D.; Anguillesi, I.; Kulinski, Z.; Pio´rkowska, E. Functionalization, compatibilization and properties of polypropylene composites with hemp fibres. *Compos. Sci. Technol.* **2006,** *66*, 2218–30.

73. Arbelaiz, A.; Ferna´ndez, B.; Cantero, G.; Llano-Ponte, R.; Valea, A.; Mondragon, I. Mechanical properties of flax fibre/polypropylene composites. influence of fibre/matrix modification and glass fibre hybridization. *Compos. Pt. A Appl. Sci. Manuf.* **2005,** *36*, 1637–1644.

74. Sam-Jung, K.; Jin-Bok, M.; Gue-Hyun, K.; Chang-Sik, H. Mechanical properties of polypropylene/natural fiber composites: Comparison of wood fiber and cotton fiber. *Polym. Test.* **2008,** *27*, 801–806.

75. Sanjay, K. N.; Smita, M. Sisal glass fiber reinforced PP hybrid composites: Effect of MAPP on the dynamic mechanical and thermal properties. *J. Reinforc. Plast. Compos.* **2010,** *29*, 1551–1568.

76. Byoung-Hoo, L.; Hyun-Joong, K.; Hee-Jun, P. Performance of paper sludge/polypropylene fiber/lignocellulosic fiber composites. *J. Ind. Eng. Chem.* **2002,** *8*, 50–56.

77. Chtourou, H.; Reidi, B.; Ait-Kadi, A. Reinforcement of recycled polyolefins with wood fibers. *J. Reinf. Plast. Comp.* **1992,** *11*, 372-394.

78. Wang, L.; Gardner, D. J.; Bousfield, D. W. Cellulose nanofibril-reinforced polypropylene composites for material extrusion: Rheological properties. *Polym. Eng. Sci.* **2017,** *58*, 793–801.

79. Ferrer, A.; Hoeger, I. C.; Lu, X.; Rojas, O. J. Reinforcement of polypropylene with lignocellulose nanofibrils and compatibilization with biobased polymers. *J. Appl. Polym. Sci.* **2016,** *133*.

80. Iwamoto, S.; Yamamoto, S.; Lee, S.-H. Endo, T. Solid-state shear pulverization as effective treatment for dispersing lignocellulose nanofibers in polypropylene composites. *Cellulose.* **2014,** *21*, 1573–1580.

81. Westphal, S. P.; Ling, T. K.; Woo, L. Polyethylene structural heterogeneity by thermal and rheological techniques. *Thermochim. Acta.* **1996,** *272*, 181-189.

82. Patel, R. M. Polyethylene. In *Multilayer Flexible Packaging* Second ed.; Wagner, J. R., Ed. William Andrew Publishing: 2016; pp 17-34.

83. Plastics and Elastomers. https://omnexus.specialchem.com/selection-guide/polyethylene-plastic#UHMWPE.

84. George, T. Studies on Kaolin Clay Reinforced PS/HDPE Nanocomposites. *Indian J. Adv. Chem. Sci.* **2013,** *1*, 201-206.

85. Azeredo, H. M. C. d. Nanocomposites for food packaging applications. *Food Res. Int.* **2009,** *42*, 1240-1253.

86. Mehrabzadeh, M.; Kamal, M.; Quintanar, G. Maleic Anhydride Grafting onto HDPE by In situ Reactive Extrusion and its Effect on Intercalation and Mechanical Properties of HDPE/Clay Nanocomposites. *Iran. Polym. J.* **2009,** *18*, 833-842.

87. Gaylord, N. G.; Mehta, R.; Mohan, D. R.; Kumar, V. Maleation of linear low-density polyethylene by reactive processing. *J. Appl. Polym. Sci.* . **1992,** *44*, 1941-1949.

88. Gaylord, N. G.; Mishra, M. K. Nondegradative reaction of maleic anhydride and molten polypropylene in the presence of peroxides. *J. Polym. Sci. Polym. Lett.* **1983,** *21*, 23-30.

89. Semsarzadeh, M. A.; Mehrabzadeh, M.; Salehil, M. New Aspects of the Reaction of HDPE with Maleic Anhydride. *Iran. Polym. J.* **1999,** *8*, 271-278.

90. Wang, K.-H.; M-H., C.; C-M., K.; Y-S., C.; I-J., C. Synthesis and characterization of maleated polyethylene/clay nanocomposites. *Polymer.* **2001,** *42*, 9819-9826.

91. Koo, C.-M.; Ham, H.-T.; Kim, S.-O.; Wang, K.-H.; Kim, D.-C.; Zin, W.-C. Morphology evolution and anisotropic phase formation of the maleated polyethylene-layered silicate nanocomposites. *Macromolecules.* **2002,** *35*, 5116-5122.

92. Wang, K.-H.; Choi, M.-H.; Koo, C.-M.; Xu, M.; Chung, I.-J.; Jang, C.-M.; Choi, S.-W.; Song, H.-H. Morphology and physical properties of polyethylene/silicate nanocomposite prepared by melt intercalation. *J. Polym. Sci. B Polym. Phys.* **2002,** *10*, 1454-1463,.

93. Liang, G.; Xu, J.; Bao, S.; Xu, W. Polyethylene/maleic anhydride grafted polyethylene/organic-montmorillonite nanocomposites. I: preparation, microstructure, and mechanical properties. *J. Appl. Polym. Sci.* **2004,** *91*, 3974-3980.

94. Reinking, M. K.; Rufener, K. P. Shear modification of HDPE-clay nanocomposites. 2005.

95. Pinnavaia, J. J.; Beall, G. W. *Polymer Nanocomposites*. John Wiley: VCH: New York, 2000.

96. Zhang, Q.; Lippits, D. R.; Rastogi, S. Dispersion and Rheological Aspects of SWNTs in Ultrahigh Molecular Weight Polyethylene. *Macromolecules.* **2006,** *39*, 658-666.

97. Alexandre, M. l.; Dubois, P.; Sun, T.; Garces, J. M.; JÃ©rÃ´me, R. Polyethylene-layered silicate nanocomposites prepared by the polymerization-filling technique: synthesis and mechanical properties. *Polymer.* **2002,** *43*, 2123-2132.

98. Sadrani, S. A.; Ramazani, S. A. A.; Khorshidiyeh, S. E.; Jafari Esfad, N. Preparation of UHMWPE/carbon black nanocomposites by in situ Ziegler–Natta catalyst and investigation of product thermo-mechanical properties. *Polym. Bull.* **2015,** *73*, 1085-1101.

99. Visakh, P. M.; Morlanes, M. J. M. Polyethylene-Based Blends, Composites and Nanocomposites: State-of-the-Art, New Challenges and Opportunities. In *Polyethylene-Based Blends, Composites and Nanocomposites*, John Wiley & Sons, Inc.: 2015; pp 1-19.

100. Mierczynska, A.; Mayne-L'Hermite, M.; Boiteux, G.; Jeszka, J. K. Electrical and mechanical properties of carbon nanotube/ultrahigh-molecular-weight polyethylene composites prepared by a filler prelocalization method. *J. Appl. Polym. Sci.* **2007,** *105*, 158-168.

101. Duan, B.; Wang, M.; Zhou, W. Y.; Cheung, W. L.; Li, Z. Y.; Lu, W. W. Three-dimensional nanocomposite scaffolds fabricated via selective laser sintering for bone tissue engineering. *Acta Biomater.* **2010,** *6*, 4495-4505.

102. Cheng, Q.; Wang, S.; Rials, T. G.; Lee, S.-H. Physical and mechanical properties of polyvinyl alcohol and polypropylene composite materials reinforced with fibril aggregates isolated from regenerated cellulose fibers. *Cellulose.* **2007,** *14*, 593-602.

103. Liu, H.; Liu, D.; Yao, F.; Wu, Q. Fabrication and properties of transparent polymethylmethacrylate/cellulose nanocrystals composites. *Bioresour. Technol.* **2010,** *101*, 5685-5692.

104. Siqueira, G.; Bras, J.; Dufresne, A. Cellulose Whiskers versus Microfibrils: Influence of the Nature of the Nanoparticle and its Surface Functionalization on the Thermal and Mechanical Properties of Nanocomposites. *Biomacromolecules.* **2009,** *10*, 425-432.

105. Gray, D. G. Transcrystallization of polypropylene at cellulose nanocrystal surfaces. *Cellulose.* **2008,** *15*, 297-301.

106. Yeh, J.-T.; Tsai, C.-C.; Wang, C.-K.; Shao, J.-W.; Xiao, M.-Z.; Chen, S.-C. Ultradrawing Novel Ultra-High Molecular Weight Polyethylene Fibers Filled with Bacterial Bellulose Nanofibers. *Carbohyd. Polym.* **2014,** *101*, 1-10.

107. Eichhorn, S. D., A.; Aranguren, M.; Marcovich, N.; Capadona, J.; Rowan,; S.; Weder, C. T., W.; Roman, M.; Renneckar, S. *J. Mater. Sci.* **2010,** *45*.

108. Hubbe, M. A.; Rojas, O. J.; Lucia, L. A.; Sain, M. Cellulosic Nanocomposites—A Review. *BioResources* **2008,** *3*, 929-980.

109. Hambir, S.; Jog, J. Sintering of ultra high molecular weight polyethylene. *Bull. Mater. Sci.* **2000,** *23*, 221-226.

110. Bondeson, D.; Oksman, K. *Compos. Interfaces.* **2007,** *14*, 617.

111. Oksman, K.; Mathew, A. P.; Bondeson, D.; Kvien, I. *Compos. Sci. Technol.* **2006,** *66*, 2776.

112. Khoshkava, V.; Kamal, M. R. Effect of Cellulose Nanocrystals (CNC) Particle Morphology on Dispersion and Rheological and Mechanical Properties of Polypropylene/CNC Nanocomposites. *ACS Appl. Mater. Interfaces.* **2014,** *6*, 8146-8157.

113. Fang, L.; Leng, Y.; Gao, P. Processing and mechanical properties of HA/UHMWPE nanocomposites. *Biomaterials.* **2006,** *27*, 3701-3707.

114. Crown Plastic Inc. http://crownplasticsinc.com/.

115. Siqueira, G.; Bras, J.; Dufresne, A. Cellulosic bionanocomposites: a review of preparation, properties and applications. *Polymers.* **2010,** *2*, 728-765.

116. Fu, Q.; Men, Y.; Strobl, G. Understanding of the tensile deformation in HDPE/LDPE blends based on their crystal structure and phase morphology. *Polymer.* **2003,** *44*, 1927-1933.

117. Kim, Y. C. Effect of maleated polyethylene on the crystallization behavior of LLDPE/clay nanocomposites. *Polymer journal.* **2006,** *38*, 250.

118. Liu, Y.; Yang, Q.; Li, G. Nonisothermal crystallization behavior of LLDPE/glass fiber composite. *Journal of applied polymer science.* **2008,** *109*, 782-788.

119. Gupta, A.; Rana, S.; Deopura, B. Crystallization kinetics of high-density polyethylene/linear low-density polyethylene blend. *Journal of applied polymer science.* **1994,** *51*, 231-239.

120. Mirabella, F. M.; Bafna, A. Determination of the crystallinity of polyethylene/α-olefin copolymers by thermal analysis: Relationship of the heat of fusion of 100% polyethylene crystal and the density. *Journal of Polymer Science Part B: Polymer Physics.* **2002,** *40*, 1637-1643.

121. Ten, E.; Bahr, D. F.; Li, B.; Jiang, L.; Wolcott, M. P. Effects of Cellulose Nanowhiskers on Mechanical, Dielectric, and Rheological Properties of Poly(3-hydroxybutyrate-co-3-hydroxyvalerate)/Cellulose Nanowhisker Composites. *Industrial & Engineering Chemistry Research.* **2012,** *51*, 2941-2951.

122. Xu, X.; Liu, F.; Jiang, L.; Zhu, J. Y.; Haagenson, D.; Wiesenborn, D. P. Cellulose Nanocrystals vs. Cellulose Nanofibrils: A Comparative Study on Their Microstructures and Effects as Polymer Reinforcing Agents. *ACS Applied Materials & Interfaces.* **2013,** *5*, 2999-3009.

123. Gupta, A.; Choudhary, V. Thermal and mechanical properties of poly(trimethylene terephthalate)/acid-treated multiwalled carbon nanotube composites. *J. Mater. Sci.* **2013,** *48*, 7063-7070.

124. Xu, G.; Zhu, Q. Studies on Crystallization and Melting Behaviors of UHMWPE/ MWNTs Nanocomposites with Reduced Chain Entanglements. *Polymers and Polymer Composites.* **2017,** *25*, 495-506.

125. Mandelkern, L. *Crystallization of Polymers: Volume 2, Kinetics and Mechanisms*. Cambridge University Press: 2004.

126. Farjas, J.; Roura, P. Modification of the Kolmogorov-Johnson-Mehl-Avrami rate equation for non-isothermal experiments and its analytical solution. *Acta Materialia.* **2008,** *54*.

127. Androsch, R.; Schick, C. Crystal Nucleation of Polymers at High Supercooling of the Melt. 2015; Vol. 276.

128. Avrami, M. Kinetics of Phase Change. I General Theory. *J. Chem. Phys.* **1939,** *7*, 1103-1112.

129. Avrami, M. Kinetics of Phase Change. II Transformationâ€□Time Relations for Random Distribution of Nuclei. *J. Chem. Phys.* **1940,** *8*, 212-224.

130. Keridou, I.; Del Valle, L. J.; Funk, L.; Turon, P.; Franco, L.; Puiggalí, J. Non-Isothermal Crystallization Kinetics of Poly(4-Hydroxybutyrate) Biopolymer. *Molecules.* **2019,** *24*, 2840.

131. Menczel, J. D.; Prime, R. B. *Thermal Analysis of Polymers: Fundamentals and Applications*. Wiley: 2014.

132. Matusita, K.; Komatsu, T.; Yokota, R. Kinetics of non-isothermal crystallization process and activation energy for crystal growth in amorphous materials. *J. Mater. Sci.* **1984,** *19*, 291-296.

133. Vyazovkin, S.; Sbirrazzuoli, N. Estimating the activation energy for non-isothermal crystallization of polymer melts. *J. Therm. Anal. Calorim.* **2003,** *72*, 681-686.

134. Vyazovkin, S.; Sbirrazzuoli, N. Isoconversional Kinetic Analysis of Thermally Stimulated Processes in Polymers. *Macromol. Rapid Commun.* **2006,** *27*, 1515-1532.

135. Kalkar, A. K.; Deshpande, V. D.; Vatsaraj, B. S. Isoconversional kinetic analysis of DSC data on nonisothermal crystallization: Estimation of Hoffman-Lauritzen parameters and thermal transitions in PET/MMT nanocomposites. *Polymer.* **2014,** *55*, 6948-6959.

136. Papageorgiou, D. G.; Filippousi, M.; Pavlidou, E.; Chrissafis, K.; Van Tendeloo, G.; Bikiaris, D. Effect of clay modification on structure-property relationships and thermal degradation kinetics of β-polypropylene/clay composite materials. *J. Therm. Anal. Calorim.* **2015,** *122*, 393-406.

137. Friedman, H. L. Kinetics of thermal degradation of char-forming plastics from thermogravimetry. Application to a phenolic plastic. *J. Polym. Sci. Pt. C Pol. Symp.* **1964,** *6*, 183-195.

138. Wang, S.; Feng, Q.; Sun, J.; Gao, F.; Fan, W.; Zhang, Z.; Li, X.; Jiang, X. Nanocrystalline Cellulose Improves the Biocompatibility and Reduces the Wear Debris of Ultrahigh Molecular Weight Polyethylene via Weak Binding. *ACS Nano.* **2016,** *10*, 298-306.

139. Mechanical Properties of Materials. https://mechanicalc.com/reference/mechanical-properties-of-materials.

140. Gupta, A.; Choudhary, V. Effect of multi-walled carbon nanotubes on mechanical and rheological properties of poly(trimethylene terephthalate). *J. Mater. Sci.* **2014,** *49*, 3839-3846.

141. Xie, H.; Yang, X.; Si, C. Recent Strategies in Preparation of Cellulose Nanocrystals and Cellulose Nanofibrils Derived from Raw Cellulose Materials. *International Journal of Polymer Science.* **2018,** *2018*, 1-25.

142. Ames, G. R.; Boeka, D. BALLISTICS 2014: 28th International Symposium on Ballistics. DEStech Publications, Inc: 2014; p 1789.

143. Sewda, K.; Maiti, N. Dynamic mechanical properties of high density polyethylene and teak wood flour composites. *Polym. Bull.* **2013,** *70*, 2657-2674.

144. Mohagheghian, I.; McShane, G. J.; Stronge, W. J. Impact perforation of monolithic polyethylene plates: Projectile nose shape dependence. *International Journal of Impact Engineering.* **2015,** *80*, 162-176.

145. Eddoumy, F. Impact of texturing on sliding wear behaviour of UHMWPE. Université de Strasbourg, 2012.

146. Mansfield, M.; Boyd, R. H. Molecular motions, the alpha relaxation, and chain transport in polyethylene crystals. *J. Polym. Sci. Pt. B Polym. Phys.* **1978,** *16*, 1227-1252.

147. Edin, S. Dielectric studies of molecular-relaxation in low density polyethylene: the influence of drawing and ionizing radiation. *Polymer.* **2002,** *43*, 5969-5978.

148. Subramani, K.; Fonseca, M.; Guedes, R.; Oliveira, M.; Simões, J. Thermo-Mechanical Behaviour of Ultrahigh Molecular Weight Polyethylene-Carbon Nanotubes Composites under Different Cooling Techniques. *Deffect and Diffusion Forum.* **2011,** *312-314*.

149. Manzur, A.; Hernández-Sáncehz, F. Activation Energy for the Glass Transition of a Confined Elastomer in HDPE/PP Blends. *Journal of Macromolecular Science Part B Physics.* **2006,** *45*, 139-152.

150. Musib, M. A Review of the History and Role of UHMWPE as A Component in Total Joint Replacements. *International Journal of Biological Engineering.* **2012,** *1*, 6-10.

151. Azam, A. M.; Mehmood, M. S. Thermal stability of Ultra High Molecular Weight Polyethylene Nano Composites with $Mg_{0.15}$ $Ni_{0.15}$ $Zn_{0.70}$ Fe_2O_3. *Journal of Materials Physics and Chemistry.* **2017,** *5*, 39-42.

152. Boldizar, A.; Klason, C.; Kubát, J.; Näslund, P.; Sáha, P. Prehydrolyzed Cellulose as Reinforcing Filler for Thermoplastics. *Int. J. Polym. Mater. Po.* **1987,** *11*, 229-262.

153. Favier, V.; Chanzy, H.; Cavaille, J. Y. Polymer Nanocomposites Reinforced by Cellulose Whiskers. *Macromolecules.* **1995,** *28*, 6365-6367.

154. Boran, S. Mechanical, Morphological, and Thermal Properties of Nutshell and Microcrystalline Cellulose Filled High-Density Polyethylene Composites. *Bioresources.* **2016,** *11*, 1741-1752.

155. Gill, Y. Preparation and characterization of polyethylene based nanocomposites for potential applications in packaging. Loughborough University, Creative Commons Attribution, 2015.

156. Liu, C.; Wei, Y.-F.; Qiu, H.-T.; Zhang, J.; Liu, C.-J. Study on the rheological behaviors of UHMWPE/CA-MMT nanocomposite. *Polym. Compos.* **2015,** *36*, 47-50.

157. Adewunmi, A.; Al-Juhani, A.; Thomas, S.; De, S.; A, A. Effect of modified and nonmodified carbon nanotubes on the rheological behavior of high density polyethylene nanocomposite. *J. Nanomater.* **2013,** *2013*, 12.

158. Cipriano, T.; Silva, A.; Fonseca, A. Rheological and morphological properties of composites based on polylactide and talc. *J. Mater. Sci. Eng. B.* **2013,** *3*, 695-699.

159. Escócio, V. A.; Pacheco, E. B. A. V.; Silva, A. L. N. d.; Cavalcante, A. d. P.; Visconte, L. L. Y. Rheological behavior of renewable polyethylene (HDPE) composites and sponge gourd (luffa cylindrica) residue. *Int. J. Polym. Sci.* **2015,** *2015*.

160. Bikiaris, D. Microstructure and properties of polypropylene/carbon nanotube nanocomposites. *Materials.* **2010,** *3*, 2884-2946.

161. Gunning, M. A.; Istrate, O. M.; Geever, L. M.; Lyons, J. G.; Blackie, P.; Chen, B.; Higginbotham, C. L. The effect of maleic anhydride grafting efficiency on the flexural properties of polyethylene composites. *J. Appl. Polym. Sci.* **2012,** *124*, 4799-4808.

162. Kim, J.; Kwak, S.; Hong, S. M.; Lee, J. R.; Takahara, A.; Seo, Y. Nonisothermal Crystallization Behaviors of Nanocomposites Prepared by In Situ Polymerization of High-Density Polyethylene on Multiwalled Carbon Nanotubes. *Macromolecules.* **2010,** *43*, 10545-10553.

163. Han, J.; Zhu, Y.; Hu, J.; Luo, H.; Yeung, L.-Y.; Li, W.; Meng, Q.; Ye, G.; Zhang, S.; Fan, Y. Morphology, reversible phase crystallization, and thermal sensitive shape memory effect of cellulose whisker/SMPU nano-composites. *J. Appl. Polym. Sci.* **2012,** *123*, 749-762.

164. Özmen, N.; Cetin, N. S.; Mengeloğlu, F.; Birinci, E. Effect of Wood Acetylation with Vinyl Acetate and Acetic Anhydride on the Properties of Wood-Plastic Composites. *Bioresources.* **2012,** *8*, 15.

165. Abu Bakar, M. B.; Ishak, Z.; Mat Taib, R.; Rozman, H.; Saad, M. J. Flammability and Mechanical Properties of Wood Flour-Filled Polypropylene Composites. *Journal of Applied Polymer Science.* **2010,** *116*, 2714-2722.

166. Mengeloglu, F.; Karakus, K. Thermal Degradation, Mechanical Properties and Morphology of Wheat Straw Flour Filled Recycled Thermoplastic Composites. *Sensors (Basel).* **2008,** *8*, 500-519.

167. Ardhyananta, H.; Ismail, H. Effects of Organoclay Loading and Ethylene Glycol on Mechanical, Morphology and Thermal Properties of Ethylene Vinyl Acetate /Organoclay Nanocomposites. *J. Reinf. Plast. Comp.* **2007,** *26*, 789.

168. George, J.; Sabapathi, S. N. Cellulose nanocrystals: synthesis, functional properties, and applications. *Nanotechnol. Sci. Appl.* **2015,** *8*, 45-54.

169. Heidarbeigi, J.; Borghei, A. M.; Afshari, H. The mechanical and thermal properties of PE/CNC nanocomposite. *Int. J. Nano Dimens.* **2019,** *10*, 209-216.

170. Uhl, F. M.; Davuluri, S. P.; Wong, S. C.; Webster, D. C. Organically Modified Montmorillonite in UV Curable Urethane Acrylate Film. *Polymer.* **2004,** *445*, 6175-6187.

171. Gong, G.; Pyo, J.; Mathew, A. P.; Oksman, K. Tensile behavior, morphology and viscoelastic analysis of cellulose nanofiber-reinforced (CNF) polyvinyl acetate (PVAc). *Compos. Pt. A Appl. Sci. Manuf.* **2011,** *42*, 1275-1282.

172. Spoljaric, S.; Genovese, A.; Shanks, R. A. Polypropylene–microcrystalline cellulose composites with enhanced compatibility and properties. *Compos. Pt. A Appl. Sci. Manuf.* **2009,** *40*, 791-799.

173. Qiu, W.; Zhang, F.; Endo, T.; Hirotsu, T. Effect of maleated polypropylene on the performance of polypropylene/cellulose composite. *Polym. Compos.* **2005,** *26*, 448-453.

174. Bagheriasl, D.; Carreau, P.; Dubois, C.; Riedl, B. Effect of cellulose nanocrystals (CNCs) on crystallinity, mechanical and rheological properties of polypropylene/CNCs nanocomposites. *AIP Conference Proceedings.* **2015,** *1664*, 070010.

175. Mirabella, F. M.; Bafna, A. Determination of the crystallinity of polyethylene/α-olefin copolymers by thermal analysis: Relationship of the heat of fusion of 100% polyethylene crystal and the density. *Journal of Polymer Science Part B: Polymer Physics.* **2002,** *40*, 1637-43.

176. Qiao, R.; Catherine Brinson, L. Simulation of interphase percolation and gradients in polymer nanocomposites. *Compos. Sci. Technol.* **2009,** *69*, 491-499.

177. Ramanathan, T.; Abdala, A. A.; Stankovich, S.; Dikin, D. A. Functionalized graphene sheets for polymer nanocomposites. *Nat. Nanotechnol.* **2008,** *3*, 327-331.

178. Salavagione, H. J.; Gomez, M. A.; Martinez, G. Polymeric modification of graphene through esterification of graphite oxide and poly (vinyl alcohol). *Macromolecules.* **2009,** *42*, 6331-6334.

179. Rahimi, S. K.; Otaigbe, J. U. Polyamide 6 nanocomposites incorporating cellulose nanocrystals prepared by In situ ring-opening polymerization: Viscoelasticity, creep behavior, and melt rheological properties. *Polym. Eng. Sci.* **2016,** *56*, 1045-1060.

180. Chopra, D.; Kontopoulou, M.; Vlassopoulos, D.; Hatzikiriakos, S. G. Effect of maleic anhydride content on the rheology and phase behavior of poly (styrene-co-maleic anhydride)/poly (methyl methacrylate) blends. *Rheologica Acta.* **2002,** *41*, 10-24.

181. Han, C. D. Influence of molecular weight distribution on the linear viscoelastic properties of polymer blends. *J. Appl. Polym. Sci.* **1988,** *35*, 167-213.

182. Tian, J.; Yu, W.; Zhou, C. The preparation and rheology characterization of long chain branching polypropylene. *Polymer.* **2006,** *47*, 7962-7969.

183. Corrêa, A. C.; de Morais Teixeira, E.; Carmona, V. B.; Teodoro, K. B. R.; Ribeiro, C.; Mattoso, L. H. C.; Marconcini, J. M. Obtaining nanocomposites of polyamide 6 and cellulose whiskers via extrusion and injection molding. *Cellulose.* **2014,** *21*, 311-322.

184. Ljungberg, N.; Bonini, C.; Bortolussi, F.; Boisson, C.; Heux, L.; Cavaillé, J.-Y. New nanocomposite materials reinforced with cellulose whiskers in atactic polypropylene: effect of surface and dispersion characteristics. *Biomacromolecules.* **2005,** *6*, 2732-2739.

185. Habibi, Y.; Goffin, A.-L.; Schiltz, N.; Duquesne, E.; Dubois, P.; Dufresne, A. Bionanocomposites based on poly (ε-caprolactone)-grafted cellulose nanocrystals by ring-opening polymerization. *J. Mater. Chem.* **2008,** *18*, 5002-5010.

186. Karnani, R.; Krishnan, M.; Narayan, R. Biofiber-reinforced polypropylene composites. *Polym. Eng. Sci.* **1997,** *37*, 476-483.

187. Tjong, S. C.; Xu, Y.; Meng, Y. Z. Composites based on maleated polypropylene and methyl cellulosic fiber: Mechanical and thermal properties. *J. Appl. Polym. Sci.* **1999,** *72*, 1647-1653.

188. Lezak, E.; Kulinski, Z.; Masirek, R.; Piorkowska, E.; Pracella, M.; Gadzinowska, K. Mechanical and Thermal Properties of Green Polylactide Composites with Natural Fillers. *Macromol. Biosci.* **2008,** *8*, 1190-1200.

189. Ashori, A. Hybrid Composites from Waste Materials. *J. Polym. Environ.* **2010,** *18*, 65-70.